INFORMATION TO USERS

This manuscript has been reproduced from the microfilm master. UMI films the text directly from the original or copy submitted. Thus, some thesis and dissertation copies are in typewriter face, while others may be from any type of computer printer.

The quality of this reproduction is dependent upon the quality of the copy submitted. Broken or indistinct print, colored or poor quality illustrations and photographs, print bleedthrough, substandard margins, and improper alignment can adversely affect reproduction.

In the unlikely event that the author did not send UMI a complete manuscript and there are missing pages, these will be noted. Also, if unauthorized copyright material had to be removed, a note will indicate the deletion.

Oversize materials (e.g., maps, drawings, charts) are reproduced by sectioning the original, beginning at the upper left-hand corner and continuing from left to right in equal sections with small overlaps.

Photographs included in the original manuscript have been reproduced xerographically in this copy. Higher quality 6" x 9" black and white photographic prints are available for any photographs or illustrations appearing in this copy for an additional charge. Contact UMI directly to order.

Bell & Howell Information and Learning
300 North Zeeb Road, Ann Arbor, MI 48106-1346 USA

UMI®
800-521-0600

ATOMIC HYDROGEN-ASSISTED EPITAXY FOR THE REDUCTION OF COMPOSITION MODULATION IN InGaAsP

By
Ray Robert LaPierre, B. Sc., M. Eng.

A Thesis
Submitted to the School of Graduate Studies
in Partial Fulfillment of the Requirements
for the Degree
Doctor of Philosophy

McMaster University
Copyright by Ray Robert LaPierre, 1997

ATOMIC HYDROGEN-ASSISTED EPITAXY FOR THE REDUCTION OF COMPOSITION MODULATION IN InGaAsP

DOCTOR OF PHILOSOPHY (1997) | MCMASTER UNIVERSITY
(Engineering Physics) | Hamilton, Ontario

TITLE: Atomic hydrogen-assisted epitaxy for the reduction of composition modulation in InGaAsP

AUTHOR: Ray Robert LaPierre, B. Sc. (Dalhousie University),
M. Eng. (McMaster University)

SUPERVISOR: Dr. D. A. Thompson

NUMBER OF PAGES: xii, 105

Abstract

A miscibility gap exists in the InGaAsP/InP system of heterostructures such that a lateral composition modulation (LCM) occurs on the surface during growth resulting in the production of InAs-rich and GaP-rich regions within the layer. As a consequence, the important material properties relevant to optoelectronic device performance, such as the carrier mobility, luminescent properties and surface morphology, are less than optimum. Hence, this work investigates the influence of LCM on the structural and optical properties of InGaAsP quantum wells and thick layers grown by gas source molecular beam epitaxy on (100) InP substrates.

Two novel growth techniques, argon plasma-assisted epitaxy and atomic hydrogen-assisted epitaxy, are developed to reduce the LCM. The reduction in LCM obtained with plasma-assisted epitaxy is explained in terms of the presence of atomic hydrogen within the argon plasma stream. A detailed atomistic model, including surface reconstruction effects based on reflection high energy electron diffraction observations, is developed to describe the surface-mediated processes that occur during growth in the presence of atomic hydrogen. A simple rate equation model is used to understand the reduced LCM in terms of a decreased surface diffusion length of adatoms.

Acknowledgements

First, I would like to express my gratitude for the supervision of Dave Thompson. Special thanks are also deserved by Brad Robinson and Scott McMaster for their assistance with the MBE growths. In particular, this thesis was greatly assisted by conversations with Brad Robinson. I also wish to thank Ciara Mullan and Tatsuya Okada for their assistance with the TEM. Patterned substrates and SIMS results were provided by *Nortel Technology* in Ottawa. This work was supported by the *Ontario Centre for Materials Research* and by an *Ontario Graduate Scholarship*. I am also grateful to my friends and colleagues Heidi, John, Greg, Peter, Doris, Marcel, Jim, Kelvin, the two Mikes, Lakshmi, Debbie, Steve, Judy and many others who made my stay here enjoyable. This thesis would also have been impossible without the love and support of my family.

Table of Contents

1. Introduction 1

2. Growth and Characterization Techniques 7
2.1. Molecular Beam Epitaxy 7
2.2. Argon Plasma-assisted and Atomic Hydrogen-assisted Epitaxy 12
2.3. Characterization Techniques 13
2.3.1. Photoluminescence 13
2.3.2. Double Crystal X-ray Diffraction 16
2.3.3. Transmission Electron Microscopy 19

3. Lateral Composition Modulation in InGaAsP Strained Layers and Quantum Wells 20
3.1. Transmission Electron Microscopy 21
3.2. X-ray Diffraction 23
3.3. Photoluminescence from Thick Layers 23
3.4. Photoluminescence from Quantum Wells 30
3.5. Discussion 35
3.6. Chapter Conclusions 36

4. Argon Plasma-assisted and Atomic Hydrogen-assisted Epitaxy of InGaAsP Grown at Various Temperatures . . . 37
4.1. Argon Plasma-assisted Epitaxy 37
4.1.1. Transmission Electron Microscopy 38
4.1.2. X-ray Diffraction 40
4.1.3. Photoluminescence from Thick Layers 41
4.1.4. Photoluminescence from Quantum Wells 44
4.2. Atomic Hydrogen-assisted Epitaxy 47
4.2.1. Transmission Electron Microscopy 48
4.2.2. Photoluminescence 50
4.2.3. Homoepitaxial Growths on Patterned Substrates 52
4.2.4. RHEED Observations 53
4.2.5. Diode Laser Studies 56
4.3. Chapter Conclusions 61

5. Atomic Hydrogen-assisted epitaxy of InP 62
5.1. Hall Effect Results 62
5.2. Photoluminescence 70
5.3. Chapter Conclusions 73

6. Growth Mechanisms of III-V Compounds during Conventional and Atomic Hydrogen-assisted Epitaxy . . . 75
6.1. Incorporation Models and Implications for LCM 75
6.1.1. Incorporation Coefficient Model 77
6.1.2. Thermodynamic Model 80
6.2. Surface-mediated Model of Epitaxy 82
6.2.1. Conventional Epitaxy 86
6.2.2. H-assisted Epitaxy 92
6.3. Chapter Conclusions 96

7. Conclusions and Suggestions for Future Work 98

References 100

List of Figures

Fig. 1.1. x-y compositional plane showing isostrain lines (dashed lines), ...2
isobandgap contours (thin solid lines), and a bulk spinodal isotherm curve
(thick solid line) for InGaAsP/InP. The data points labelled (a) to (j) and
A to C (squares) indicate compositions grown in this work.

Fig. 2.1. Schematic of the gas source molecular beam epitaxy system. 9

Fig. 2.2. Schematic of the photoluminescence system. 14

Fig. 2.3. Schematic of (a) the double crystal X-ray diffractometer, and 17
(b) a typical (400) rocking curve.

Fig. 2.4. Illustration of [0 -1 1] cross-sectional TEM foils under two- 19
beam conditions with diffraction vectors of (a) g = 400 and (b) g = 022.
Transmitted beams (T) form bright-field images while diffracted beams
(D) form dark-field images.

Fig. 3.1. Schematic of the sample structure (not drawn to scale) used 20
for the studies in this chapter.

Fig. 3.2. Dark-field, cross-sectional TEM micrographs, using a diffraction 22
vector of g = 022, for the compressively strained samples labelled (a) to
(c), and the tensile strained samples labelled (g) to (j), in Fig. 1.1. The
sample structure is shown in Fig. 3.1. The normal to the TEM foil
surface is in the [0 -1 1] direction.

Fig. 3.3. PL linewidths (FWHM) at 11 and 300 K versus nominal com- 24
position for band-to-band transitions. These data points correspond to
those in Fig. 1.1. The solid lines indicate theoretical linewidths for lattice-
matched material, and the dashed lines are meant as guides to the eye.

Fig. 3.4. Integrated PL intensities at 11 and 300 K versus nominal com- 25
position for band-to-band transitions. These data points correspond to
those in Fig. 1.1. The dashed lines are meant as guides to the eye.

Fig. 3.5. Band-to-band PL spectra at various temperatures from samples (a) to (i) in Fig. 1.1 (continued from previous page). Peaks 1 to 3 are from InAs-rich regions, regions of nominal composition and GaP-rich regions, respectively, as discussed in the text. 25

Fig. 3.6. Structural and corresponding bandgap model for the LCM. 27

Fig. 3.7. Difference between low temperature (11 K) and room temperature (300 K) PL peak energies (left-hand scale), and the corresponding compositional deviations (right-hand scale), versus nominal composition for the PL spectra in Fig. 3.5. A solid line indicates the bandgap difference of 67 meV expected from the Varshni equation, the dashed lines are guides to the eye, and the representative error bar refers to the uncertainty in the compositional deviation. 30

Fig. 3.8. PL linewidth (FWHM) versus nominal composition for the e1-hh1 QW transition at low temperature (11 K). These data points correspond to those in Fig. 1.1. The solid line indicates the theoretical linewidth for fluctuations in well thickness of one monolayer, and the dashed lines are guides to the eye. 31

Fig. 3.9. Temperature-dependence of the PL peak energy for the e1-hh1 transition in the 50 Å QW of samples (b), (e) and (h) in Fig. 1.1. The dashed lines indicate the expected variation from the Varshni equation. 32

Fig. 3.10. Temperature-dependence of the PL linewidth (FWHM) for the e1-hh1 transitions in lattice-matched $In_{0.72}Ga_{0.28}As_{0.61}P_{0.39}$ layers with thicknesses of 50, 100 and 500 Å. The solid lines indicate the contributions of alloy disorder (σ_{alloy}), thermal broadening (σ_{kT}) and interface roughness of 2 monolayers ($\sigma_{(\pm 2\ ML)}$) to the total theoretical linewidth (σ_{total}). 34

Fig. 4.1. Dark-field, cross-sectional TEM micrographs, using diffraction vectors of (a) **g** = 022 and (b) **g** = 400, for an $In_{0.59}Ga_{0.41}As_{0.69}P_{0.31}$ quaternary (Q) comparative structure. The normal to the TEM foil surface is in the [0 -1 1] direction. 39

Fig. 4.2. Room temperature (400) DCXRD spectra from 1000 Å thick $In_{0.59}Ga_{0.41}As_{0.69}P_{0.31}$ layers (sample A) grown with and without Ar plasma at 480 °C. 41

Fig. 4.3. Low temperature (11 K) band-to-band PL spectra from the 1000 Å thick $In_{0.59}Ga_{0.41}As_{0.69}P_{0.31}$ layers (sample A) grown with and without Ar plasma at various temperatures. The relative PL intensity for the spectrum at 480 °C is multiplied by 10 for the case with plasma and 1000 for the case without plasma. The other spectra are on the same scale. 42

Fig. 4.4. Room temperature (300 K) and low temperature (11 K) band-to-band PL linewidths (FWHM) versus growth temperature from the 1000 Å thick $In_{0.59}Ga_{0.41}As_{0.69}P_{0.31}$ layers (sample A) grown with and without Ar plasma. The dashed lines are guides to the eye. 43

Fig. 4.5. Room temperature (300 K) and low temperature (11 K) integrated PL intensity versus growth temperature from the 1000 Å thick $In_{0.59}Ga_{0.41}As_{0.69}P_{0.31}$ layers (sample A) grown with and without Ar plasma. The dashed lines are guides to the eye. 44

Fig. 4.6. Temperature-dependence of the PL peak energy shifts, measured with respect to the room temperature PL peak energies, from the 50 Å $In_{0.59}Ga_{0.41}As_{0.69}P_{0.31}$ QWs (sample A) grown with and without Ar plasma at various growth temperatures (400-480 °C). The thick line shows the expected variation from the Varshni equation. 45

Fig. 4.7. Room temperature PL linewidths (FWHM) from 50 Å $In_{0.59}Ga_{0.41}As_{0.69}P_{0.31}$ QWs (0.64% tension, sample A) and $In_{0.31}Ga_{0.69}As$ QWs (1.5% tension, sample B) grown with (filled symbols) and without (open symbols) Ar plasma. Results from 72 Å lattice-matched $In_{0.53}Ga_{0.47}As$ QWs grown without plasma, as discussed in the text, are included for reference (diamonds). The dashed lines are guides to the eye. 46

Fig. 4.8. Bright-field, cross-sectional TEM micrographs, using diffraction vectors of g = 022 and 0 -2 2, respectively, for a lattice-matched $In_{0.72}Ga_{0.28}As_{0.61}P_{0.39}$ layer (sample C) grown by (a, c) conventional 49

epitaxy without H and (b, d) with a H flux of 0.15 ML/s. The normal to the TEM foil surface is in the [0 -1 1] or [011] direction as indicated.

Fig. 4.9. Room temperature PL linewidths (FWHM) and the red-shifts 50
of the low temperature PL peak energies, as a function of the H flux, for lattice-matched $In_{0.72}Ga_{0.28}As_{0.61}P_{0.39}$ layers (sample C).

Fig. 4.10. Axial TEM micrographs of homoepitaxial growths on patterned 52
InP substrates grown by (a) conventional epitaxy and (b) with a H flux of 0.1 ML/s. The normal to the TEM foil surface is in the [0 -1 1] direction.

Fig. 4.11. Surface reconstructions and corresponding RHEED streak 54
patterns obtained from (a) a conventional surface, and (b) a H-terminated surface.

Fig. 4.12. Threshold current density versus stripe width for DH lasers 58
with active regions having bandgap wavelengths of 1.15, 1.3 and 1.55 μm grown by conventional epitaxy at 480 °C.

Fig. 4.13. Slope efficiency versus stripe width for DH lasers with active 59
regions having bandgap wavelengths of 1.15, 1.3 and 1.55 μm grown by conventional epitaxy at 480 °C.

Fig. 4.14. Threshold current density versus stripe width for DH lasers 59
with an active region having bandgap wavelength of 1.3 μm grown by conventional epitaxy at 450 and 480 °C.

Fig. 4.15. Slope efficiency versus stripe width for DH lasers with an 60
active region having a bandgap wavelength of 1.3 μm grown by conventional epitaxy at 450 and 480 °C.

Fig. 4.16. Threshold current density versus stripe width for DH lasers 60
with an active region having a bandgap wavelength of 1.3 μm grown at 480 °C by conventional epitaxy and H-assisted epitaxy.

Fig. 4.17. Slope efficiency versus stripe width for DH lasers with an 61
active region having bandgap wavelength of 1.3 μm grown at 480 °C by

conventional epitaxy and H-assisted epitaxy.

Fig. 5.1. Room temperature Hall effect results for as-grown (open symbols) and annealed (closed symbols) InP homoepitaxial layers grown by conventional epitaxy (circles), and H-assisted epitaxy using $T_H = 1600$ °C (crossed square) and 1900 °C (diamonds). Hall effect results are also shown for a lattice-matched $In_{0.72}Ga_{0.28}As_{0.61}P_{0.39}$/InP layer grown by H-assisted epitaxy (open squares), and an InP homoepitaxial layer grown by Ar plasma-assisted epitaxy (triangle). The dashed lines indicate theoretical compensation ratios, $\phi = N_a/N_d$. 63

Fig. 5.2. Net donor, N_d, and acceptor concentrations, N_a, for the data in Fig. 6.1. The PH_3 cracker temperature was $T_c = 975$ °C unless indicated otherwise. The arrows for $T_c = 875$, 1050 and 1125 °C refer to single data points. The dashed lines indicate theoretical compensation ratios, $\phi = N_a/N_d$. 65

Fig. 5.3. SIMS yield as a function of depth from the surface for (a) an InP structure grown with deuterium, as discussed in the text, and (b) the same sample after annealing at 700 °C for 1 minute. 69

Fig. 5.4. Low temperature (15 K) PL spectra from an InP homoepitaxial layer grown by conventional epitaxy (thin solid line), and H-assisted epitaxy using $T_H = 1600$ °C (thick solid line) and 1900 °C (dashed line). The peaks labelled 1 to 6 are discussed in the text. 71

Fig. 5.5. Band-edge exciton PL (peak 1 in Fig. 6.4) and additional spectra obtained with various PH3 cracker cell temperatures, T_c, and H cracker cell temperatures, T_H. Results are shown for conventional growths (thin solid lines), and H-assisted growths using $T_H = 1600$ °C (thick solid line) and 1900 °C (dashed line). 72

Fig. 6.1. Incorporation data showing As solid content, y, versus arsine flow fraction, Y. The V/III beam flux ratio is k and the growth rate is 1 μm/hr unless stated otherwise. The dashed lines are fits from the thermodynamic model as described in the text. 77

Fig. 6.2. Incorporation coefficient data fitted with the thermodynamic model . . . 79
(dashed curves). The arrows indicate the regions of immiscibility as discussed in the text.

Fig. 6.3. Surface models for electronically stable intermediate structures 85
for a (100) III-V surface grown by ((a) to (c)) conventional epitaxy, and ((d), (e)) H-assisted epitaxy.

Fig. 6.4. Surface diffusion length ratio, λ'/λ, versus the H surface 95
coverage, θ, using a model parameter of m/m' = 1, 1.5 and 3. Experimental data points are derived from the linewidth (FWHM) and red-shift (ΔE) measurements in Fig. 4.9, and the growth rate (GR) measurements at the bottom of etched grooves as in Fig. 4.10.

CHAPTER 1

Introduction

The room temperature direct bandgap wavelength in the $In_{1-x}Ga_xAs_yP_{1-y}$/InP system of heterostructures can be varied by changing the composition (x and y) of the solid solution making them useful for various optoelectronic devices. However, epitaxial growth of these alloys is problematic due to the existence of a miscibility gap [1.1, 1.2]. The miscibility gap is a range of compositions and temperatures in which the InGaAsP solid solution is energetically unstable so that a lateral composition modulation (LCM) develops during growth, producing InAs-rich and GaP-rich regions within the layer. In the case of $In_{1-x}Ga_xAs$ (y = 1), the alloy separates into InAs-rich and GaAs-rich regions.

The InGaAsP compositions which undergo LCM can be roughly predicted thermodynamically for any growth temperature by the bulk, strain-free spinodal isotherm shown in Fig. 1.1 [1.3, 1.4]. This spinodal curve is the locus of the points of inflection (x and y) in the total Gibbs free energy of the alloy which defines the limits of the miscibility gap at a given temperature. The spinodal isotherm in Fig. 1.1 is shown at a temperature of 480 °C, as typically used during growth of these layers by gas source molecular beam epitaxy (GSMBE) [1.5]. The arrows near sample (e) in Fig. 1.1 indicate that the InGaAsP compositions within the spinodal isotherm separate into GaP-rich and InAs-rich regions, as determined theoretically [1.1, 1.2] and experimentally [1.6]. Also shown in Fig. 1.1 are various isostrain lines (dashed lines) and isobandgap contours (thin solid lines) for InGaAsP layers grown on (100) InP substrates [1.7]. Finally, the data points labelled (a) to (j) and A to C indicate the compositions studied in this work.

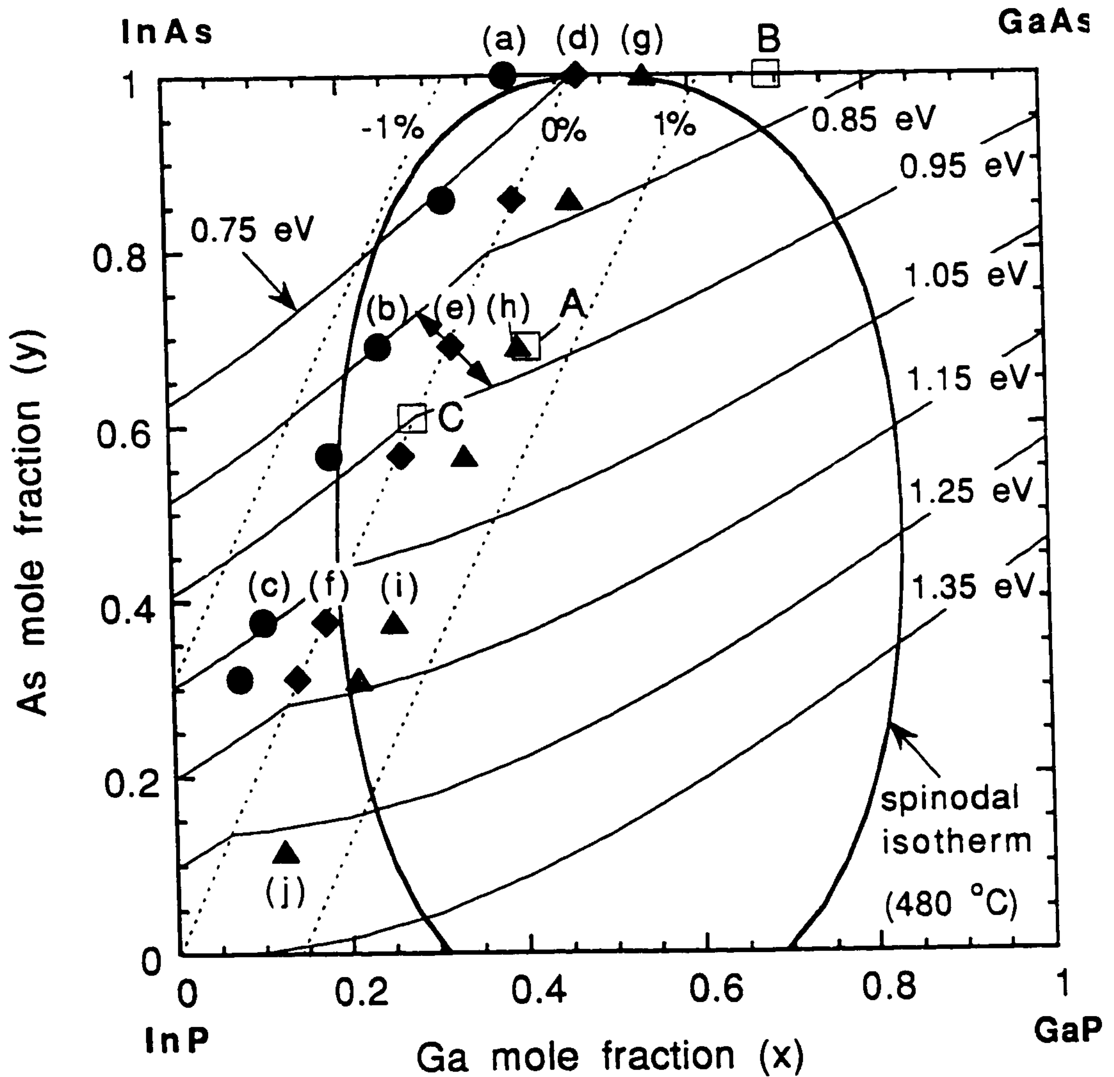

Fig. 1.1. x-y compositional plane showing isostrain lines (dashed lines), isobandgap contours (thin solid lines), and a bulk spinodal isotherm curve (thick solid line) for InGaAsP/InP. The data points labelled (a) to (j) and A to C (squares) indicate compositions grown in this work.

The phase separation of an alloy arises as a result of the positive enthalpy of mixing of the constituent elements. Historically, the enthalpy term of the Gibbs free energy for

ternary or quaternary materials has been calculated using two techniques. First, the enthalpy can be expressed in terms of interaction parameters that are adjusted to match calorimetric data [1.8]. Second, the enthalpy can be determined by the delta lattice parameter model of Stringfellow in terms of the difference in lattice constants among the binary constituents of the alloy [1.9]. This model suggests that the positive enthalpy of mixing is associated with the bending and stretching of the binary bonds from their equilibrium values. Most recently, this model has been supported theoretically by detailed thermodynamic models, such as the cluster variation method, and experimentally by extended X-ray absorption fine structure (EXAFS) studies [1.10, 1.11].

A random arrangement of atoms is initially deposited on the surface during epitaxial growth such that an ideal InGaAsP alloy would have the group III atoms (In and Ga) and group V atoms (As and P) distributed randomly on their respective sublattices of the zincblende structure. In such a random arrangement, the In-As bonds become compressed and the Ga-P bonds become elongated for incorporation in a homogeneous quaternary. Hence, thermodynamic models show that a driving force for phase separation exists due to the positive enthalpy of mixing associated with the bending and stretching of the binary bonds from their equilibrium values [1.10, 1.11]. This means that the microscopic strain energy of any alloy within the miscibility gap can be reduced during growth by separating into two distinct phases with compositions near the end point binary compounds. Since In-As is the longest and Ga-P is the shortest of the four binary constituent bonds, they tend to be strained more than the other two bonds, which have intermediate lengths. Since the energy is minimized by reducing the number of bonds with the greatest strain, the production of InAs-rich and GaP-rich regions is favored.

The occurrence of LCM has been observed experimentally in ternary and quaternary semiconductor alloys such as InGaAs, InGaP and InGaAsP lattice-matched to InP or GaAs substrates [1.3-1.21]. This thesis addresses four major deficiencies in these earlier studies and extends other studies performed by the author [1.22, 1.23]. First, the compositional fluctuations that occur as a result of phase separation have been observed primarily as a

black-white contrast in plan-view or cross-sectional transmission electron micrographs of the alloy. Other techniques capable of probing the amplitude of the compositional fluctuations, such as X-ray diffraction or photoluminescence, have not been used extensively. This thesis uses both photoluminescence and X-ray diffraction, in addition to transmission electron microscopy, to investigate the LCM in InGaAsP layers deposited by GSMBE on (100) InP substrates. In this way, both the amplitude and period of the compositional fluctuations are studied as a function of the nominal InGaAsP composition and growth conditions.

Second, the influence of the compositional fluctuations on the structural and optical properties of InGaAsP quantum wells (QWs) has received little attention. In addition, the influence of strain on the LCM has not been studied extensively despite the fact that the LCM, particularly of tensile strained layers which lie deep within the miscibility gap, may impose limitations in various optoelectronic devices such as strain compensated laser structures [1.24]. The LCM of InGaAsP strained layers and QWs grown by GSMBE on (100) InP substrates is therefore investigated in chapter 3.

Third, no work has been done concerning the effect of LCM on the performance of optoelectronic devices. Fig. 1.1 shows that at a typical growth temperature of 480 °C for GSMBE the lattice-matched InGaAsP/InP alloy lies inside the unstable region for As mole fractions in the solid greater than about 0.4. Hence, the InGaAsP compositions required for heterostructure devices designed to operate at the wavelengths of interest for optical communications (1.3 and 1.55 μm) would typically lie within the miscibility gap. As a consequence, the important material properties relevant to optoelectronic device performance, such as the carrier mobility, luminescent properties and surface morphology, are less than optimum. The work in this thesis therefore establishes, for the first time, the detrimental effects of LCM on diode laser performance.

Fourth, the influence of the surface on the phase separation process is not generally appreciated. Previous thermodynamic models for describing LCM [1.18-1.21] implicitly

assume that the crystal grows by the simultaneous formation of all the tetrahedral bonds in the bulk and are therefore inadequate for describing the actual surface-mediated processes that occur during epitaxy. Bulk thermodynamic models predict that the phase separation process will occur only at temperatures below a specific critical temperature, T_C, since the entropy term dominates the Gibbs free energy at higher temperatures favoring the formation of a disordered (homogeneous) alloy. Hence, from thermodynamic considerations spinodal decomposition is expected not to occur for a sufficiently high growth temperature. The relatively high growth temperatures (≈ 650 °C) used by some growth techniques, such as LPE and MOCVD, may therefore suppress the LCM. For GSMBE growth, on the other hand, kinetic limitations whereby the adatom surface diffusion lengths are reduced via decreased growth temperatures or increased group V overpressures, appear to limit the ability of the system to achieve thermodynamic equilibrium resulting in less LCM [1.23, 1.24]. Hence, the LCM can be minimized if the adatoms are covered over by successive layers before they can diffuse significant distances on the surface. Once the atoms are frozen in the solid, they migrate very little due to the extremely low diffusion constants in the bulk material.

The surface control of the LCM will be demonstrated by two novel growth techniques, Ar plasma-assisted epitaxy and atomic hydrogen-assisted epitaxy. The role of atomic hydrogen in epitaxial growth, produced either by plasma or by thermal cracking, has been investigated by many authors. Some applications include low temperature oxide desorption, gettering of surface impurities during growth, defect or impurity passivation, and altered growth processes [1.25]. Growth in the presence of H has also been shown to produce less three-dimensional (3D) island growth and fewer dislocations in strained layer epitaxy [1.26-1.31], and to enhance the step flow growth on vicinal substrates [1.32-1.35]. Hence, the phase separation process may be significantly influenced by the effects of atomic hydrogen on the surface. The details of these growth techniques are discussed in chapter 2 with results presented in chapter 4. The electrical and optical properties of InP homoepitaxial layers grown by plasma-assisted and atomic hydrogen-assisted epitaxy are

also investigated in chapter 5. Finally, a detailed atomistic model, including surface reconstruction effects based on reflection high energy electron diffraction observations, is developed in chapter 6 to explain the reduction in LCM obtained with H exposure. A simple rate equation model is used to understand the reduced LCM in terms of a decreased surface diffusion length of adatoms in the presence of atomic hydrogen. This represents the first detailed surface model of the LCM to include surface reconstruction effects.

CHAPTER 2

Growth and Characterization Techniques

This chapter provides an overview of the epitaxial growth and characterization techniques used throughout this thesis.

2.1. Molecular Beam Epitaxy

Epitaxy is defined as the deposition of a layer with the same crystal structure as the substrate on which it is grown. Molecular beam epitaxy (MBE) is a method for growing epitaxial layers under ultra-high vacuum conditions by directing atomic and molecular beams onto a heated single-crystal surface, where they react. The stream of atoms or molecules effuse from their sources under ultra-high vacuum (UHV) conditions such that collisions with each other, or with residual gases, do not occur during transit to the substrate. In other words, the mean free path of the beam constituents is longer than the source-to-substrate distance. MBE offers precise control over the incident atomic and molecular fluxes so that "sticking" probability differences between the growth species may be taken into account, and the beams may be switched on and off rapidly to produce monolayer control for the realization of sharp interfaces and abrupt doping profiles.

In gas source molecular beam epitaxy (GSMBE) [1.5], as used for the growths in this thesis, evaporation sources are used for the group III elements (In and Ga) as well as for the two dopant elements (Be for p-type doping and Si for n-type doping). The solid source cells are chemically inert, cylindrical or conical containers made of pyrolytic boron nitride that hold the elements to be evaporated. When the effusion ovens are resistance-heated, the vapour pressure of the elements they contain increases. Under the UHV conditions existing in the MBE system, atomic beams are emitted (effused) from the cell

aperture providing a typical growth rate of 1 μm/hr (≈ 1 monolayer/s). Each cell has an externally controlled mechanical shutter in front of it for starting and stopping the beam. Precise temperature control of the effusion cells, provided by thermocouple feedback, is required for precise compositional control of the layers. To obtain uniform growth over a large substrate area, the sample stage is rotated (≈ 30 rpm) so that the surface receives the time-averaged flux.

Control problems associated with solid P and/or As sources are overcome in GSMBE by using beams containing As_2, P_2, and H_2 generated by the thermal decomposition of the hydrides, arsine (AsH_3) and phosphine (PH_3) [1.5]. The hydrides are decomposed in a single, low pressure cracker with a heated rhenium wire catalyst. The AsH_3 and PH_3 vapour is delivered into the cracker cell by a gas-handling system that uses a baratron-based pressure control system with the resulting gas flow rates indicated by calibrated flow meters. The valve combinations of the gas handling system simulate the shutter operation of the group III sources. The hydride sources are mixed in the gas cracking cell and effuse into the MBE system through the same tube. The resulting arsenic and phosphorus species are a mixture of monomers, dimers, and tetramers (for example, P, P_2, and P_4, respectively). The relative amounts of these will depend upon the temperature and pressure, and the degree to which thermodynamic equilibrium is achieved in the cracker cell. Since the tetramers have a very low incorporation probability, the cracker is typically operated at 1000 °C to insure a dominant dimer concentration. The P_4/P_2 beam flux ratio is about 10^{-4} under these conditions [2.1].

Fig. 2.1 shows the UHV system presently used for our MBE studies. The main growth chamber is a stainless-steel, oil-diffusion pumped chamber with a liquid nitrogen cold trap giving an ultimate base pressure of about 10^{-10} Torr after baking. The group III beam sources and dopants are thermally isolated from each other by a liquid nitrogen (LN_2) cooled radial vane baffle, which prevents chemical cross-contamination and thermal cross-

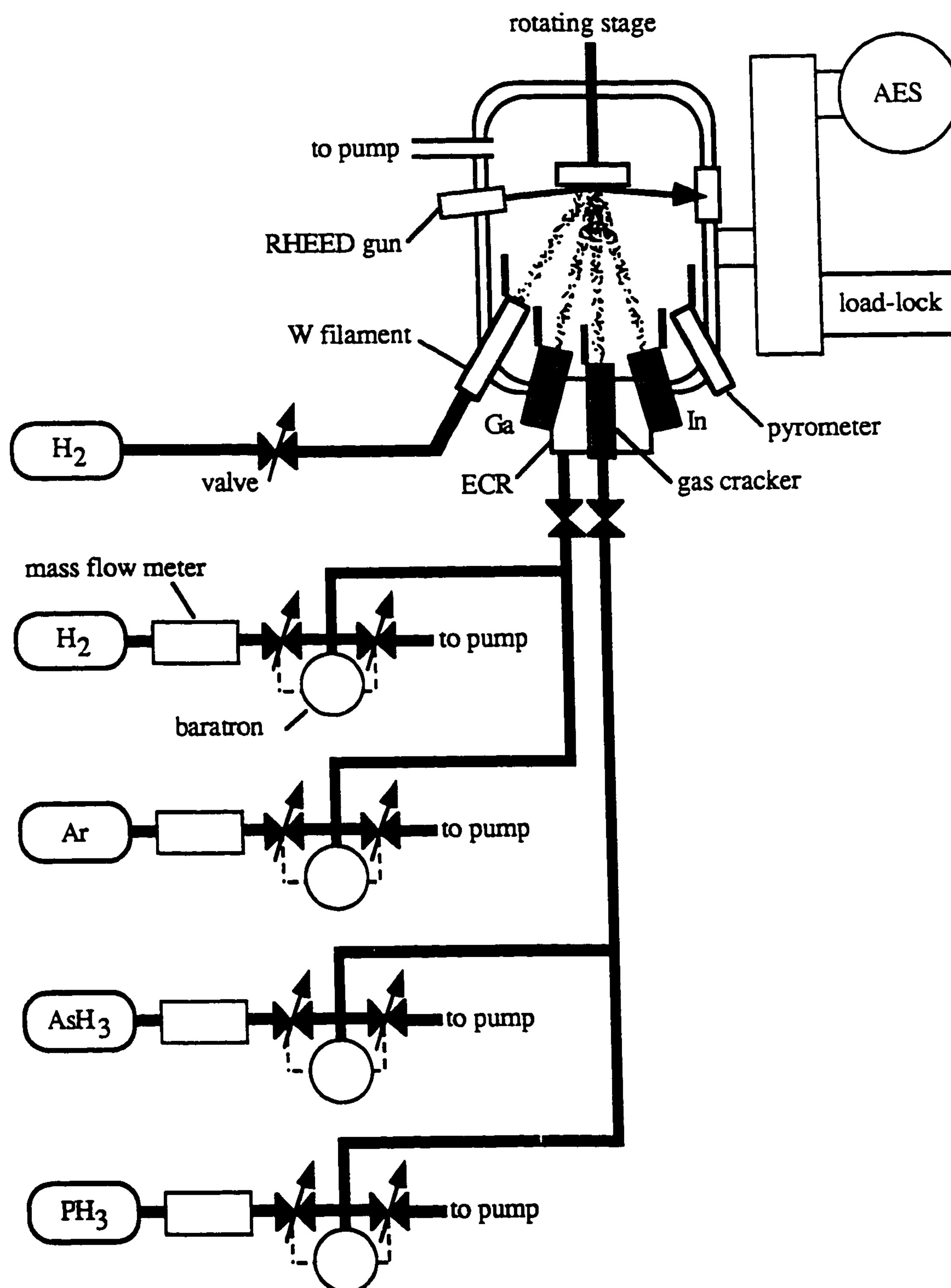

Fig. 2.1. Schematic of the gas source molecular beam epitaxy system.

talk. Cryogenically (LN_2) cooled walls are also used to reduce unwanted impurities and outgassing. A large H_2 background pressure of about 4×10^{-5} Torr exists during growth due to cracking of the group V hydrides. However, the UHV condition is always maintained with respect to unwanted impurity species. An *in situ* reflection high energy electron diffraction (RHEED) system with an incident electron energy of 28 keV is used to monitor, on a fluorescent screen, the structure of the outermost layers of the sample surface before and during epitaxial growth. The chamber is also equipped with a pyrometer, an *in situ* electron cyclotron resonance (ECR) plasma source, and a vacuum-linked Auger electron spectroscopy (AES) chamber.

To provide the basis for high quality films, a substrate free of defects and clean on an atomic scale must be prepared. The (100) substrates used in our studies were either square pieces, 15x15 mm in size, or quarter pieces cleaved from (100)-oriented (± 0.1°) two inch diameter InP wafers, 400 μm thick. The n-type samples were sulfur-doped with carrier concentrations ranging from $4\text{-}7 \times 10^{18}$ cm^{-3}, and the semi-insulating samples were iron-doped with resistivity greater than 10^7 Ωcm. All substrates were "Epiready" wafers so that no further processing was necessary before loading them into the growth chamber. The samples were, however, exposed to a 5 minute *ex vacuo* ultraviolet/ozone cleaning to remove carbon contamination and to provide a protective oxide passivation layer. The substrate was then mounted in dust-free conditions under a HEPA (high efficiency particulate air) filter. The mounting technique involved clipping the sample to a molybdenum sample holder.

Once mounted, the sample holder was placed in a glass petri dish and enclosed in two polyethylene bags to allow dust-free transfer of the sample to the load-lock of the MBE system. A load-lock enables the sample to be introduced into the MBE system without breaking the vacuum of the growth chamber. After a sufficient pump-down of the load-lock chamber, the sample was transported *in vacuo* to the AES chamber where it was

degassed for 30 minutes at 350 °C for n-type substrates or at 400 °C for semi-insulating substrates. The oxide layer prevents decomposition of the substrate during degassing. After degassing, the samples were transported *in vacuo* to the main MBE growth chamber where the temperature was ramped to 460 °C to prepare for oxide desorption. For substrate temperatures above about 365 °C the evaporation of the InP is no longer congruent, so that P is preferentially evaporated with liquid In remaining. Heating of the sample above 350 °C was therefore done with a P_2 beam impinging on the sample surface, thus reducing the risk of decomposition of the substrate surface.

The temperature of the sample is measured with a thermocouple rigidly fixed to the sample stage about 2 mm below the substrate. Although the thermocouple does not allow an absolute measurement of the substrate surface temperature, it is possible to obtain and maintain a given temperature of the substrate surface accurately. For absolute surface temperature measurement an infrared pyrometer is used. It is calibrated using the well-established temperature of 450 °C above which the surface reconstruction, as determined by RHEED, changes from 2x1 to 2x4.

An *in situ* ECR hydrogen plasma, described elsewhere [2.2], was used to desorb the oxide from the substrate prior to growth. Plasma treatments were done at a substrate temperature of 460 °C and with 8.3 sccm of phosphine flowing through the hydride cracker cell producing an overpressure of P_2. The hydrogen plasma was generated by a hydrogen input of about 2 sccm into the ECR source operating at 300 W forward microwave power and about 100 W reflected power. A timed (shuttered) exposure of 2 minutes of H was generally used. The RHEED technique was used to monitor the cleaning of the substrate surface and the initial stages of epitaxial growth. For an oxidized InP surface the electron beam produces an amorphous glow on the fluorescent screen, while complete removal of the oxide layer produces the 2x4 streak pattern of a clean phosphorus-stabilized (100) InP surface.

After oxide desorption the substrate temperature was ramped to the growth temperature (typically, 450-480 °C). Each run was then initiated by allowing the required

pressure of AsH_3 and/or PH_3 to be established in the cracking cell with no In or Ga flux impinging onto the substrate surface. With the desired As_2 and/or P_2 flux established, the In and/or Ga shutters were opened simultaneously to initiate growth of the epilayer of desired composition. Prior calibration runs had been done to establish the required relative fluxes of all the components. At the conclusion of the growth, the sample was cooled down from the growth temperature under a P_2 flux that was turned off when the substrate temperature dropped below 350 °C.

2.2. Argon Plasma-assisted and Atomic Hydrogen-assisted Epitaxy

Chapter 4 investigates a new Ar plasma-assisted growth technique in which epitaxial layers of InGaAsP are grown by gas source molecular beam epitaxy while simultaneously exposed to an Ar plasma stream produced by electron cyclotron resonance (ECR) as described elsewhere [2.2]. The microwave source operates at 2.45 GHz with a corresponding magnetic field intensity of 875 Gauss for resonance. The Ar plasma stream was generated using an argon input of about 1 sccm into the ECR source operating at 300 W forward microwave power and about 250 W reflected power. A dc substrate bias of +40 V was used during the plasma-assisted growths to reduce the energy of the incident ion component of the plasma [2.3].

Chapter 4 also investigates the role of atomic hydrogen within the Ar plasma stream by using a separate atomic hydrogen source (AHS) supplied by "EPI" [1.25], consisting of a tungsten filament operating at 1600 to 1900 °C. H_2 was delivered to this AHS via an independent manifold consisting of a gas regulator, a leak valve and simple on/off switching with a shutter. The nominal MBE chamber pressure during these atomic hydrogen-assisted growths was varied from 4×10^{-5} Torr, corresponding to the ambient H_2 pressure from cracking the group V hydrides, to 2×10^{-4} Torr, corresponding to about 25 sccm of H_2 supplied to the AHS gas manifold. Assuming 4% cracking efficiency [1.25],

H fluxes of 0.025 to 0.7 monolayer per second (ML/s) were estimated from these pressures. Growths without the AHS were estimated to have a H flux of at most 10^{-2} ML/s from the hydride cracker [2.1].

2.3. Characterization Techniques

This section describes the experimental techniques used throughout this thesis to examine the epilayers after growth: photoluminescence (PL), double crystal X-ray diffraction (DCXRD), and transmission electron microscopy (TEM).

2.3.1. Photoluminescence

Photoluminescence (PL) is a sensitive, non-destructive technique for investigating spontaneous emission processes in semiconductors. When a semiconductor is optically excited, electron-hole pairs are produced (via absorption) in excess of the thermal equilibrium concentration. These excess carriers subsequently relax to the lowest available energy states near the conduction and valence band edges before recombining. If the recombination of the photoexcited electrons and holes results in the emission of light, the process is called photoluminescence.

Fig. 2.2 shows the photoluminescence system used in these studies. Continuous excitation was provided by a 20 mW cw Ar ion laser. A filter, F_1, was used to eliminate the 514.5 nm line from the Ar ion laser, leaving only the 488 nm wavelength. The laser light was modulated with a mechanical chopper to increase the sensitivity of the apparatus by a lock-in technique. The laser beam was focused onto the surface of the sample by the lenses, L_1 and L_2. Low temperature spectra at 11 to 15 K were obtained by using a closed-cycle, helium-refrigerated, diffusion-pumped cryostat. A resistive heater provided variable temperature capability with the temperature measured by a calibrated thermocouple mounted on the cold-head below the sample.

The sample luminescence was dispersed by an f/7.5 0.65 m single-grating

monochromator. The front surface PL from the sample was focused on the entrance slit of the monochromator by the lenses, L_3 and L_4. A filter, F_2, prevents the exciting laser light from entering the monochromator. A 1200 lines/mm grating was used for wavelengths from 0.4 to 1.1 μm and a 600 lines/mm grating was used for wavelengths from 0.8 to 1.8 μm with a typical step size of 1 nm. The monochromator was calibrated against the laser line (488 nm) for wavelength accuracy. The entrance and exit slit widths were kept equal at 500 μm giving a resolution of about 1 nm (≈2 meV at 875 nm).

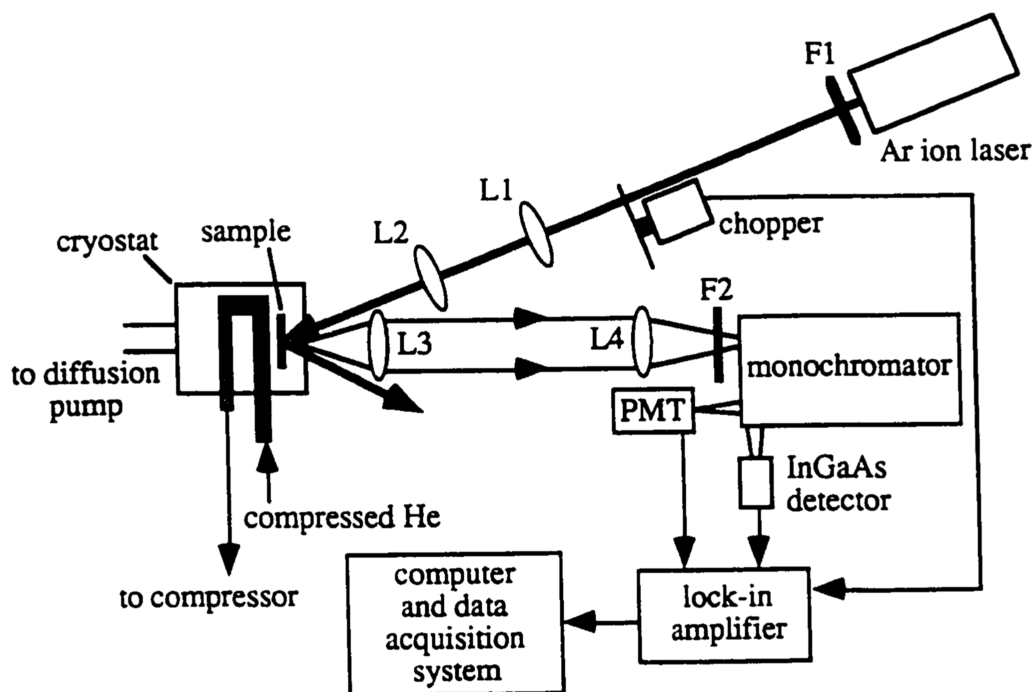

Fig. 2.2. Schematic of the photoluminescence system.

The detector was a water-cooled photomultiplier tube (PMT) for wavelengths from 0.8 to 1.1 μm, while an InGaAs pin photodiode was used for wavelengths from 1.1 to 1.65 μm. The spectral response of the system was determined by measuring the white light spectrum from a calibrated halogen lamp. This correction is important only at higher temperatures when the peaks are broader. At low temperatures (below 77 K), when the

change in system response is negligible over the wavelength range of the measured spectrum, the correction can be ignored.

When a photon generates an electron-hole pair, Coulombic attraction can lead to the formation of an exciton in which the electron and hole remain bound to each other in a hydrogen-like state. In high purity materials at low temperatures, the excess electrons and holes predominantly form excitons which can decay to give free exciton luminescence. Bound exciton recombination, involving donors or acceptors, may also contribute to the band-edge PL in less pure material (donor or acceptor concentrations > 10^{15} cm^{-3}). Finally, band-to-acceptor (e-A), band-to-donor (e-D) and donor-to-acceptor (D-A) recombination may also occur. These impurity-related emission processes are discussed in chapter 5 in order to assess possible contamination problems during atomic hydrogen-assisted epitaxy.

The thermal distribution of electrons in the conduction band and of holes in the valence band contributes a linewidth of 1.8 kT to all band-to-band recombination processes [2.4, 2.5]. Most spectroscopic measurements are therefore performed at low temperatures to prevent thermal ionization of the optically active centres, to minimize thermally-activated non-radiative recombination processes, and to minimize the thermal broadening of sharp spectral features. An additional alloy broadening mechanism exists in the ternary and quaternary samples due to statistical fluctuations of the composition associated with the random positioning of the group III and V elements in each sublattice of the zincblende structure [2.4, 2.5]. This leads to a fluctuation in the bandgap, and thus to a broadening of all electron-hole recombination processes. Also, a contribution to the total linewidth exists in quantum wells due to interface roughness [2.4]. In chapter 3 additional PL linewidth broadening is observed in the band-to-band transitions of InGaAsP layers because the composition of the alloy due to LCM is inhomogeneous over dimensions less than the incident laser beam spot size.

The temperature dependence of the peak position for band-to-band emission in homogeneous material is given empirically by the Varshni equation [2.6]:

$$E_g(T) = E_g(T{=}0) - \frac{\alpha T^2}{T + \beta} \tag{2.1}$$

where $E_g(T = 0\ K) = 1.4236$ eV, $\alpha = 3.63 \times 10^{-4}\ K^{-1}$, and $\beta = 162$ K for InP [2.7]. The same values of α and β may be used for InGaAsP alloys lattice-matched to InP [2.8]. Chapter 3 shows that as the degree of LCM increases, a red-shift in the low temperature PL peak energy is observed relative to that predicted by extrapolating the higher temperature data using Eq. (2.1). This red-shift is shown to result from recombination occurring in the InAs-rich regions associated with the LCM structure and hence can be used as a measure of the compositional fluctuations.

2.3.2. Double Crystal X-ray Diffraction

Lattice mismatch for (100)-oriented samples was determined by measuring the symmetric reflection of the (400) X-ray diffraction peak at room temperature, using the *Bede Scientific Instruments QC1* double crystal diffractometer. Double crystal X-ray diffractometers work by using a reference crystal to produce a highly collimated X-ray beam. To do this, a beam of X-rays is diffracted from the reference crystal and subsequently by the specimen crystal as shown in Fig. 2.3(a). A strong, doubly-diffracted beam is only observed when the crystals are set nearly parallel to one another.

A typical sample structure consists of an epitaxial layer where the presence of strain leads to a tetragonal distortion of the unit cell. If the sample is "illuminated" with a parallel, monochromatic beam of X-rays, and then slowly rotated through the (400) Bragg angle, the substrate will diffract at one angle and the layer at another. The diffracted intensity is measured by counting the number of X-ray photons diffracted from the sample using a scintillator-photomultiplier detector assembly. When the diffracted intensity is measured as a function of angle, a diffraction pattern called a rocking curve results, as shown in Fig. 2.3(b).

The X-ray rocking curve is analyzed by using the Bragg law:

$$\lambda = 2a_{\perp}\sin\theta \qquad (2.2)$$

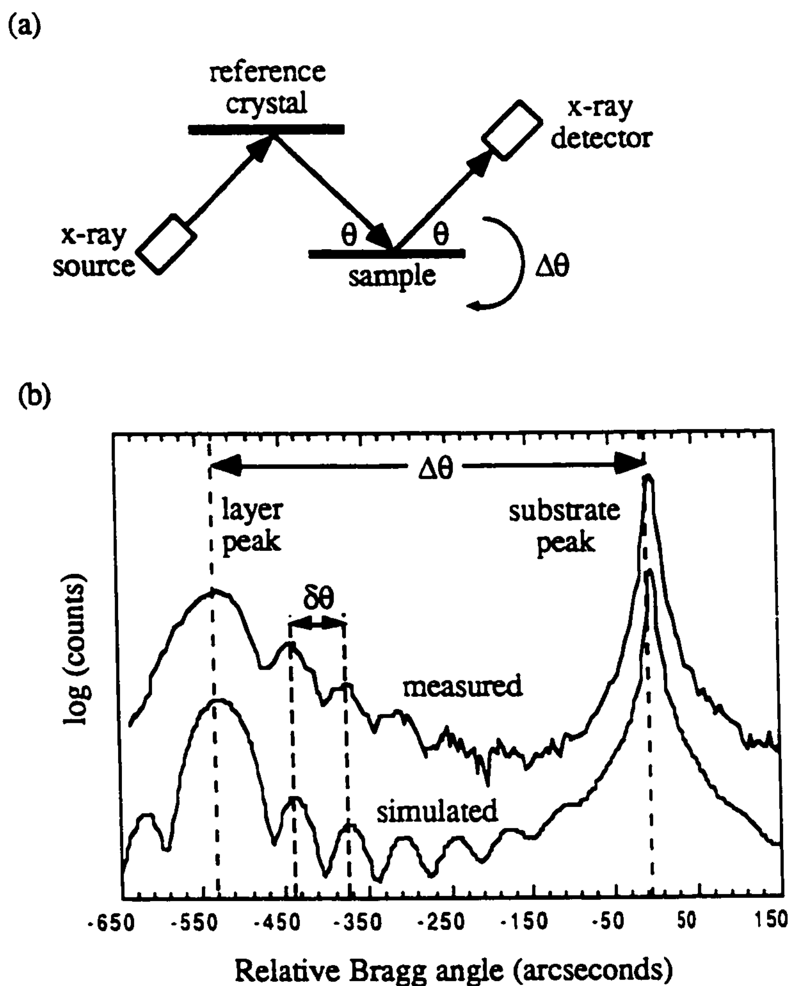

Fig. 2.3. Schematic of (a) the double crystal X-ray diffractometer, and (b) a typical (400) rocking curve.

where λ is the X-ray wavelength, $a_{\perp}$ is the perpendicular distance between diffraction planes, and θ is the diffraction angle. The diffractometer uses the Cu $K_{\alpha1}$ and $K_{\alpha2}$ X-ray

lines with wavelengths $\lambda = 1.541$ Å and 1.544 Å, respectively. When the Bragg angles of the specimen and the reference crystal are close, the $K_{\alpha 1}$ and $K_{\alpha 2}$ lines cannot be separated and the substrate and layer peaks simply broaden. Using $\lambda = 1.541$ Å and $a_{\perp} = 5.8690$ Å for InP in the Bragg law gives $\theta = 31.7$ °. By using the differentiated form of Bragg's law and taking account of the tetragonal distortion of the layer, the lattice mismatch of the unconstrained layer, $(\Delta a/a)_o$, can be related to the angular separation, $\Delta\theta$, of the layer and substrate peaks in the rocking curve [1.7]:

$$(\Delta a/a)_o = - (\Delta\theta \cot \theta) (1 + 2c_{12}/c_{11})^{-1} \qquad (2.3)$$

where c_{11} and c_{12} are elastic constants of the layer. The room temperature values of c_{11} and c_{12} for $In_{1-x}Ga_xAs_yP_{1-y}$ are determined from those of the binary constituents using Vegard's law [2.9]. Each InGaAsP composition can then be established by combining DCXRD measurements of lattice mismatch and PL bandgap determinations for thick (>1000 Å) layers [1.7]. Since the values of c_{11} and c_{12} depend on the InGaAsP composition, x and y, an iterative approach is required. The smallest splitting, $\Delta\theta$, which can be measured directly (without curve fitting) is about 25 arcseconds, or $(\Delta a/a)_o \approx 1 \times 10^{-4}$ Å.

Interference of X-rays diffracted from the layer interfaces produces so-called "Pendellosung fringes" in the rocking curve. The layer thickness, t, can be derived from the angular separation of the thickness fringes, $\delta\theta$, using [2.10]:

$$t = \lambda / 2\, \delta\theta \cos\theta \qquad (2.4)$$

where $\theta = 31.7°$ and $\lambda = 1.541$ Å. In all cases, the thickness derived from the interference

fringes was the same as that determined by a thickness profilometer.

2.3.3. Transmission Electron Microscopy

Cross-sectional samples for transmission electron microscopy (TEM) were made by mechanical polishing and subsequent thinning by Ar ion beam milling to achieve foil thicknesses of 1000 to 2000 Å. The samples were examined in a *Philips CM12* TEM microscope operating at 120 kV. Dark field and bright-field cross-sectional TEM micrographs were obtained under two-beam conditions along the [011] direction using diffraction vectors of **g** = 0 -2 2 and 400, and along the [0 -1 1] direction using diffraction vectors of **g** = 022 and 400, as illustrated in Fig. 2.4. The effects of atomic hydrogen on the epitaxial deposition, as discussed in chapter 4, were also evaluated by axial TEM observations of homoepitaxial growths on patterned InP substrates.

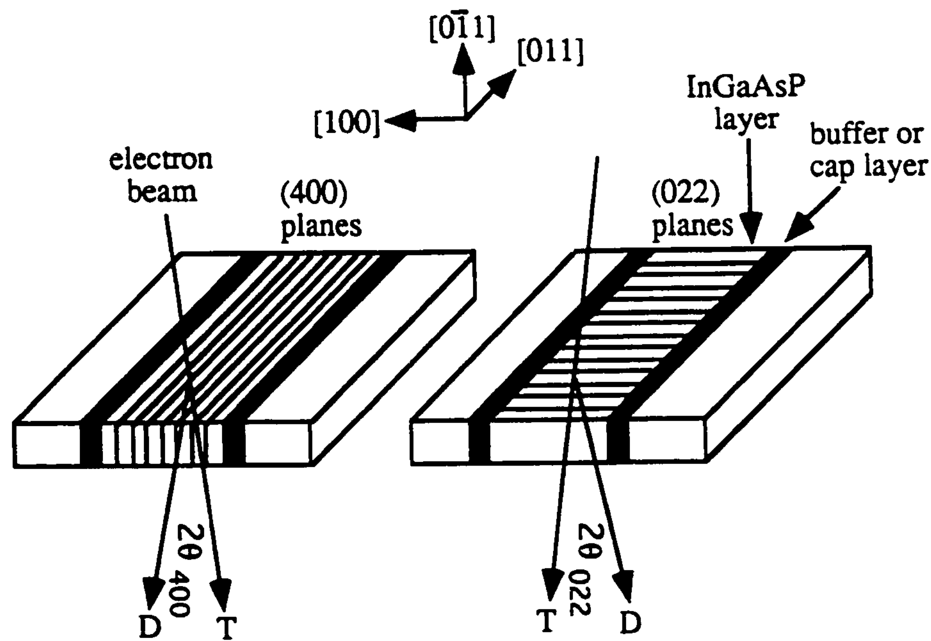

Fig. 2.4. Illustration of [0 -1 1] cross-sectional TEM foils under two-beam conditions with diffraction vectors of (a) **g** = 400 and (b) **g** = 022. Transmitted beams (T) form bright-field images whereas diffracted beams (D) form dark-field images.

CHAPTER 3

Lateral Composition Modulation in InGaAsP Strained Layers and Quantum Wells

This chapter investigates lateral composition modulation (LCM) in InGaAsP layers grown by gas source molecular beam epitaxy (GSMBE). The InGaAsP layers for this study were grown over a wide alloy range with lattice mismatches of -0.5% (compression), 0% (lattice-matched) and +0.5% (tension) using the sample structure shown in Fig. 3.1. In this way both thick layers (1500 Å) and quantum wells (50 Å) were studied from a single structure grown in the same run. The InGaAsP layers were grown using arsine flow fractions of 1 (InGaAs), 0.60, 0.36, 0.25, 0.15, 0.12 and 0.06. These flows gave nominal arsenic mole fractions in the solid of y = 1, 0.86, 0.69, 0.57, 0.38, 0.30 and 0.12, respectively, as indicated in Fig. 1.1. The InGaAsP layers were grown at 450 °C with a total hydride flow of 5 sccm giving a V/III flux ratio of about 2.6. The InP layers were grown at 450 °C with 4 sccm of PH_3 giving a V/III flux ratio of about 2. After growth the epitaxial layers were characterized by transmission electron microscopy (TEM), photoluminescence (PL) and double crystal X-ray diffraction (DCXRD). These techniques were reviewed in chapter 2.

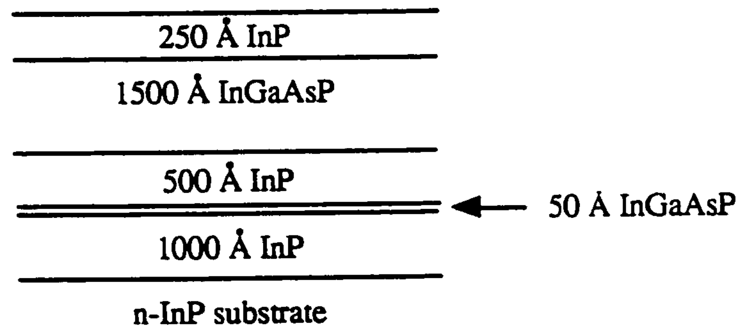

Fig. 3.1. Schematic of the sample structure (not drawn to scale) used for the studies in this chapter.

3.1. Transmission Electron Microscopy

Fig. 3.2 shows the dark-field [0 -1 1] cross-sectional TEM micrographs for the sample structure shown in Fig. 3.1, obtained with a diffraction vector of **g** = 022 for the -0.5% compressively strained samples labelled (a) to (c) in Fig. 1.1, and the +0.5% tensile strained samples labelled (g) to (j). Similar black-white contrast has been observed for lattice-matched samples [1.22, 1.23]. The strong contrast modulations are due to elastic relaxation of (022) lattice planes at the free surface of the sample foil [3.1, 3.2] due to the InAs-rich and GaP-rich regions. Larger contrast differences between the bright and dark regions are clearly observed for samples grown deeper within the miscibility gap of Fig. 1.1. In particular, tensile strained layers clearly show more compositional fluctuations as compared with the compressively strained layers. The size of the compositionally differentiated regions are on average about 100 Å in the [011] direction. Earlier work [1.22, 1.23] on lattice-matched samples showed the size of the compositionally differentiated regions in the [0 -1 1] direction to be about 1000 Å.

Previous studies [1.22, 1.23] showed weak vertical striations in the [0 -1 1] cross-sectional TEM micrographs, using a diffraction vector of **g** = 400. This modulation was attributed to lateral variations in the [100] lattice parameter due to elastic accommodation of the tensile strained GaP-rich regions and the compressively strained InAs-rich regions within the bulk of each film. These vertical striations, and therefore each compositionally differentiated region, appeared to extend throughout the InGaAsP layer thickness from the buffer layer to the capping layer interface yielding a columnar microstructure. The finite length of the black-white contrast in the [100] growth direction for the micrographs in Fig. 3.2 are therefore believed to be an artifact caused by the intersection of the TEM foil surface with the wavy surfaces of each compositionally differentiated region.

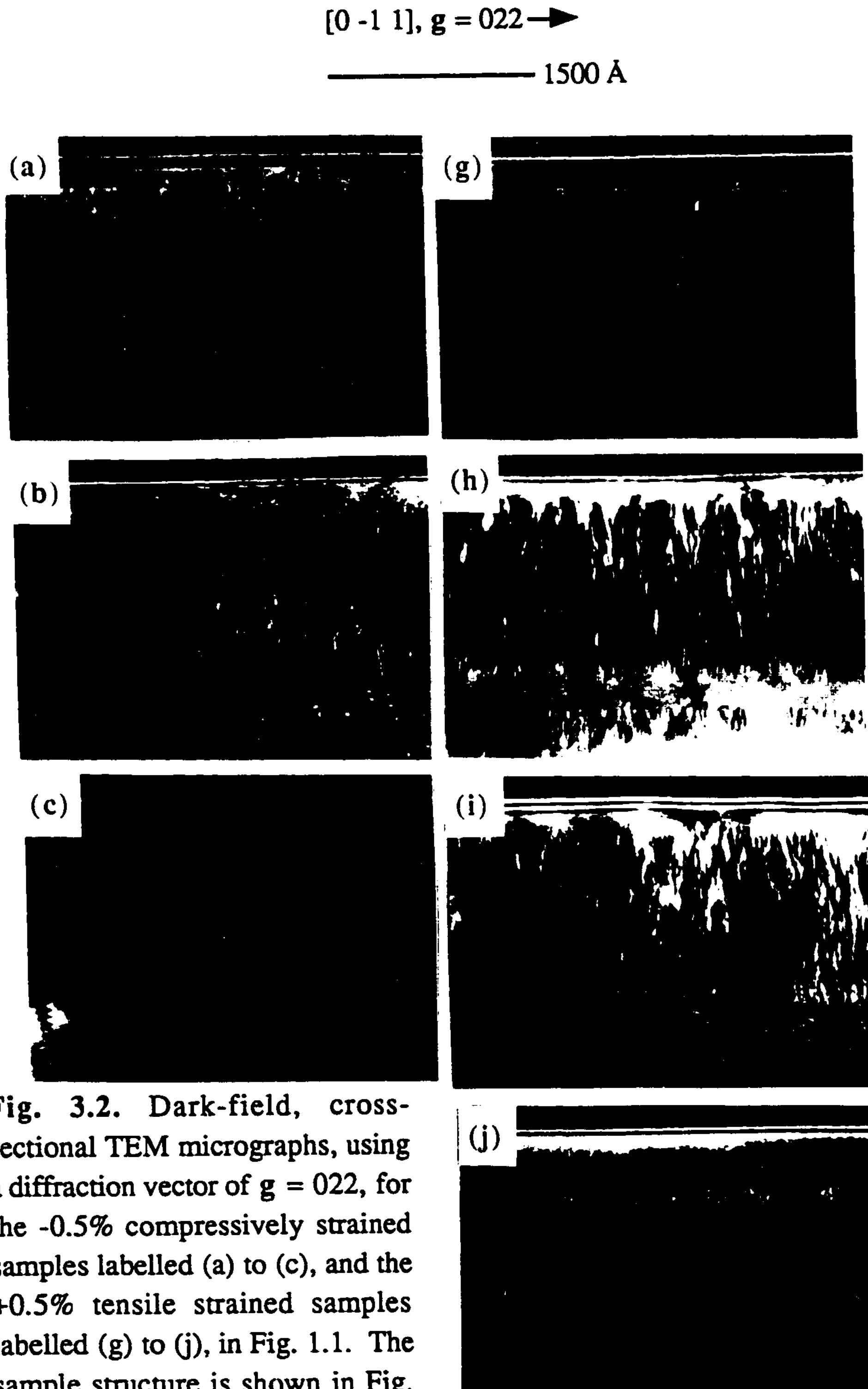

Fig. 3.2. Dark-field, cross-sectional TEM micrographs, using a diffraction vector of g = 022, for the -0.5% compressively strained samples labelled (a) to (c), and the +0.5% tensile strained samples labelled (g) to (j), in Fig. 1.1. The sample structure is shown in Fig. 3.1. The normal to the TEM foil surface is in the [0 -1 1] direction.

3.2. X-ray Diffraction

The full widths at half maximum (FWHM) of the DCXRD layer peaks for the 1500 Å thick layers were significantly broadened (140 arcseconds) for the tensile strained layers. In comparison, compressively strained and lattice-matched layers showed X-ray linewidths that were on average about 110 arcseconds over the entire alloy range in good agreement with the dynamically simulated value of 115 arcseconds. These results can be understood in terms of the variations in lattice constant produced by the InAs-rich and GaP-rich regions of the LCM structure which is more severe for tensile strained material grown deeper within the miscibility gap.

3.3. Photoluminescence from Thick Layers

Figs. 3.3 and 3.4 show the distribution of PL linewidths (FWHM) and integrated PL intensities, respectively, for the low temperature (11 K) and room temperature (300 K) PL spectra from the 1500 Å thick layers. The solid lines in Fig. 3.3 show the theoretical linewidths for band-to-band transitions in lattice-matched random InGaAsP alloys, due to thermal and alloy broadening [2.4, 2.5] as mentioned in chapter 2. Tensile strained (+ 0.5 %) samples which lie deeper within the spinodal isotherm have PL linewidths that are much larger than the theoretical broadening, and integrated PL peak intensities that are drastically reduced particularly at room temperature.

A comparison of the PL results with the TEM analysis shows that the PL linewidth broadening and reduction of the integrated PL intensity correlates with the severity of the composition modulation. The broadening of the PL peaks is therefore attributed to a variation in bandgap since the composition is inhomogeneous over dimensions that are small compared to the laser beam spot. The LCM also apparently increases non-radiative recombination, thereby reducing the integrated PL intensity. Although the non-radiative mechanisms are unknown at the present time, we can speculate that they may arise from point defects existing at the boundaries of the compositional fluctuations.

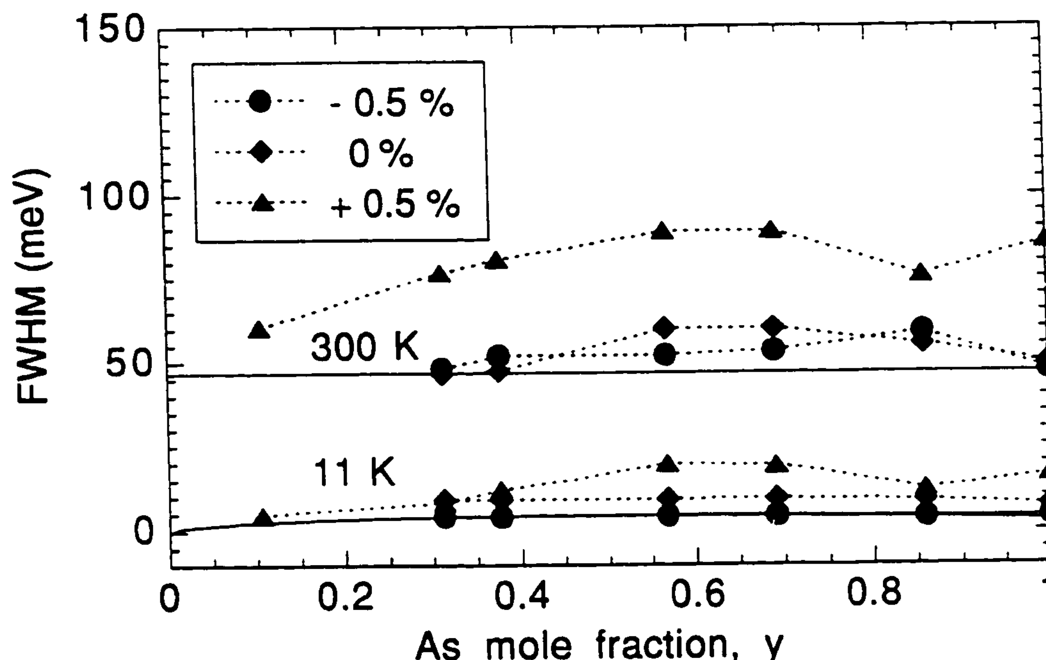

Fig. 3.3. PL linewidths (FWHM) at 11 and 300 K versus nominal composition for band-to-band transitions. These data points correspond to those in Fig. 1.1. The solid lines indicate theoretical linewidths for lattice-matched material, and the dashed lines are meant as guides to the eye.

A measure of the compositional variation is provided by the temperature-dependence of the PL peak energy. For example, PL spectra at various temperatures are shown in Fig. 3.5 for the 1500 Å thick layers with compositions labelled (a) to (i) in Fig. 1.1. The spectra have been normalized to unity in order to more easily compare differences among the samples, although one should bear in mind the variations in PL intensity evident in Fig. 3.4. The compressively strained samples labelled (a) to (c), as well as the lattice-matched sample labelled (f), have compositions that lie outside or nearly outside the spinodal isotherm. These samples exhibit a variation in peak energy and linewidth that is indicative of relatively homogeneous material. For these samples, the temperature-dependence of the bandgap, taken as the PL peak energy, can be described by the Varshni

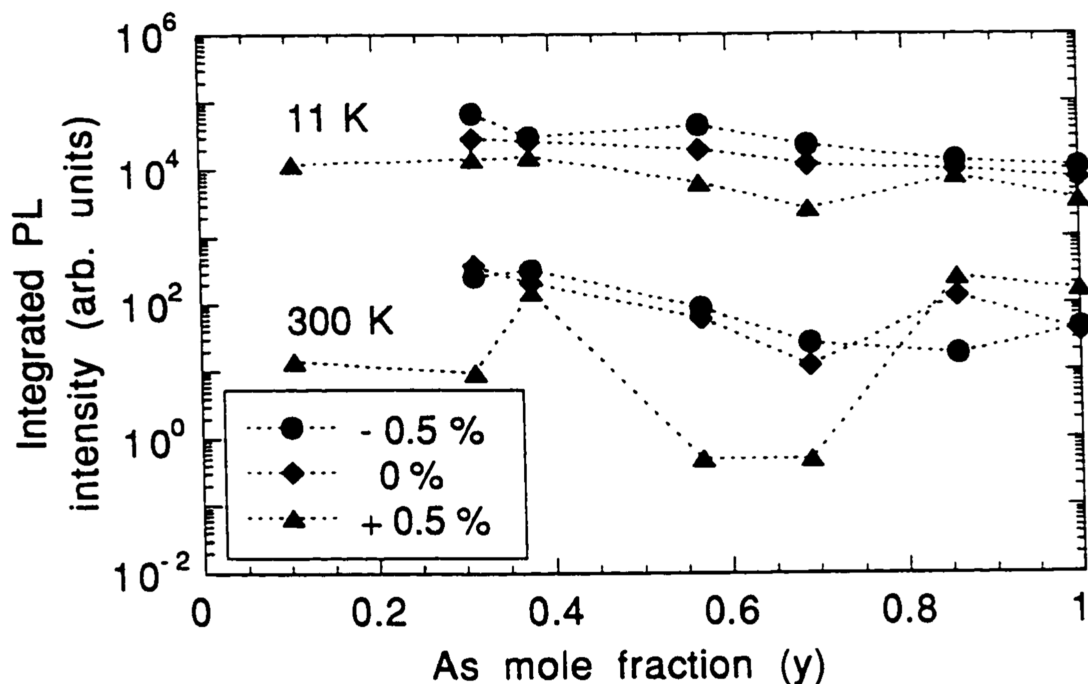

Fig. 3.4. Integrated PL intensities at 11 and 300 K versus nominal composition for band-to-band transitions. These data points correspond to those in Fig. 1.1. The dashed lines are meant as guides to the eye.

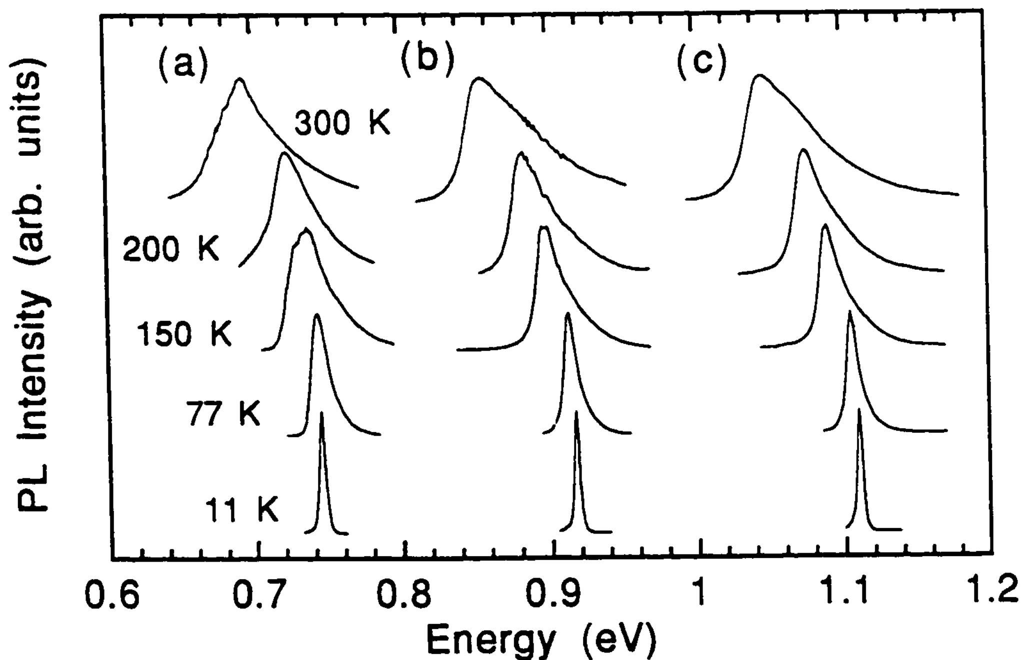

Fig. 3.5. Continued on next page.

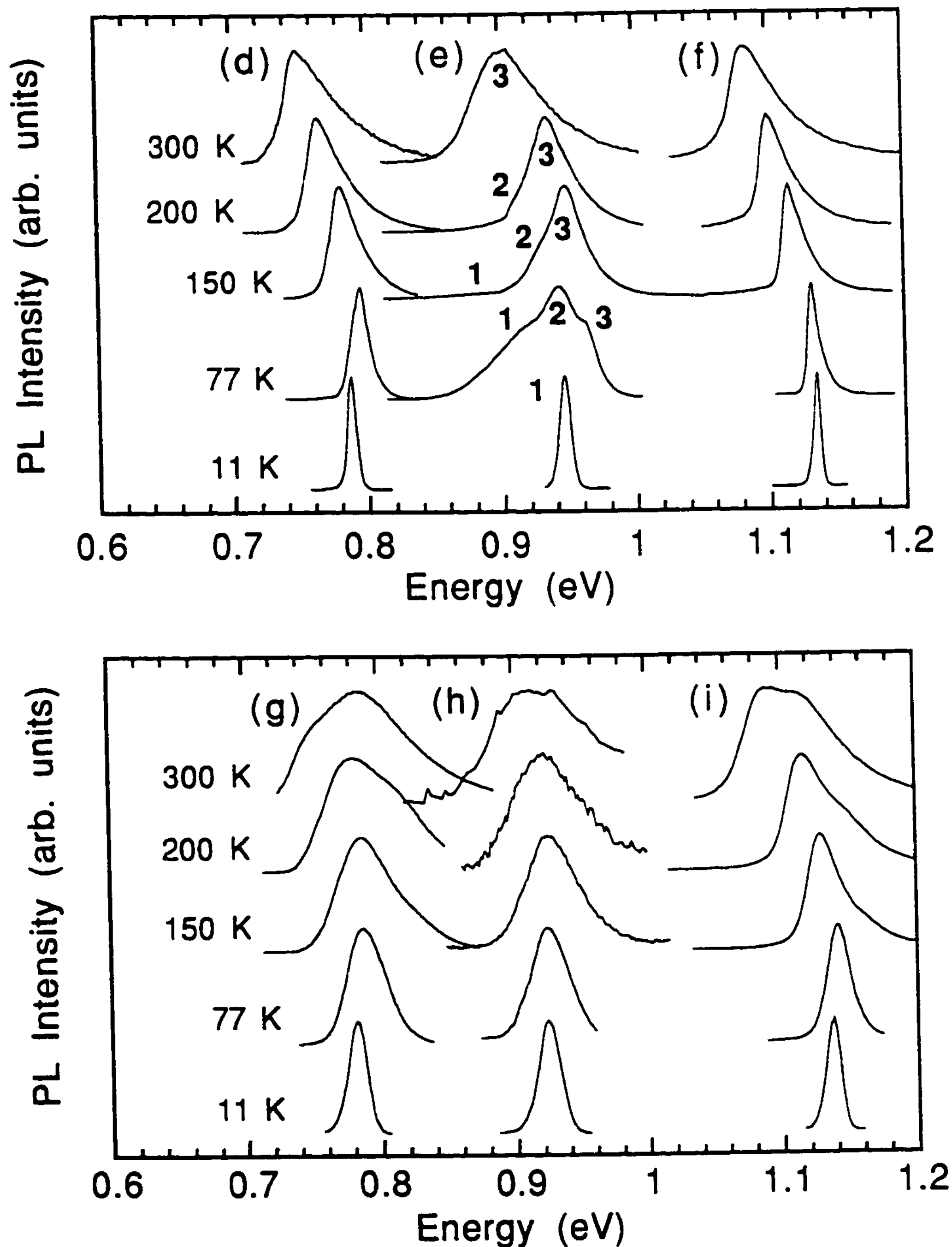

Fig. 3.5. Band-to-band PL spectra at various temperatures from samples (a) to (i) in Fig. 1.1 (continued from previous page). Peaks 1 to 3 are from InAs-rich regions, regions of nominal composition and GaP-rich regions, respectively, as discussed in the text.

Three PL peaks, however, are evident for the lattice-matched samples, such as (e) and nearby compositions ($0.57 \leq y \leq 0.86$), which lie deeper within the miscibility gap. These multiple peaks did not shift with excitation powers varying over three orders of magnitude, from 0.02 to 20 mW, and the intensity of the peaks varied linearly with excitation power over the same range. As well, at temperatures above about 150 K (when alloy broadening becomes insignificant) the high energy side of each peak can be approximated by a Boltzmann distribution, exp(-E/kT). These observations and the fact that the layers were not intentionally doped are evidence that the multiple peaks are not due to donor or acceptor transitions. The multiple peaks for the lattice-matched samples are therefore attributed to band-to-band recombination in InAs-rich regions (peak 1), regions of nominal composition (peak 2), and GaP-rich regions (peak 3), as indicated by the model in Fig. 3.6 [1.22, 1.23]. The PL from the tensile strained samples are discussed below.

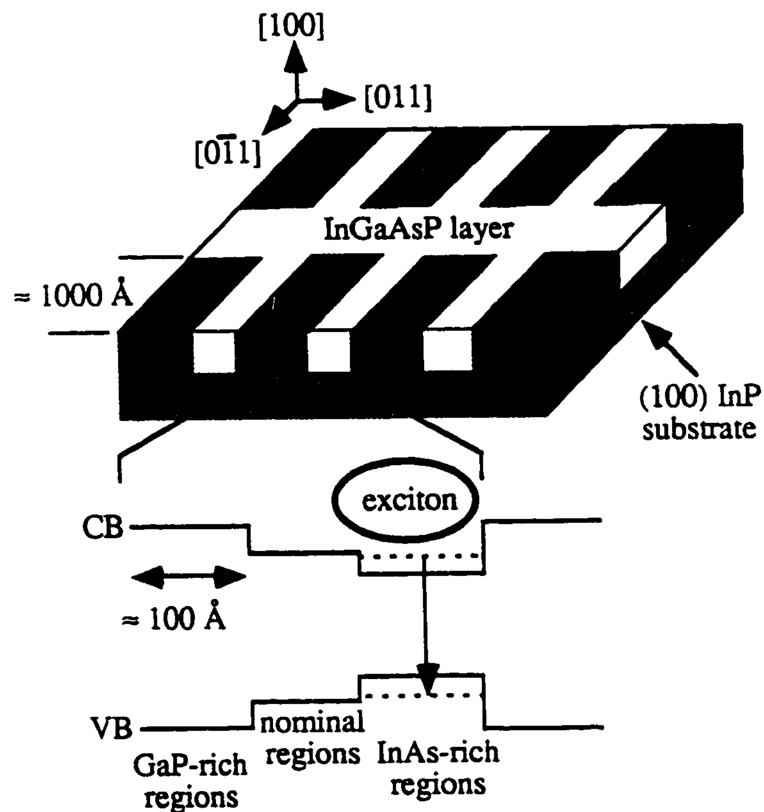

Fig. 3.6. Structural and corresponding bandgap model for the LCM.

Because the period of the LCM is much smaller than the carrier diffusion length (≈1 μm), the carriers become trapped after diffusing into the smaller bandgap InAs-rich regions at low temperatures. This results in a LCM-induced red-shift of the PL emission as compared with that expected for the average composition. As the temperature is increased, the carriers acquire enough energy to diffuse out of the InAs-rich regions, and carrier recombination in the nominal and GaP-rich regions contribute to the PL spectra. In a previous model of the LCM for nominally lattice-matched material [1.22, 1.23], the conduction band offset between the InAs-rich regions and the surrounding barrier material (nominal and GaP-rich regions) was estimated to be about 5 meV at 11 K with only a single electron energy level very close to the top of the laterally-defined well (assuming an average well width of 100 Å in the [011] direction). Since the thermal expansion coefficient increases with As content [2.9], the InAs-rich regions, coherent with the InP substrate, become even more compressively strained as the temperature increases. As a result, we speculate that a strain-induced hydrostatic shift of a few meV raises the electron energy level to the top of the InAs-rich well (that is, to the conduction band edge of the surrounding barrier material) as the temperature increases. This reduces the PL efficiency of the InAs-rich regions relative to the surrounding barrier regions as the PL measurement temperature increases. In addition, the carrier recombination lifetime is shorter in a light-hole band so the bulk recombination rate is greater in the tensile GaP-rich regions, where the light-hole band is pushed above the heavy-hole band [3.3]. As a result, PL from the GaP-rich regions dominates at room temperature in the lattice-matched material.

Because tensile strained samples are grown deeper within the miscibility gap, the driving force for LCM is greater so that the regions of nominal composition are expected to be consumed to become InAs-rich and GaP-rich regions by the phase separation process. Hence, two peaks, corresponding to the InAs-rich and GaP-rich regions, persist at room temperature, as demonstrated by samples (g) to (i) in Fig. 3.5. Linewidth broadening can smear these two peaks so that the spectra appear as single peaks that do not shift with temperature, as shown by sample (h). Because the compositional deviations are greater for

the tensile strained samples as compared to the lattice-matched samples, the conduction and valence band offsets between the InAs-rich regions and the surrounding GaP-rich barrier regions are relatively larger. The efficient recombination in the deeper InAs-rich wells and the short recombination lifetime in the GaP-rich regions cause both peaks to survive in the room temperature PL spectra of the tensile strained material. Comparing samples (e) and (i) in Fig. 3.5, higher temperatures are required for the tensile material before carriers can escape from the InAs-rich regions to the GaP-rich regions and recombine to produce peak 3. This is consistent with the deeper InAs-rich wells of the tensile strained material as compared to the lattice-matched material.

As discussed above, the LCM is accompanied by a red-shift of the low temperature PL peak energy due to recombination in the smaller bandgap InAs-rich regions, and a blue-shift of the room temperature PL peak energy due to recombination in the larger bandgap GaP-rich regions, as compared to the regions of nominal composition. As the blue-shift and red-shift increase with increasing LCM, the difference between the low temperature and room temperature PL peak energies, $\Delta E = E_g(11\text{ K}) - E_g(300\text{ K})$, becomes smaller than the value of 67 meV expected, over the entire alloy range, from the Varshni equation, Eq. (2.1). In fact, a plot of ΔE as a function of nominal composition, shown in Fig. 3.7, reveals a correlation consistent with the spinodal isotherm shown in Fig. 1.1. A solid line shows the bandgap difference of 67 meV expected from the Varshni equation which is roughly independent of composition. The deviations from the nominal composition (x, y) for the InAs-rich regions $(x - \Delta x, y + \Delta y)$ and the GaP-rich regions $(x + \Delta x, y - \Delta y)$ can then be roughly estimated by the excursions from $\Delta E = 67$ meV, using the model in Fig. 3.6 and the relationship between bandgap and composition in Fig. 1.1, as described previously [1.7, 1.22, 1.23]. The compositional fluctuations are assumed to occur directly toward InAs and GaP ($\Delta x = \Delta y$), as suggested by theoretical predictions [1.1, 1.2] and experimental observations [1.6]. The right-hand ordinate axis in Fig. 3.7 shows the

compositional deviations ($|\Delta x| = |\Delta y|$, or simply $|\Delta x|$ for InGaAs). The error bar represents the uncertainty in the compositional deviation due to the overlap and broadness of the multiple PL peaks. The compositional deviations are clearly greater for tensile strained compositions that lie deeper within the miscibility gap.

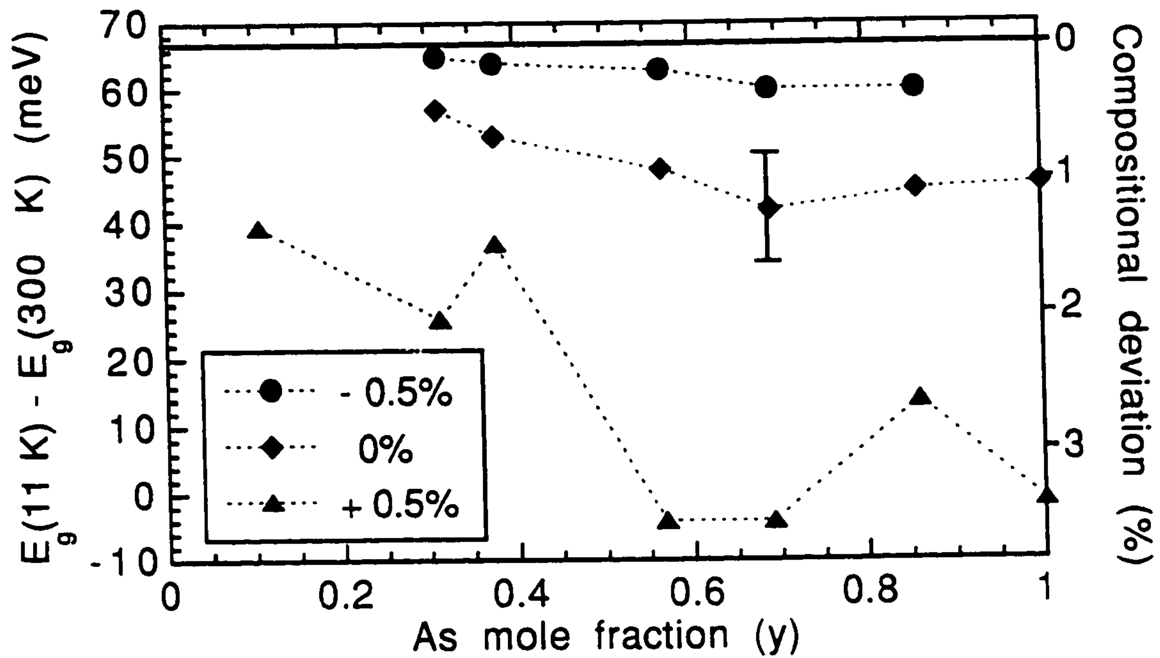

Fig. 3.7. Difference between low temperature (11 K) and room temperature (300 K) PL peak energies (left-hand scale), and the corresponding compositional deviations (right-hand scale), versus nominal composition for the PL spectra in Fig. 3.5. A solid line indicates the bandgap difference of 67 meV expected from the Varshni equation, the dashed lines are guides to the eye, and the representative error bar refers to the uncertainty in the compositional deviation.

3.4. Photoluminescence from Quantum Wells

Front surface PL spectra were obtained from the 50 Å InGaAsP QWs shown in Fig. 3.1 by wet chemical etch removal of the 250 Å InP cap layer and the 1500 Å

quaternary absorbing layer. Fig. 3.8 shows the distribution of low temperature (11 K) PL linewidths (FWHM) for e1-hh1 transitions in the 50 Å QWs with compositions indicated in Fig. 1.1. Tensile strained (+0.5 %) QWs which are grown deeper within the miscibility gap have greater PL linewidths than lattice-matched (0 %) or compressively strained (-0.5 %) QWs which is consistent with the thicker layers described earlier. The increase in linewidth with tensile strain persists in the room temperature PL (not shown). The solid curve in Fig. 3.8 shows the theoretical linewidth for fluctuations of one monolayer ($\Delta E = (\partial E/\partial Lz)*1$ ML) in a 50 Å QW [2.4]. The excess linewidth broadening is attributed to the fine-scale lateral composition modulations (≈ 100 Å) in the [011] direction which are smaller than the extension of the exciton (≈ 250 Å) in the plane of the QW [2.4].

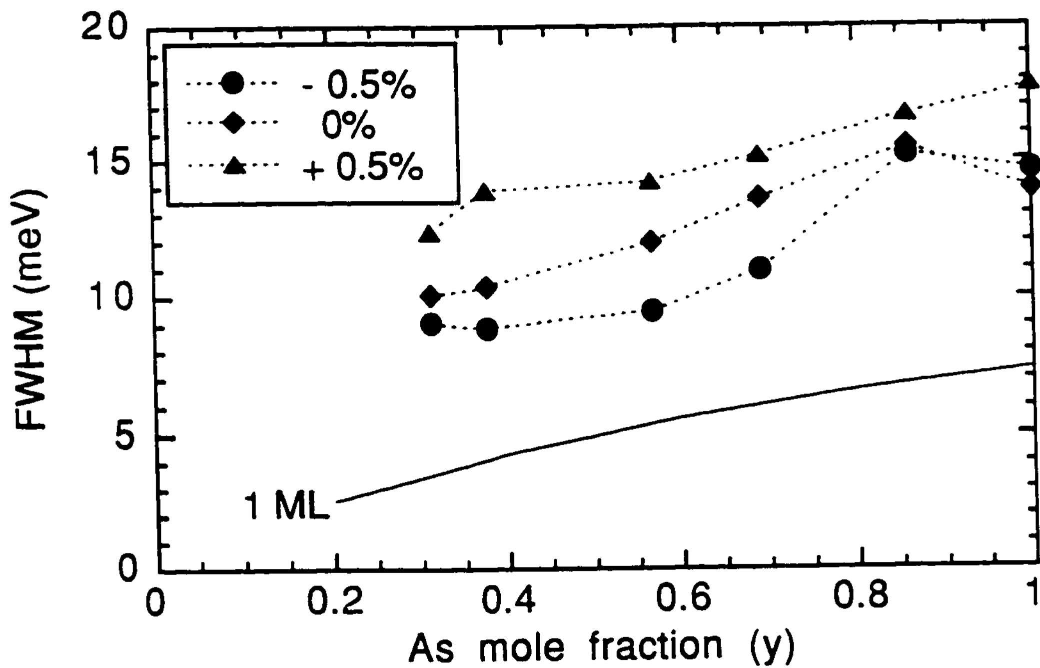

Fig. 3.8. PL linewidth (FWHM) versus nominal composition for the e1-hh1 QW transition at low temperature (11 K). These data points correspond to those in Fig. 1.1. The solid line indicates the theoretical linewidth due to interface roughness of one monolayer, and the dashed lines are guides to the eye.

The transition energy (e1-hh1) in QWs of homogeneous material is expected to increase monotonically with decreasing temperature according to the Varshni equation, Eq. (2.1), in the same fashion as the bandgap for thick layers. The compositional fluctuations in the QWs, however, result in a red-shift of the PL emission at low temperatures due to localization of the excitons in the potential minima associated with the smaller bandgap InAs-rich regions. Hence, the transition energies (e1-hh1) of the tensile QWs, such as (h), are significantly reduced at low temperatures from the expected energies which are indicated by the dashed lines in Fig. 3.9. The compressively strained QWs, such as (b), show a much smaller red-shift which is consistent with less LCM as described earlier for the thick layers.

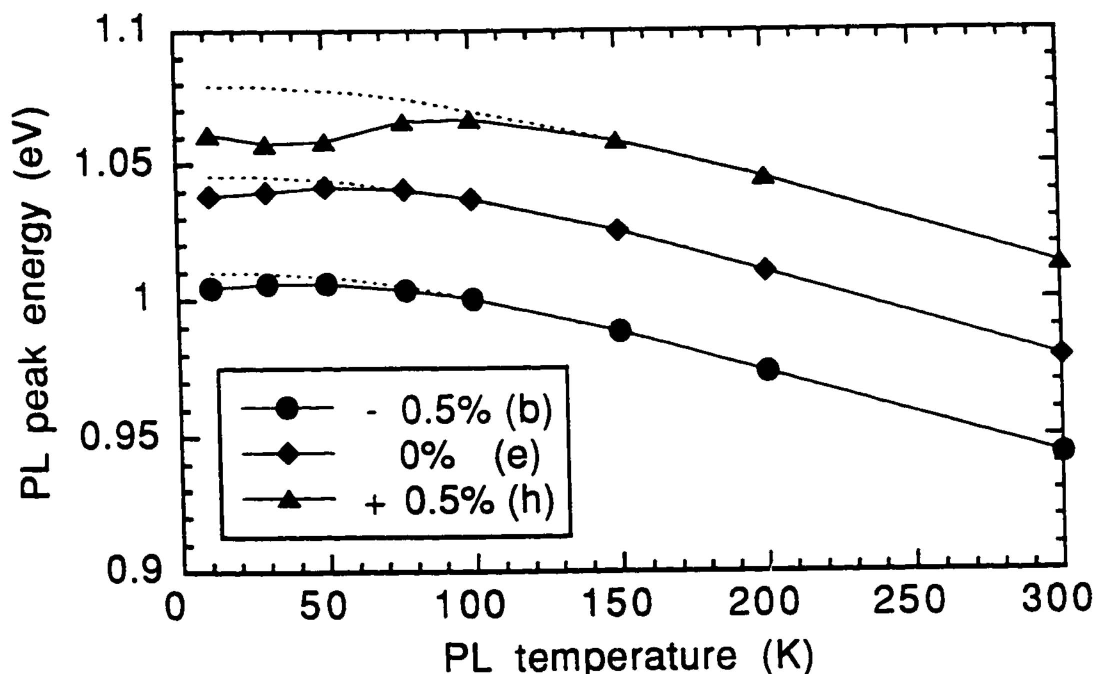

Fig. 3.9. Temperature-dependence of the PL peak energy for the e1-hh1 transition in the 50 Å QW of samples (b), (e) and (h) in Fig. 1.1. The dashed lines indicate the expected variation from the Varshni equation.

Further evidence that carrier recombination is occurring in a potential minimum of the QWs is provided by the power-dependence of the PL spectra at 11 K. Reduction of the excitation power from 20 mW to 0.125 mW resulted in an additional 5 meV red-shift of the PL peak energy for the tensile sample (h) as compared with only 1.8 meV for the compressive sample (b) and the lattice-matched sample (e). The change of the excitonic peak with excitation power has been described by Schubert et al [3.4]. Suppose τ_r is the recombination time and τ_c is the relaxation time for carrier migration into the potential minima of a QW. Since the recombination time decreases with increasing excitation intensity [3.4], at high excitation powers for which $\tau_r << \tau_c$ the carriers cannot migrate to the lowest energy sites of the QW before radiative recombination occurs. Relatively long recombination lifetimes ($\tau_r > \tau_c$), on the other hand, occur when the excitation intensity is low such that the carriers have an increased time to thermalize and recombine in the lowest energy sites of the QW. This results in a red-shift of the PL emission as the excitation intensity is lowered. The greater red-shift for the tensile strained QW is consistent with the larger compositional fluctuations as compared to that in the lattice-matched or compressively strained QW.

Assuming the nominal compositions of the QWs, the compressively strained sample (b) would be expected to have a much lower PL peak energy (about 70 meV lower) as compared with the tensile sample (h). This is approximately true in Fig. 3.9 for the QWs, but not at 11 K in Fig. 3.5 for the thicker quaternary layers due to the red-shifting associated with the LCM. Hence, the phase separation appears to be less for the thin QWs as compared to the thicker layers. This is in agreement with previous studies which showed that the phase separation process becomes more severe as the growth proceeds [3.5, 3.6].

The increase in LCM with layer thickness was investigated further by PL studies of lattice-matched $In_{0.72}Ga_{0.28}As_{0.61}P_{0.39}$ layers having a composition indicated by C

(square) in Fig. 1.1. PL linewidths and peak energies were studied as a function of temperature and layer thickness, and compared with theoretical expectations. The sample structure consisted of a 1000 Å InP buffer layer followed by 50, 100 and 500 Å thick layers of InGaAsP separated by 500 Å InP barrier layers, and finished with a 500 Å InP cap layer.

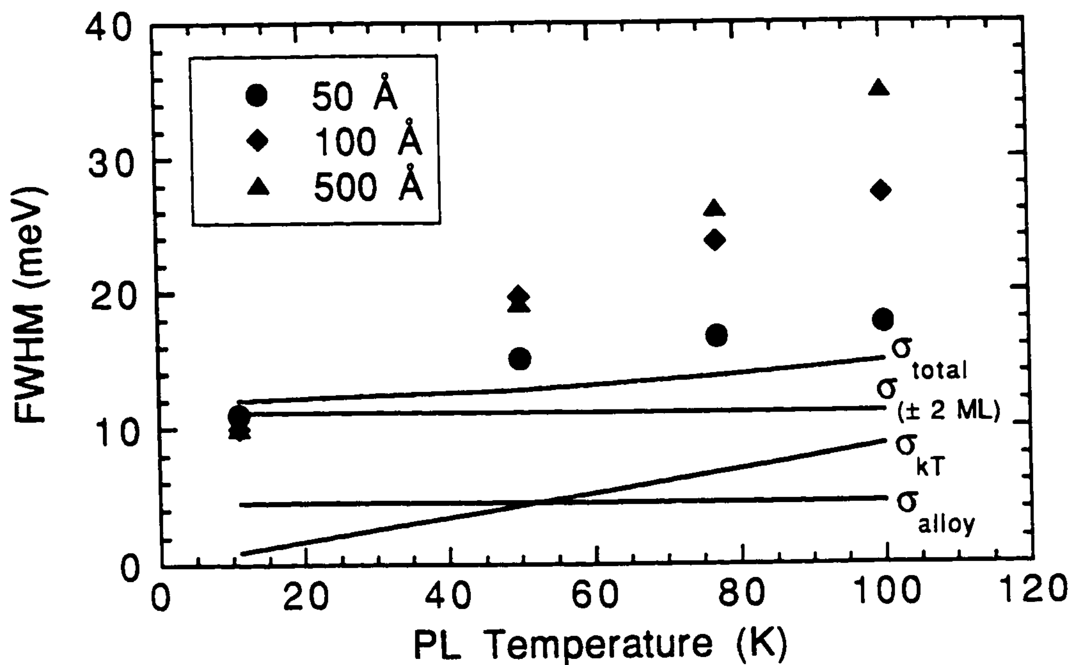

Fig. 3.10. Temperature-dependence of the PL linewidth (FWHM) for the e1-hh1 transitions in lattice-matched $In_{0.72}Ga_{0.28}As_{0.61}P_{0.39}$ layers with thickness 50, 100 and 500 Å. The solid lines indicate the contributions of alloy disorder (σ_{alloy}), thermal broadening (σ_{kT}) and interface roughness of 2 monolayers ($\sigma_{(\pm 2\ ML)}$) to the total theoretical linewidth (σ_{total}).

Fig. 3.10 shows the PL linewidths (FWHM) as a function of temperature obtained from the $In_{0.72}Ga_{0.28}As_{0.61}P_{0.39}$ layers. The thick lines indicate the contributions of alloy

disorder (σ_{alloy}), thermal broadening (σ_{kT}) and interface roughness of 2 monolayers ($\sigma_{(\pm 2\,ML)} = (\partial E/\partial L_z)\cdot L_z$) to the total theoretical linewidth (σ_{total}), as described in chapter 2 and elsewhere [2.4, 2.5]. The interface roughness of height L_z = 2 monolayers ($\sigma_{(\pm 2\,ML)}$) was observed in the top interface of the 50 Å QW using high resolution TEM as described elsewhere [3.7]. The linewidths for the 50 Å QW show only a slight broadening at higher temperatures with respect to the theoretical curve, σ_{total}. In comparison, a dramatic increase in linewidth is observed with increasing temperature for the 100 and 500 Å layers, suggesting an increase in LCM with layer thickness. Multiple PL peaks were not observed, however, indicating less LCM as compared to the 1500 Å layer (sample (e)) studied earlier.

3.5. Discussion

Despite the successes of the bulk spinodal model in Fig. 1.1, none of the existing theories of phase separation can account for all of our observations. For example, theory shows [3.8] that the composition modulations in the bulk should occur along the elastically soft directions which are the <100> directions, not the <011> directions, for the zincblende lattice considered in this work. Furthermore, when the effects of elastic strain energy induced by the substrate and the compositionally differentiated regions are considered, the growth temperature of 480 °C is found to be greater than the critical temperature above which the LCM is expected to be unstable along either <100> or <011> directions [3.7-3.12].

The spatial dimensions of the composition modulation were observed to be larger in the [0 -1 1] direction as compared to the [011] direction [1.22, 1.23]. This anisotropy in the orientation of the LCM structure is consistent with the greater surface adatom diffusion length in the [0 -1 1] direction as compared to the [011] direction on the (2x4) reconstructed

(100) surface, where the surface atomic arrangement is anisotropic [3.13]. Reducing the growth temperature and increasing the group V overpressure were previously found to decrease the LCM in GSMBE-grown layers [1.22, 1.23]. Kinetic limitations, whereby the surface adatom diffusion lengths are reduced via decreased growth temperature or increased group V overpressure, therefore limit the ability of the system to achieve equilibrium resulting in less LCM. In addition, the substrate surface orientation has been shown to influence the amount of LCM [3.14]. Finally, the observations in this work and elsewhere [3.15-3.17] have shown that the influence of elastic strain with the substrate must also be considered. This is demonstrated by sample (g) which exhibits relatively severe LCM despite having a composition that lies nearly outside the bulk miscibility gap. All of these observations indicate that the compositional fluctuations are undoubtedly caused by two-dimensional phase separation occurring on the surface during growth.

3.6. Chapter Conclusions

TEM, PL, and DCXRD have been used to characterize GSMBE-grown InGaAsP layers and QWs. For the 1500 Å thick layers, greater PL and DCXRD linewidths and larger phase contrast in TEM micrographs have indicated greater LCM in tensile strained material as compared with lattice-matched or compressively strained material. Multiple PL peaks observed in a temperature-dependent PL study have been interpreted in terms of emission from InAs-rich and GaP-rich regions. Similar results for the QWs have shown that the LCM plays a significant role in linewidth broadening and red-shifting of the low temperature PL emission. Comparison of bulk and QW results suggests that the LCM becomes more severe with layer thickness. Differences between the observed LCM structure and that predicted by bulk models, and the influence of growth conditions, substrate surface orientation and lattice mismatch strain on the compositional fluctuations, suggest the need for a surface model of the LCM.

CHAPTER 4

Argon Plasma-assisted and Atomic Hydrogen-assisted Epitaxy of InGaAsP Grown at Various Temperatures

In this chapter a new argon plasma-assisted growth technique will be shown to be an effective method for reducing the lateral composition modulation (LCM). Epitaxial layers of InGaAsP were grown on (100) InP substrates by gas source molecular beam epitaxy (GSMBE) over the temperature range 400-480 °C while simultaneously exposed to an Ar plasma stream. The role of atomic hydrogen within the plasma stream was subsequently investigated by using an independent atomic hydrogen source (AHS). This chapter is therefore divided into two sections dealing with argon plasma-assisted epitaxy in section 4.1 and atomic hydrogen-assisted epitaxy in section 4.2. Atomic hydrogen within the plasma stream will be shown to be the sole actor in reducing the LCM while the effects of other plasma species (for example, the argon ions) are negligible.

4.1. Argon Plasma-assisted Epitaxy

The Ar plasma stream was produced by electron cyclotron resonance (ECR) as described in chapter 2. A dc substrate bias of +40 V was used during the plasma-assisted growths to reduce the energy of the incident ion component of the plasma. Each structure grown by plasma-assisted epitaxy was compared to one grown by conventional epitaxy without plasma. InGaAsP samples were grown with compositions indicated by A and B in Fig. 1.1, as described below.

Sample A consisted of both thick layers and single quantum wells (QW) grown in a single structure similar to that in Fig. 3.1. Specifically, the sample structure consisted of a 1000 Å InP buffer layer, a 50 Å $In_{0.59}Ga_{0.41}As_{0.69}P_{0.31}$ QW, a 500 Å InP barrier or spacer layer, a 1000 Å $In_{0.59}Ga_{0.41}As_{0.69}P_{0.31}$ layer, and a 250 Å InP cap layer. The

InGaAsP composition (A in Fig. 1.1) is essentially the same as composition (h) where the LCM was shown in chapter 3 to be greatest. The InGaAsP growth temperature was varied from 400 to 480 °C, while the InP growth temperature was maintained at 450 °C. The InGaAsP layers were grown with 3.2 sccm of PH_3 and 1.8 sccm of AsH_3 giving a V/III flux ratio of about 2.6, while the InP layers were grown with 4 sccm of PH_3 giving a V/III flux ratio of about 2.

Sample B consisted of a 50 Å, tensile strained (1.5%), $In_{0.31}Ga_{0.69}As$ QW on a 1000 Å InP buffer layer, followed by a 250 Å InP cap layer. The InGaAs composition is indicated as B in Fig. 1.1. The InGaAs and InP layers were grown at 455 °C with a V/III flux ratio of about 2.

The optical properties of samples A and B were studied by photoluminescence (PL). In addition, double crystal X-ray diffraction (DCXRD) studies were performed on sample A using a symmetric (400) diffraction condition at room temperature. Finally, transmission electron microscopy (TEM) studies were performed on a special sample grown at 470 °C, consisting of alternating layers (each 1000 Å thick) of plasma-assisted and conventionally grown $In_{0.59}Ga_{0.41}As_{0.69}P_{0.31}$ layers (composition A in Fig. 1.1), for comparison of the two growth techniques.

4.1.1. Transmission Electron Microscopy

Fig. 4.1 shows the dark-field [0 -1 1] cross-sectional TEM micrographs, using diffraction vectors of g = 022 and 400, for the comparative structure. The structure was grown at 470 °C and consisted of alternating layers of plasma-assisted and conventionally grown $In_{0.59}Ga_{0.41}As_{0.69}P_{0.31}$ layers indicated by the data point labelled A in Fig. 1.1. As discussed in chapter 3, the strong contrast modulations in the (022) micrograph are due to elastic relaxation of (022) lattice planes at the free surface of the sample foil caused by the InAs-rich and GaP-rich regions of the LCM structure [3.1, 3.2]. Faint vertical striations can also be observed in the (400) micrograph due to elastic accommodation of the

InAs-rich and GaP-rich regions in the [100] growth direction.

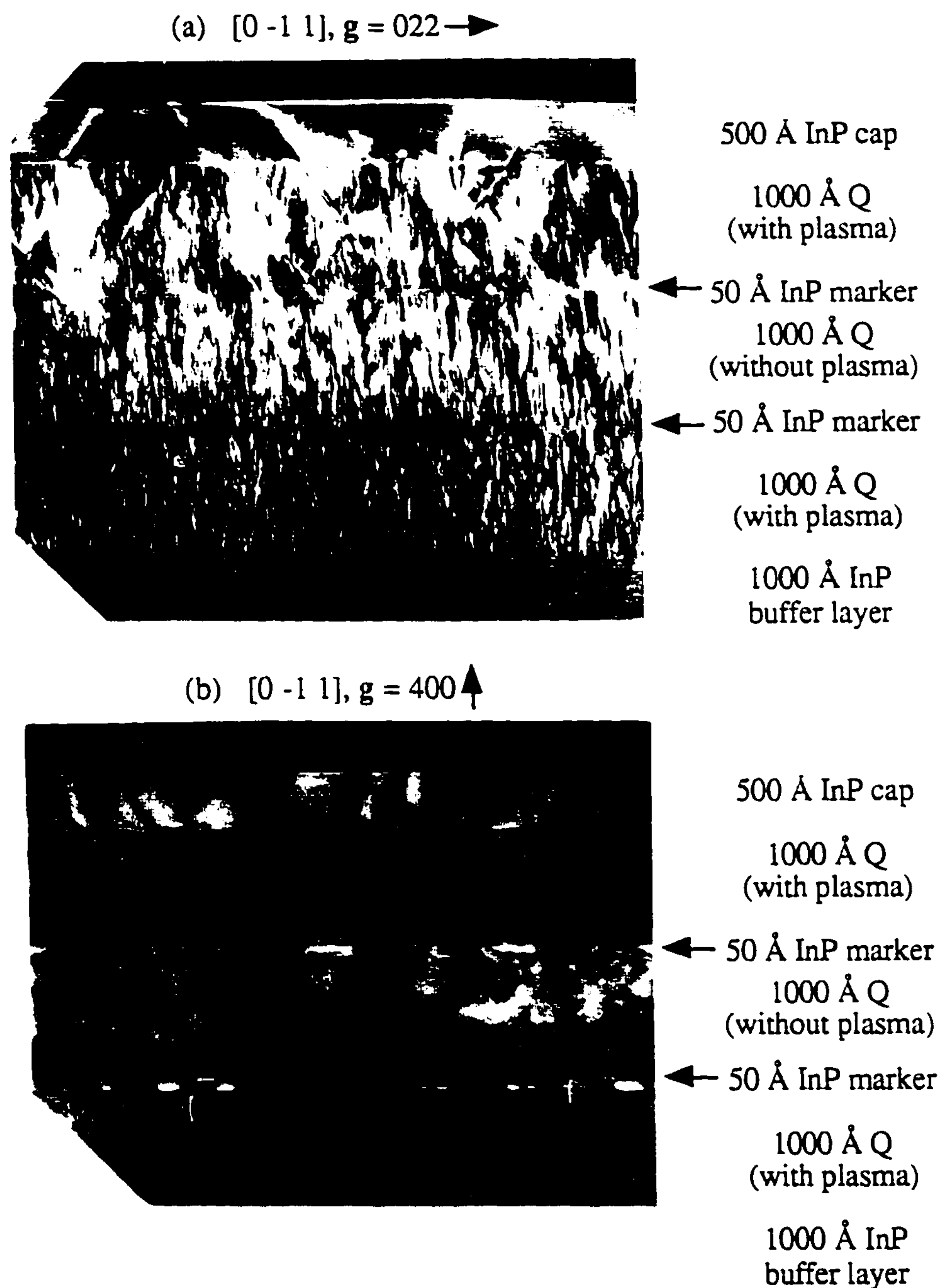

Fig. 4.1. Dark-field, cross-sectional TEM micrographs, using diffraction vectors of (a) g = 022 and (b) g = 400, for an $In_{0.59}Ga_{0.41}As_{0.69}P_{0.31}$ quaternary (Q) comparative structure. The normal to the TEM foil surface is in the [0 -1 1] direction.

While tensile strained InGaAsP layers grown by conventional epitaxy undergo relatively severe LCM resulting in roughening and faceting of the InGaAsP surface, plasma-assisted epitaxy produces relatively smooth layers with weaker striations in the (400) micrograph. A weaker black-white contrast in the (022) micrograph of the plasma-assisted layers also indicates less LCM. Relaxation of the top InGaAsP layer occurs as the critical thickness for dislocation formation is exceeded. The reduction in LCM provided by plasma-assisted epitaxy has also been confirmed by additional TEM observations, not reported here, of the individual InGaAsP layers that were used for the DCXRD and PL studies described below.

4.1.2. X-ray Diffraction

(400) DCXRD spectra of 1000 Å thick $In_{0.59}Ga_{0.41}As_{0.69}P_{0.31}$ layers (sample A) exhibited increased intensities and narrower linewidths for the plasma-assisted growths. A typical result is shown in Fig. 4.2 for growth at 480 °C. The sharp peak at 0 arcseconds is caused by (400) diffraction from the InP substrate and buffer layer while that at about 1500 arcseconds is caused by (400) diffraction from the tensile strained InGaAsP layer as described in chapter 2. Similar spectra were obtained at growth temperatures down to 400 °C. The sharper InGaAsP layer peak for the plasma-assisted growths can be understood in terms of a decrease in lattice parameter fluctuations due to a reduction in the LCM. The layer peak position did not change with growth temperature indicating the same composition in all cases.

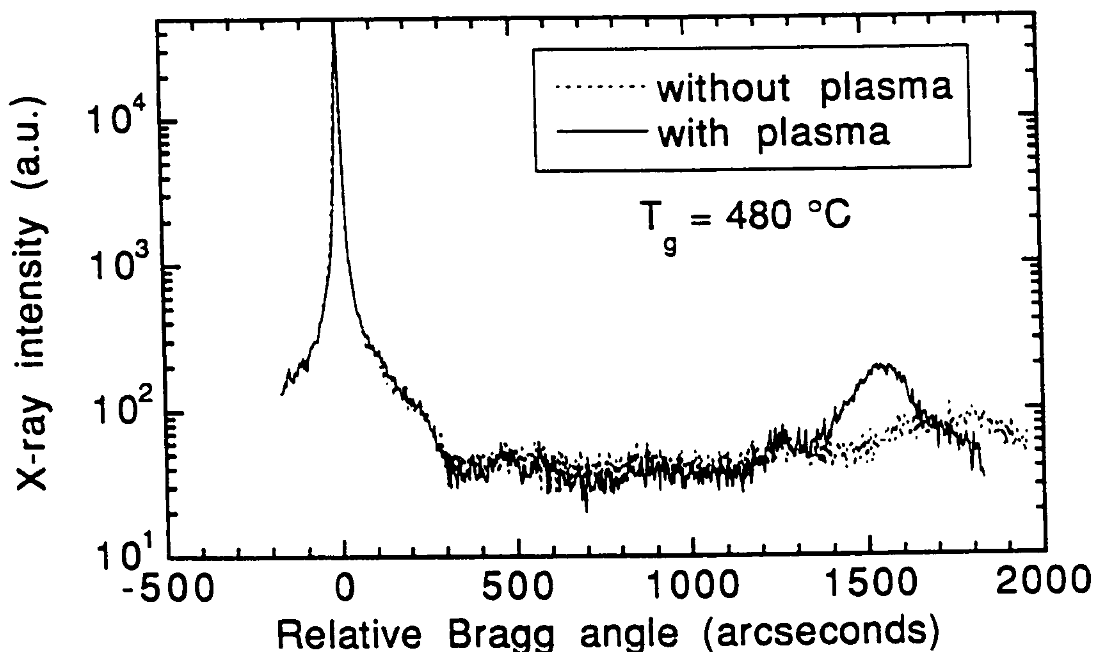

Fig. 4.2. Room temperature (400) DCXRD spectra from 1000 Å thick $In_{0.59}Ga_{0.41}As_{0.69}P_{0.31}$ layers (sample A) grown with and without Ar plasma at 480 °C.

4.1.3. Photoluminescence from Thick Layers

Low temperature (11 K) PL is shown in Fig. 4.3 for band-to-band transitions in 1000 Å thick $In_{0.59}Ga_{0.41}As_{0.69}P_{0.31}$ layers (sample A) grown with and without Ar plasma at various growth temperatures (400-480 °C). Fig. 4.3 shows a steady decrease (red-shift) in the PL peak energy as the growth temperature increases. However, Fig. 4.3 also shows that growth with the Ar plasma results in reduced red-shifts at all temperatures.

Figs. 4.4 and 4.5 show the growth temperature dependence of the full widths at half maximum (FWHM) and the integrated intensities, respectively, for the low temperature band-to-band PL spectra in Fig. 4.3 and the room temperature band-to-band PL spectra (not shown in Fig. 4.3). The room temperature linewidths for the 480 °C growths have been omitted since the PL intensity was extremely low in this case. The linewidth

decreases, and the integrated PL intensity generally increases, with decreasing growth temperature. However, the PL intensity is also seen to decrease slightly for growth temperatures below about 425 °C. This is probably associated with non-radiative point defects grown-in at these low growth temperatures [4.1-4.4]. However, growth with the Ar plasma results in reduced linewidths and increased PL intensities at all temperatures.

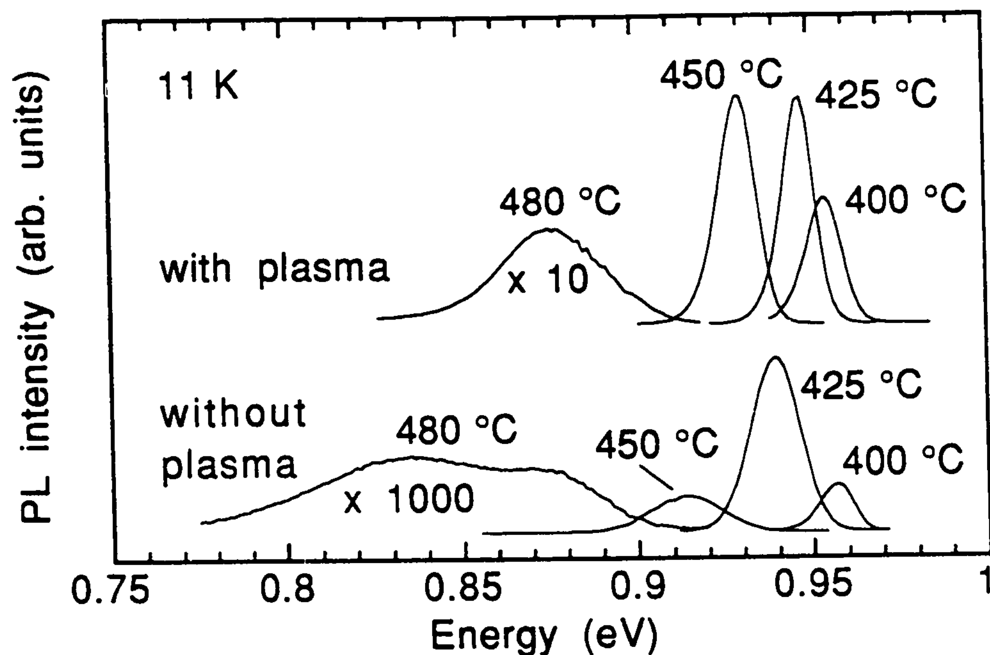

Fig. 4.3. Low temperature (11 K) band-to-band PL spectra from the 1000 Å thick $In_{0.59}Ga_{0.41}As_{0.69}P_{0.31}$ layers (sample A) grown with and without Ar plasma at various temperatures. The relative PL intensity for the spectrum at 480 °C is multiplied by 10 for the case with plasma and 1000 for the case without plasma. The other spectra are on the same scale.

Earlier studies in chapter 3 and elsewhere [1.22, 1.23] showed that as the LCM increases, a greater red-shift is observed in the low temperature PL peak energy due to recombination in the increasingly InAs-rich regions. These earlier studies also showed that

the PL linewidth increases and the integrated PL intensity decreases with increasing LCM. In this section we have observed that the red-shift and linewidth increase, while the integrated PL intensity decreases, with increasing growth temperature. This can be taken as an indication that the LCM increases with growth temperature as confirmed by earlier studies [1.23, 1.24]. In summary, epilayers with improved structural and optical characteristics can be achieved at all growth temperatures by using the Ar plasma-assisted MBE growth technique.

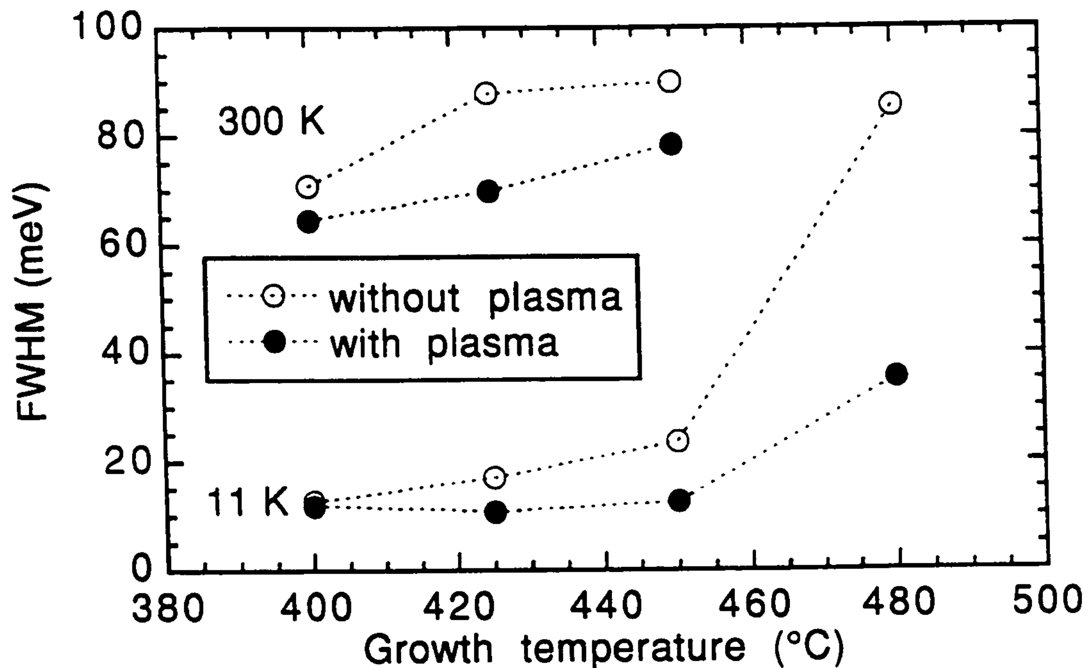

Fig. 4.4. Room temperature (300 K) and low temperature (11 K) band-to-band PL linewidths (FWHM) versus growth temperature from the 1000 Å thick $In_{0.59}Ga_{0.41}As_{0.69}P_{0.31}$ layers (sample A) grown with and without Ar plasma. The dashed lines are guides to the eye.

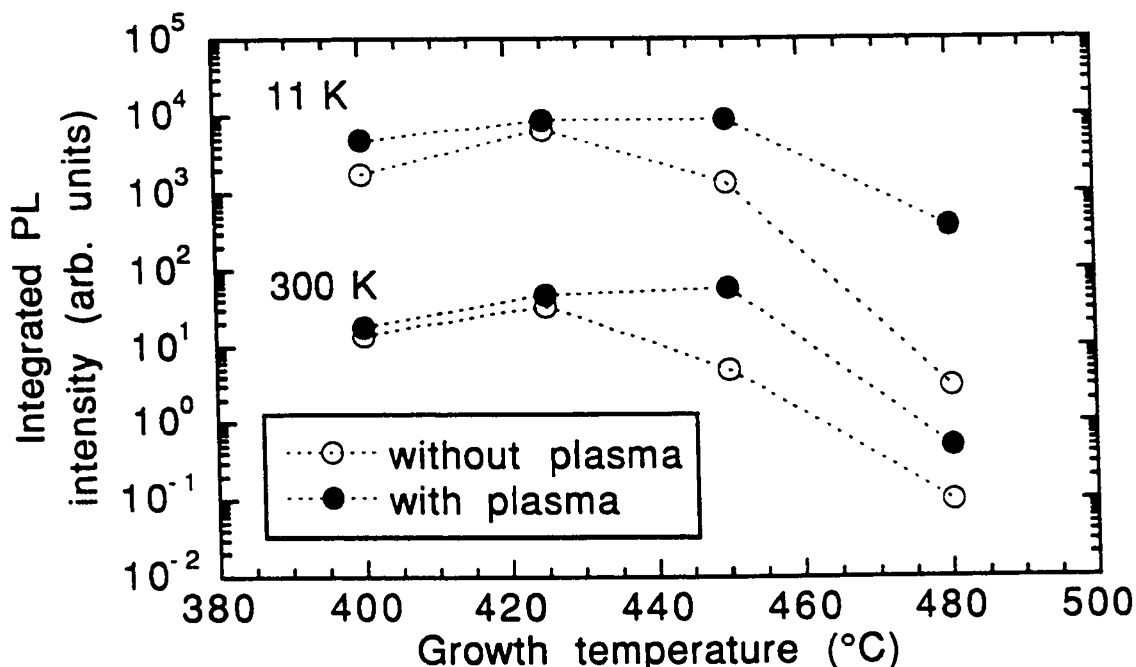

Fig. 4.5. Room temperature (300 K) and low temperature (11 K) integrated PL intensity versus growth temperature from the 1000 Å thick $In_{0.59}Ga_{0.41}As_{0.69}P_{0.31}$ layers (sample A) grown with and without Ar plasma. The dashed lines are guides to the eye.

4.1.4. Photoluminescence from Quantum Wells

PL studies were also performed on the single 50 Å $In_{0.59}Ga_{0.41}As_{0.69}P_{0.31}$ QWs (sample A) following wet chemical etch removal of the InP cap layer and the absorbing quaternary layer. Fig. 4.6 shows the PL peak energy shifts for the e1-hh1 transitions in the 50 Å QWs, measured with respect to the PL peak energies at room temperature. Similar to that observed previously in chapter 3, at low PL measurement temperatures the transition energies of the tensile QWs are significantly red-shifted from the expected energies (thick line) which are given at all growth temperatures by the Varshni equation, Eq. (2.1). This red-shift increases with growth temperature confirming an increase in

LCM. The plasma-assisted growths, however, show much smaller red-shifts in the low temperature PL peak energies, consistent with less LCM.

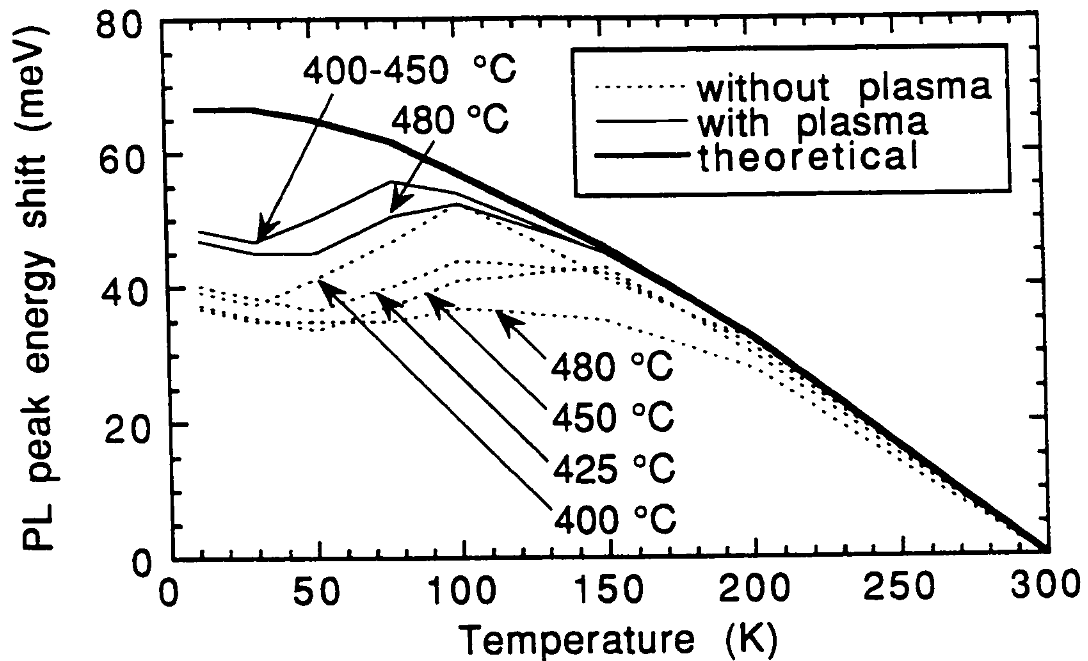

Fig. 4.6. Temperature-dependence of the PL peak energy shifts, measured with respect to the room temperature PL peak energies, from the 50 Å $In_{0.59}Ga_{0.41}As_{0.69}P_{0.31}$ QWs (sample A) grown with and without Ar plasma at various growth temperatures (400-480 °C). The thick line shows the expected variation from the Varshni equation.

Reduction in the room temperature PL linewidths of the 50 Å QWs are also evident in Fig. 4.7 for the plasma-assisted growths. In addition to sample A, plasma-assisted epitaxy was also evaluated at a growth temperature of 455 °C using a 50 Å $In_{0.31}Ga_{0.69}As$ QW (sample B). Although the 50 Å $In_{0.31}Ga_{0.69}As$ QW has a composition lying outside the miscibility gap, the layer has tensile strain (1.5%) which was shown in chapter 3 to result in significant LCM. Fig. 4.7 shows that the InGaAs QW exhibits an overall broader linewidth consistent with greater LCM, while growth by plasma-assisted epitaxy gives a

reduced linewidth, as well as a smaller red-shift (not shown).

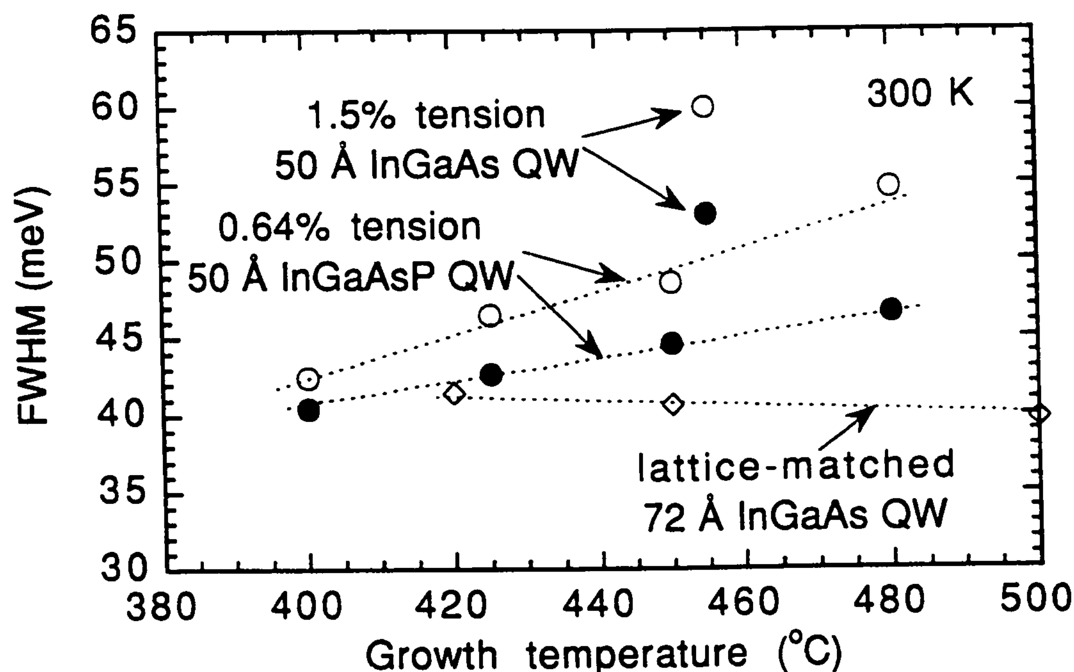

Fig. 4.7. Room temperature PL linewidths (FWHM) from 50 Å $In_{0.59}Ga_{0.41}As_{0.69}P_{0.31}$ QWs (0.64% tension, sample A) and $In_{0.31}Ga_{0.69}As$ QWs (1.5% tension, sample B) grown with (filled symbols) and without (open symbols) Ar plasma. Results from 72 Å lattice-matched $In_{0.53}Ga_{0.47}As$ QWs grown without plasma, as discussed in the text, are included for reference (diamonds). The dashed lines are guides to the eye.

Also included for reference in Fig. 4.7 are the linewidths from 72 Å lattice-matched $In_{0.53}Ga_{0.47}As$ QWs with lattice-matched 1.3 μm InGaAsP barriers for emission at 1.55 μm, as used in QW lasers for application in long-haul telecommunications. The growth temperature was varied from 420 to 500 °C for each InGaAs QW while the InGaAsP barriers were maintained at a growth temperature of 490 °C. The relatively narrow linewidths are evidence of less LCM in lattice-matched QWs, even at high growth

temperatures. Comparison with the tensile strained data confirms the correlation between LCM and tensile strain. Plasma-assisted epitaxy, however, allows the tensile strained layers to approach the quality of the lattice-matched layers by significantly reducing the LCM.

4.2. Atomic Hydrogen-assisted Epitaxy

Historically, the motivation for using plasma irradiation during epitaxial growth has been to enhance the adatom diffusion length via collisions with the energetic plasma species, thereby enabling the temperature for good epitaxial growth to be lowered [4.5]. However, in the case of gas source molecular beam epitaxy (GSMBE) the influence of atomic hydrogen on the epitaxial growth must also be considered. Thermodynamic analysis [2.1] indicates that a beam flux of less than 10^{-2} monolayer/s (ML/s) of atomic H is produced at a typical cracker temperature of 1000 °C and dimer flux of 1 ML/s. However, the ambient molecular hydrogen inherent in the GSMBE growth technique, may backflow into the ECR chamber during plasma-assisted epitaxy resulting in a significant flux of atomic hydrogen toward the growing surface.

As discussed in chapter 1, the role of atomic hydrogen in epitaxial growth, produced either by plasma or by thermal cracking, has been investigated by many authors. Some applications include low temperature oxide desorption, gettering of surface impurities during growth, defect or impurity passivation, and altered growth processes [1.25]. Growth in the presence of H has also been shown to produce less three-dimensional (3D) island growth and fewer dislocations in strained layer epitaxy [1.26-1.31], and to enhance the step flow growth on vicinal substrates [1.32-1.35]. Hence, the plasma/adatom interactions may be significantly influenced by the effects of atomic hydrogen on the surface. An understanding of plasma-assisted epitaxy therefore requires an unfolding of the kinetic effects associated with the plasma species (Ar and H). The amount of hydrogen required to sustain a pure H plasma was found to be too great for accurate compositional

control of P-based compounds due to reaction of atomic H with phosphorus on the growing surface [4.1]. Hence, to resolve the role of atomic hydrogen present in the Ar plasma, growths were done under an equivalent H flux produced by the thermal cracking of H_2 in a separate atomic hydrogen source. In this way, a plausible mechanism will be established for the improved layer quality described earlier in section 4.1.

The thermal H-exposed growths were performed using a cracker supplied by EPI [1.25], consisting of a tungsten filament operating at 1900 °C, as described in chapter 2. The PL quality of a lattice-matched $In_{0.72}Ga_{0.28}As_{0.61}P_{0.39}$ layer, with composition C in Fig. 1.1, was directly compared after a conventional, H-assisted and plasma-assisted growth. The sample structure consisted of a lattice-matched $In_{0.72}Ga_{0.28}As_{0.61}P_{0.39}$ layer grown 3000 Å thick on a 1000 Å InP buffer layer, followed by a 250 Å InP cap layer. The InGaAsP layers were grown at 480 °C with 3.8 sccm of PH_3 and 1.2 sccm of AsH_3 giving a V/III flux ratio of about 2.6. The InP layers were grown at 450 °C with a V/III flux ratio of about 2. The same sample structure, but with a 1 μm thick $In_{0.72}Ga_{0.28}As_{0.61}P_{0.39}$ layer, was used for TEM studies. The effect of H was also evaluated by TEM observations of homoepitaxial growths on pattern-etched InP substrates after conventional, plasma-assisted, and thermal H-exposed growths. Finally, reflection high energy electron diffraction (RHEED) streak patterns were observed *in situ* on an InP substrate as described below.

4.2.1. Transmission Electron Microscopy

Fig. 4.8 shows bright-field, [0 -1 1] and [011] cross-sectional TEM micrographs, using a diffraction vector of **g** = 022 and 0 -2 2, respectively, for a lattice-matched $In_{0.72}Ga_{0.28}As_{0.61}P_{0.39}$ layer (sample C), grown by conventional epitaxy (a, c) and with a H flux of 0.15 ML/s (b, d).

The $In_{0.72}Ga_{0.28}As_{0.61}P_{0.39}$ composition lies within the miscibility gap and is

therefore expected to be unstable, producing InAs-rich and GaP-rich regions with an associated black-white contrast in the TEM micrographs. This is clearly seen in Figs. 4(a) and (c) along with the expected anisotropy in the lateral dimensions of the LCM structure between the [0 -1 1] and [011] directions. The micrographs for the H-exposed growth, however, show weaker black-white contrast indicating less LCM as compared to that in the conventional growth. Also, the size of the compositionally differentiated regions appear somewhat smaller, particularly in the [0 -1 1] direction of the LCM structure (compare Figs. 4.8(c) and (d)), and less anisotropy is apparent. This will be discussed further in chapter 6.

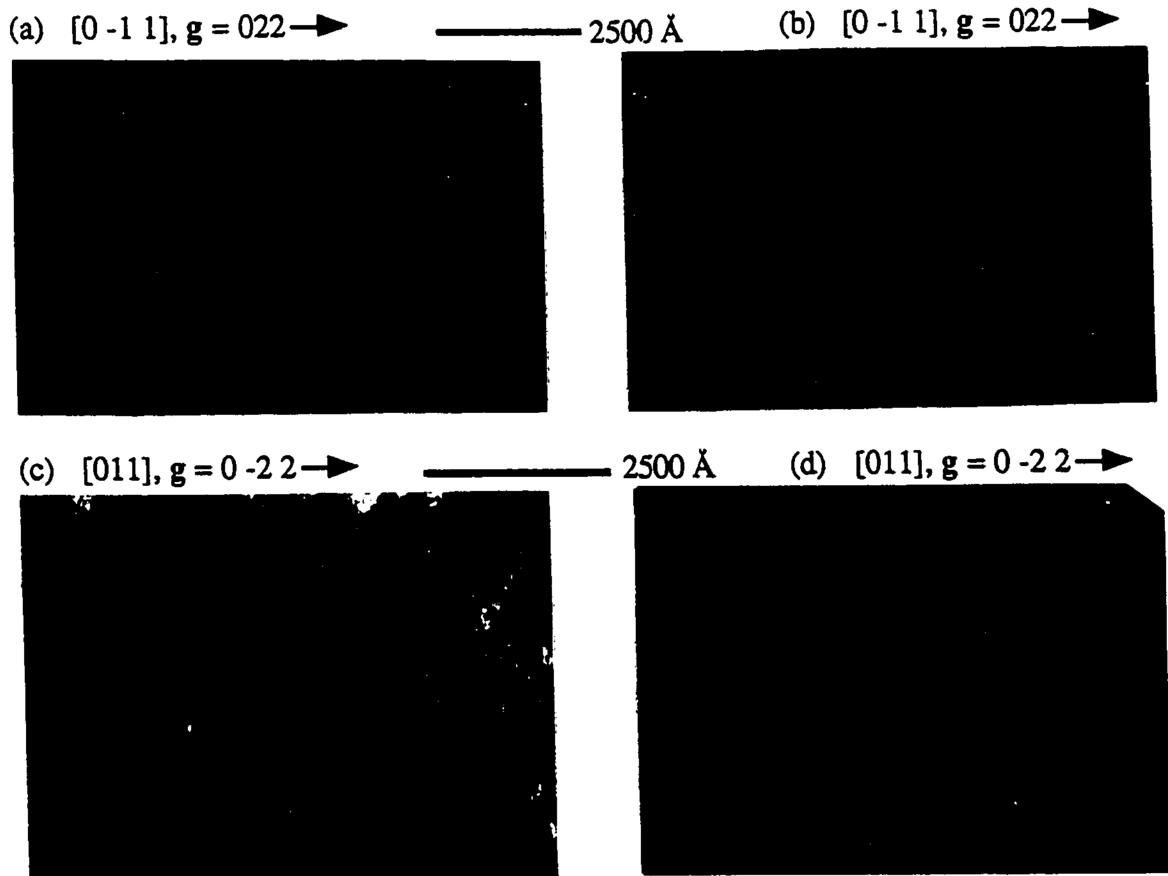

Fig. 4.8. Bright-field, cross-sectional TEM micrographs, using diffraction vectors of g = 022 and 0 -2 2, respectively, for a lattice-matched $In_{0.72}Ga_{0.28}As_{0.61}P_{0.39}$ layer (sample C) grown by (a, c) conventional epitaxy without H and (b, d) with a H flux of 0.15 ML/s. The normal to the TEM foil surface is in the [0 -1 1] or [011] direction as indicated.

4.2.2. Photoluminescence

In addition to the TEM studies described above, atomic hydrogen-assisted epitaxy was also assessed by PL measurement of the $In_{0.72}Ga_{0.28}As_{0.61}P_{0.39}$ layer (sample C). These results were then directly compared with those obtained by conventional epitaxy and by plasma-assisted epitaxy. The room temperature PL linewidths (FWHM) for band-to-band transitions in sample C are shown in Fig. 4.9 as a function of the atomic hydrogen flux. Fig. 4.9 also shows the red-shifts of the low temperature PL peak energies from the expected peak energies for these band-to-band transitions. The upper scale, indicating the H surface coverage, was estimated by RHEED observations as discussed below.

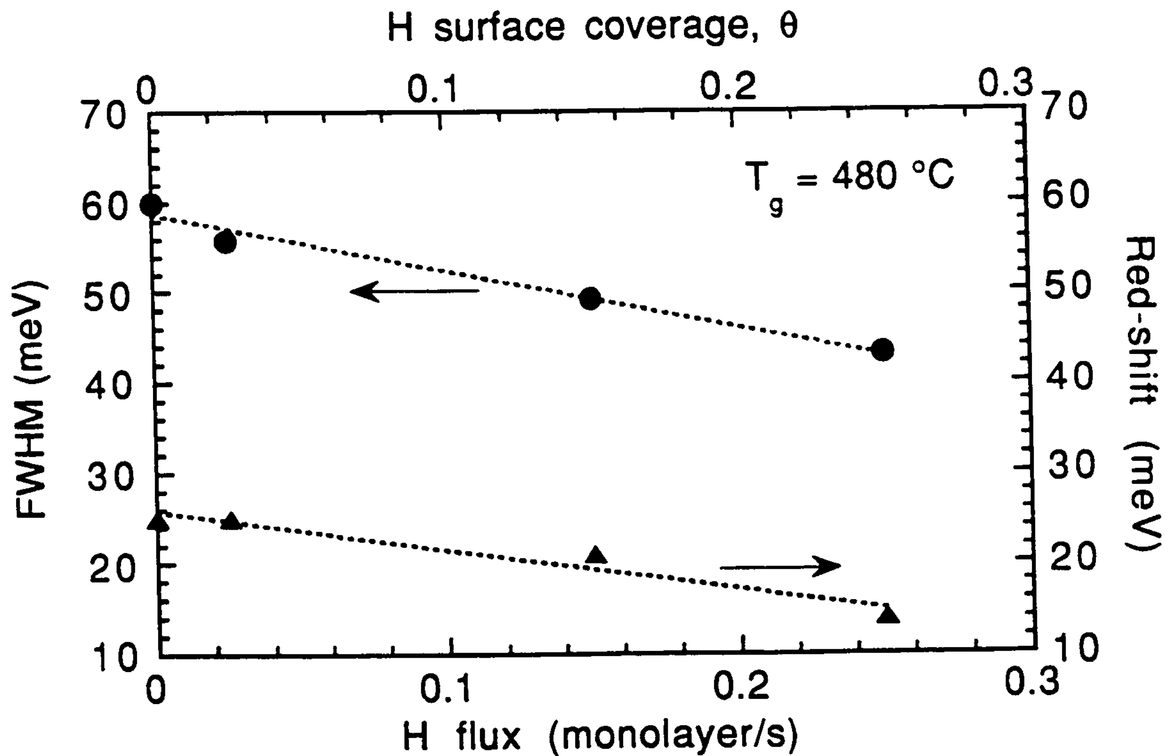

Fig. 4.9. Room temperature PL linewidths (FWHM) and the red-shifts of the low temperature PL peak energies, as a function of the H flux, for lattice-matched $In_{0.72}Ga_{0.28}As_{0.61}P_{0.39}$ layers (sample C).

The layers grown by conventional epitaxy, without plasma or atomic hydrogen, had room temperature PL linewidths of 60 meV and a red-shift of 25 meV, whereas relatively homogeneous samples with compositions that lie outside the miscibility gap would have linewidths close to the expected value of 47 meV and essentially no red-shift [1.22, 1.23]. The H-exposed growths have linewidths and red-shifts that are less than those of the conventional growth, indicating less LCM in agreement with the TEM observations above. The same sample grown by Ar plasma-assisted epitaxy showed linewidths of about 52 meV and a red-shift of 22 meV which would be consistent with a H flux of about 0.1 ML/s within the Ar plasma stream. It is therefore plausible that the improved layer quality obtained by plasma-assisted epitaxy may be attributed to atomic hydrogen. Further evidence to support this view is provided by homoepitaxial growths on patterned substrates and by *in situ* reflection high energy electron diffraction (RHEED) observations, as discussed below.

The reduction in LCM in sample C was not observed when only Ar gas (that is, no plasma) was admitted into the growth chamber via the ECR system nor when only molecular hydrogen was admitted to the AHS with the filament turned off. Varying the substrate bias from -40 to +80 V also had no effect on the degree of LCM during plasma-assisted epitaxy as measured by PL linewidths and red-shifts. The ion component of the plasma therefore seems to play a negligible role in the LCM reduction. The plasma only provides a way of cracking the ambient H_2 inherent in GSMBE via backflow into the ECR chamber.

4.2.3. Homoepitaxial Growths on Patterned Substrates

In order to examine the effect of atomic hydrogen on the adatom diffusion lengths, TEM micrographs of homoepitaxial growths on patterned InP substrates were performed after conventional, plasma-assisted, and thermal H-exposed growths. The substrates were patterned with a 2000 Å period grating, with grooves 400 Å deep oriented along the

[0 -1 1] direction, as typically used in distributed feedback lasers. The InP growths were marked every 120 Å with a 28 Å lattice-matched $In_{0.53}Ga_{0.47}As$ layer. Axial [0 -1 1] TEM micrographs shown in Fig. 4.10(a) indicate that growth by conventional epitaxy (without plasma or atomic hydrogen) resulted in a surface that was almost planar after the deposition of less than 500 Å of InP, while Fig. 4.10(b) indicates that the same growth with an atomic hydrogen flux of 0.1 ML/s is more conformal in that the surface partially maintained the grooved profile. On the other hand, the background H flux (0.025 ML/s), obtained with the cracker filament at 1900 °C but with no hydrogen supplied to the AHS gas manifold, had no effect. Conformality similar to the atomic hydrogen-assisted growth in Fig. 4.10 was obtained by a plasma-assisted growth (not shown).

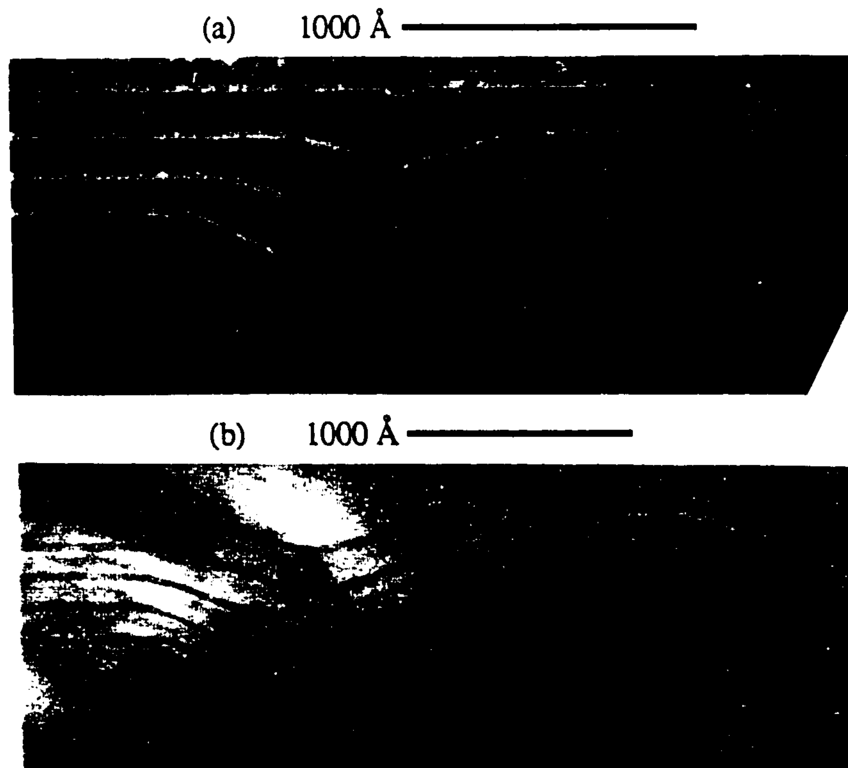

Fig. 4.10. Axial TEM micrographs of homoepitaxial growths on patterned InP substrates grown by (a) conventional epitaxy and (b) with a H flux of 0.1 ML/s. The normal to the TEM foil surface is in the [0 -1 1] direction.

Previous studies [1.22, 1.23] have shown that the LCM can be reduced by inhibiting the surface adatom diffusion length by growing at a reduced temperature or with a greater excess group V flux. Hence, the reduction in LCM obtained by plasma or H exposure is consistent with a reduction in the surface diffusion length of adatoms as confirmed by the patterned substrate growths. The studies in the previous section, however, show that atomic hydrogen-assisted epitaxy can provide a further reduction in LCM as compared to conventional epitaxy under otherwise identical conditions. In addition, non-radiative grown-in point defects associated with lower growth temperatures or greater group V overpressures can be avoided by using atomic hydrogen-assisted epitaxy under normal MBE growth conditions.

4.2.4. RHEED Observations

Reflection high energy electron diffraction (RHEED) observations were performed *in situ* using a 28 keV electron beam. A P-stabilized 2x4 RHEED streak pattern was observed for both a static or growing (1 μm/hr) InP surface at 460 °C. A clear 2x1 pattern, however, was observed under the same conditions but with a H exposure of 0.25 ML/s using the atomic hydrogen source. These observations are consistent with the surface model depicted in Fig. 4.11 where the missing phosphorus dimer row on the conventional surface is filled and accompanied by a H adsorption of 0.5 monolayer [4.6]. These surface models are discussed in chapter 6. RHEED observations during plasma-assisted epitaxy were also possible because the substrate bias and ECR magnetic fields could be temporarily removed while strong microwave absorption was maintained. A 2x1 streak pattern was also observed in this case under the same conditions as above, providing convincing evidence for the presence of atomic hydrogen in the plasma stream.

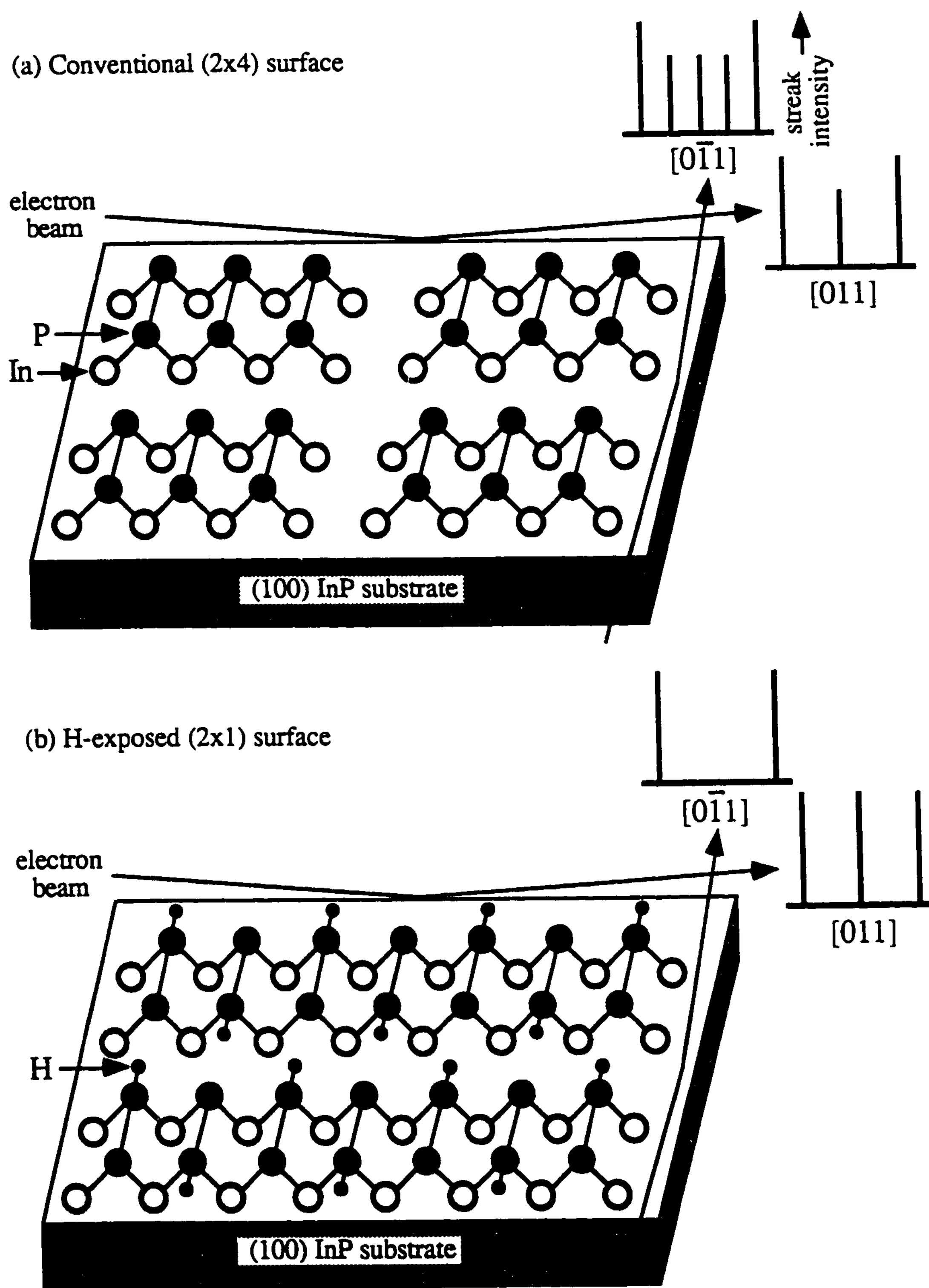

Fig. 4.11. Surface reconstructions and corresponding RHEED streak patterns obtained from (a) a conventional surface, and (b) a H-terminated surface.

The transition time required to produce the 2x1 RHEED pattern on a static InP surface at a substrate temperature of 460 °C, after opening the AHS shutter (with H flux set to 0.25 ML/s), was about 2 seconds. However, the transition time observed after opening the ECR shutter for the Ar plasma was about 5 seconds under the same conditions. Assuming the transition time is inversely proportional to the H flux, these values are consistent with the Ar plasma stream containing about 2/5 the H flux as that obtained from the AHS; that is, about 0.1 ML/s as also estimated from the photoluminescence results described earlier. Also, these transition times (2 and 5 seconds) are consistent with the time required to achieve roughly 0.5 ML of H for the 2x1 surface reconstruction (at 0.25 and 0.1 ML/s, respectively), assuming a negligible desorption rate of the H atoms.

The 2x (that is, the 2-fold symmetry) streak intensity weakened (that is, the 2x4 pattern "crept" back) as the substrate temperature was increased above 460 °C with the H flux maintained at 0.25 ML/s. This "weakening" of the 2x1 streak pattern indicates a reduction in the H surface coverage due to increased H desorption at the higher substrate temperature. Hence, both 2x1 and 2x4 reconstructions probably coexist on the surface under these conditions. The steady-state H surface coverage, θ, at 480 °C can be roughly determined by the RHEED estimate of the surface lifetime, τ_d, of the H atoms. This is given by:

$$\theta = F_H \tau_d \tag{4.1}$$

where F_H is the H flux (ML/s). Using RHEED, $\tau_d \approx 1$ sec was measured for the 2x1 to 2x4 transition on a static InP surface at 480 °C. The H surface coverages, shown in the upper scale of Fig. 4.9, are considered accurate to within a factor of about two due to uncertainties in the H_2 cracking efficiency and in the measurement of the H lifetime. As discussed in chapter 6, adatom migration lengths are expected to be less on 2x1 surfaces as compared to 2x4 surfaces. The reduction in LCM with increasing H flux may then be explained by a more complete 2x1 surface reconstruction as the H flux increases.

4.2.5. Diode Laser Studies

Double heterostructure (DH) broad-area diode lasers were grown with various active region compositions and growth temperatures to demonstrate an improvement in device performance with a reduction of the LCM. The DH laser diodes were grown on (100) oriented n-type InP substrates with symmetric 1.5 μm thick InP cladding regions grown at 450 °C. The n-type cladding region was uniformly doped with Si at $1x10^{18}$ cm^{-3}, while the p-type cladding region was uniformly doped with Be at $3x10^{18}$ cm^{-3}. A 2000 Å thick, p-type $In_{0.53}Ga_{0.47}As$ ohmic contact layer, doped $5x10^{18}$ cm^{-3}, was grown on top of the p-type cladding layer at 480 °C. An undoped InGaAsP active region was grown 1500 Å thick at a temperature of 480 °C and with bandgap wavelengths of 1.15, 1.3 and 1.55 μm. A DH laser with 1.3 μm emission was also grown at a lower temperature, 450 °C, for comparison with that grown at 480 °C. The InP layers were grown with 4 sccm of PH_3 giving a V/III flux ratio of about 2, while the InGaAsP layers were grown with a total group V flow of 5 sccm giving a V/III flux ratio of about 2.6, as in the earlier studies. The broad-area devices were fabricated with various stripe widths (10 to 70 μm), defined by wet chemical etch removal of a "spin-on" glass layer and subsequent metallization using standard photolithography procedures. Cavity lengths of 500 μm, oriented along the [011] direction, were obtained by cleaving.

Light-current (L-I) characteristics were measured under pulsed operation with a 4 μs pulse width and 500 Hz repetition rate giving a duty cycle of 0.2%. Current injection was provided by contact probes. Pulsed operation on a thermoelectric stage ensured a constant measurement temperature of 20 °C. Figs. 4.12 to 4.15 show the threshold current densities and slope efficiencies (slope of the L-I curve above threshold) obtained from the L-I characteristics of the DH lasers. The DH laser with 1.15 μm bandgap wavelength,

having an active region composition that lies outside the miscibility gap, showed the best characteristics (that is, the lowest threshold current densities and the highest slope efficiencies). In this case, the average threshold current density for stripe widths greater than 10 μm was about 4.5 kA/cm^2 with a corresponding slope efficiency of about 0.3 W/A which are among the best values reported in the literature for similar structures [4.7].

In comparison, the DH laser with 1.3 μm bandgap wavelength grown at 480 °C, has an active region composition that lies deepest inside the miscibility gap. Consequently, this laser showed the worst characteristics. However, Figs. 4.14 and 4.15 reveal that lasers with improved L-I characteristics may be obtained by lowering the growth temperature to 450 °C which is consistent with the reduction in LCM with decreasing growth temperature observed in chapter 3 and elsewhere [1.22, 1.23]. Finally, the DH laser with 1.55 μm bandgap wavelength showed L-I characteristics that were intermediate between those obtained above which is consistent with its composition in the miscibility gap relative to the 1.15 and 1.3 μm bandgap wavelengths. Hence, DH lasers with improved characteristics were obtained by reduction of the LCM.

The lasing threshold corresponds to the point at which the stimulated emission rate equals the loss due to scattering, absorption or emission from the laser. The increase in threshold current density and decrease in slope efficiency due to LCM occurs because of several reasons. First, the electrons and holes are distributed in energy over a broader range due to the composition modulation, and hence fewer electron-hole pairs are available per unit energy range for stimulated emission into the lasing modes at any given input current. Second, losses due to non-radiative recombination, and photon scattering out of the laser cavity due to surface roughness and compositional inhomogeneities [4.8], are increased by the LCM. As a result, compositions that lie deeper in the miscibility gap and show greater LCM, such as that with 1.3 μm bandgap wavelength, will have greater threshold current densities and lower slope efficiencies.

Double heterostructure (DH) broad-area diode lasers with an active region having bandgap wavelength of 1.3 μm were grown at 480 °C by conventional epitaxy and H-assisted epitaxy for comparison. H-assisted epitaxy was used only during growth of the InGaAsP active region. Figs. 4.16 and 4.17 show the threshold current densities and the slope efficiencies obtained from the L-I characteristics of these DH lasers. The DH laser grown by H-assisted epitaxy showed improved characteristics (that is, lower threshold current densities and higher slope efficiencies) as compared to the conventional growth without atomic hydrogen. This improvement is attributed to a reduction of the LCM by H-assisted epitaxy. The improvement is such that the performance of the 1.3 μm lasers is comparable to that of the 1.15 and 1.55 μm lasers where the LCM is much less severe.

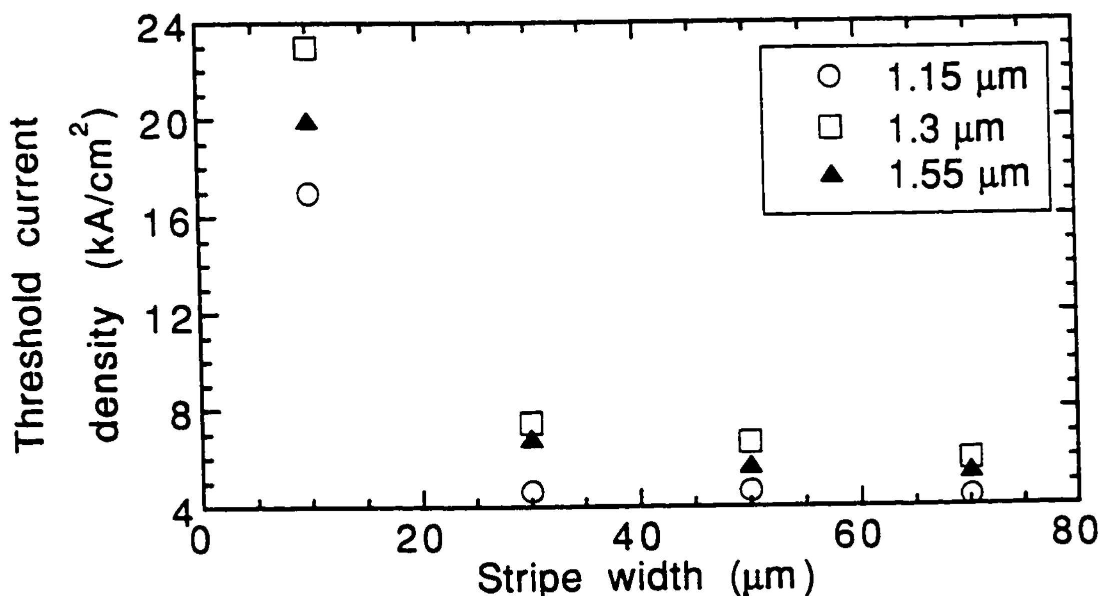

Fig. 4.12. Threshold current density versus stripe width for DH lasers with active regions having bandgap wavelengths of 1.15, 1.3 and 1.55 μm grown by conventional epitaxy at 480 °C.

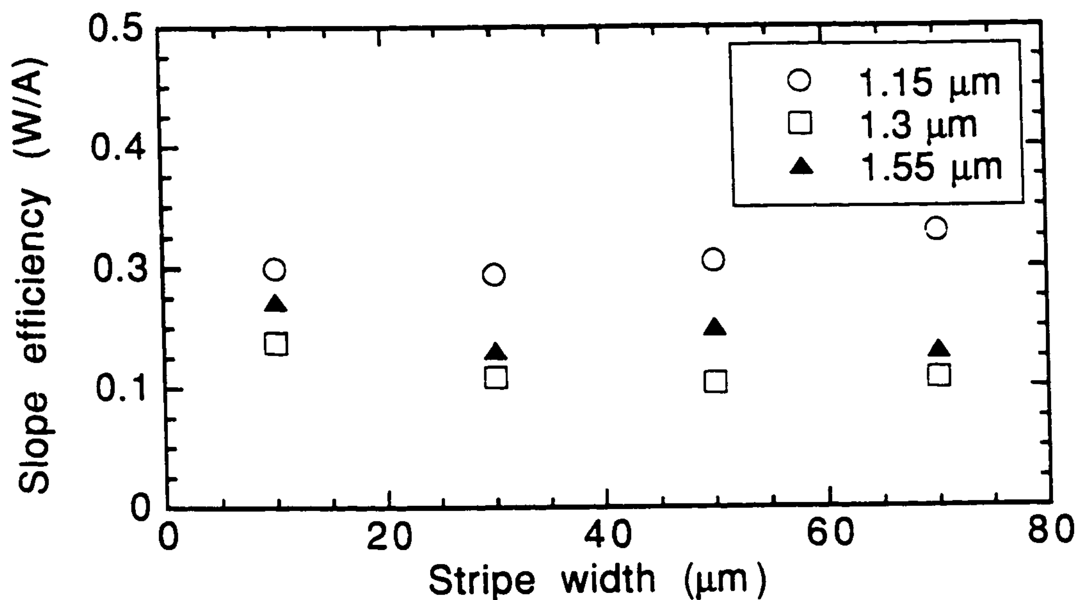

Fig. 4.13. Slope efficiency versus stripe width for DH lasers with active regions having bandgap wavelengths of 1.15, 1.3 and 1.55 µm grown by conventional epitaxy at 480 °C.

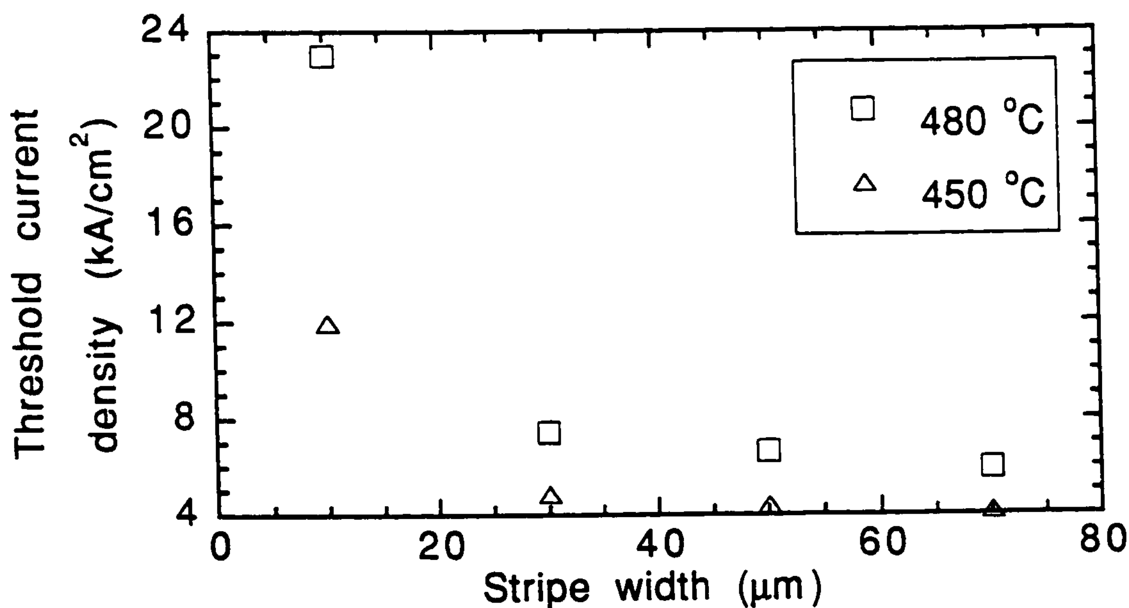

Fig. 4.14. Threshold current density versus stripe width for DH lasers with an active region having a bandgap wavelength of 1.3 µm grown by conventional epitaxy at 450 and 480 °C.

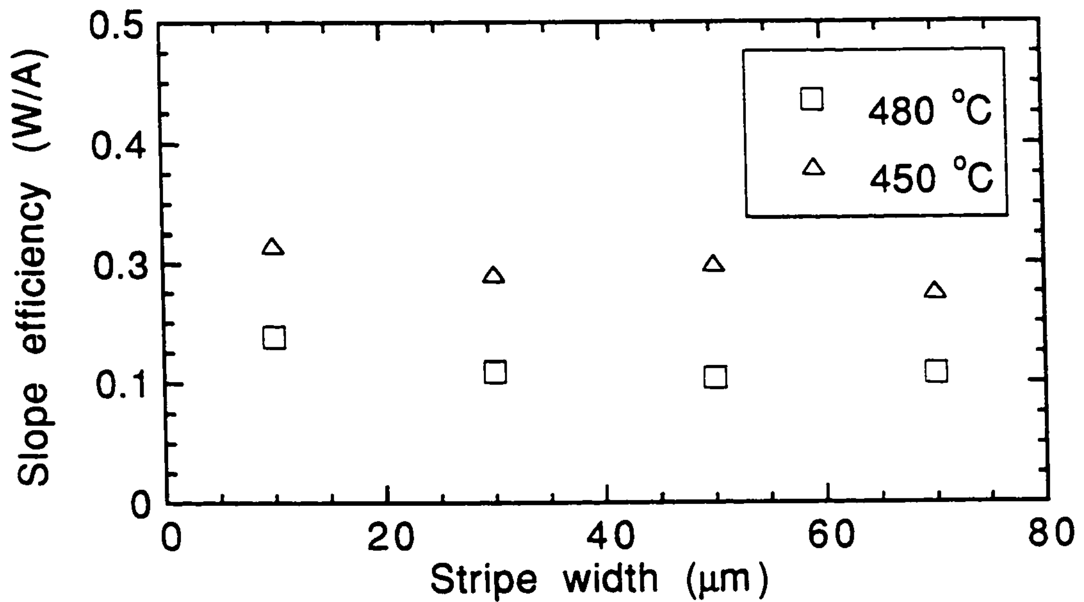

Fig. 4.15. Slope efficiency versus stripe width for DH lasers with an active region having a bandgap wavelength of 1.3 μm grown by conventional epitaxy at 450 and 480 °C.

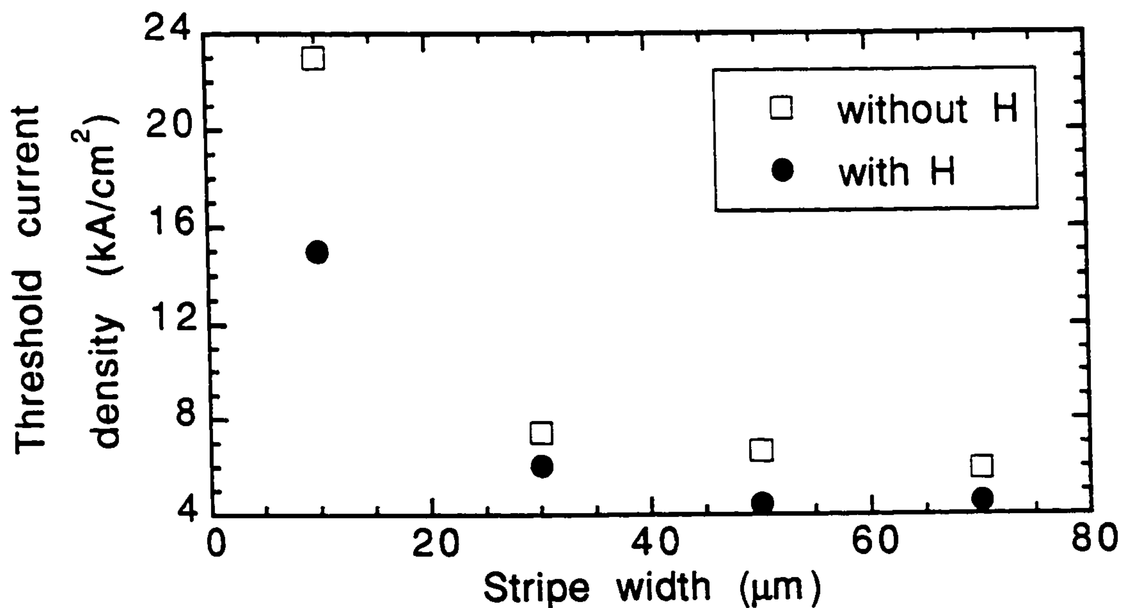

Fig. 4.16. Threshold current density versus stripe width for DH lasers with an active region having bandgap wavelength of 1.3 μm grown at 480 °C by conventional epitaxy and H-assisted epitaxy.

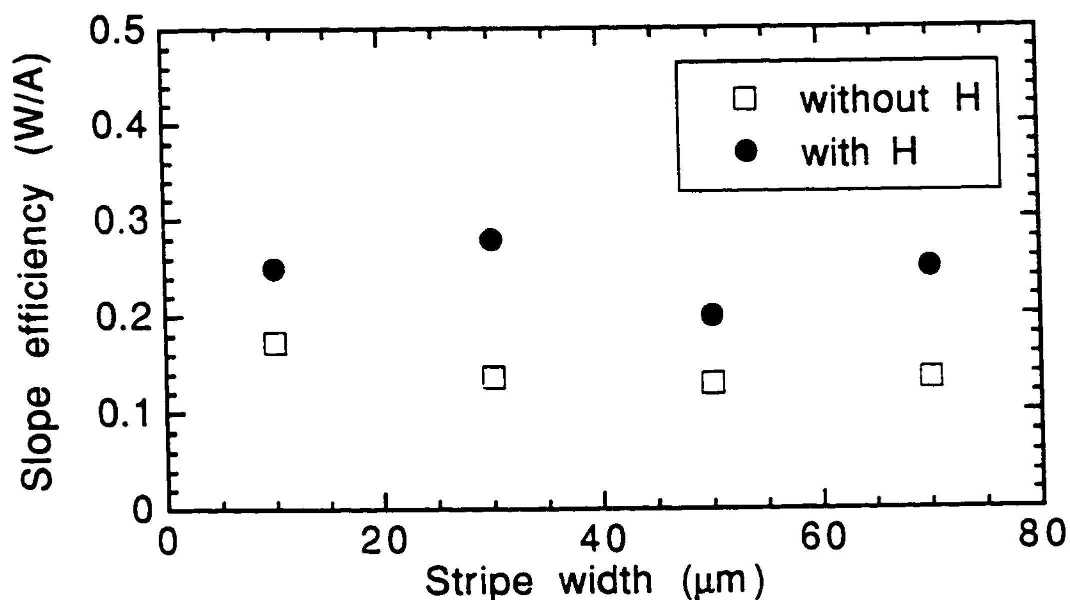

Fig. 4.17. Slope efficiency versus stripe width for DH lasers with an active region having bandgap wavelength of 1.3 µm grown at 480 °C by conventional epitaxy and H-assisted epitaxy.

4.3. Chapter Conclusions

Ar plasma-assisted epitaxy has been shown by TEM, DCXRD and PL to result in less LCM in thick InGaAsP layers and single QWs grown on (100) InP substrates, resulting in improved structural and optical properties as compared to conventional epitaxy without plasma. The reduction in LCM and conformality of growth on substrates containing etched grooves is consistent with a reduced surface adatom diffusion length when growth is carried out with the Ar plasma. Comparison of these results, and RHEED observations, with those obtained using an independent atomic hydrogen source indicates that the reduced LCM is caused by atomic hydrogen present in the Ar plasma stream. The principal species in the Ar plasma (such as the Ar ions) seemed to play a negligible role in the LCM reduction. The plasma simply provides a way of cracking the ambient H_2 inherent in GSMBE via backflow into the ECR chamber. Improvements in DH laser performance by H-assisted epitaxy, attributed to a reduction of LCM, was also established.

CHAPTER 5

Atomic Hydrogen-assisted Epitaxy of InP

This chapter investigates the effects of atomic hydrogen on the electrical and optical properties of InP homoepitaxial layers which are independent of the effects of LCM. H-assisted growths were performed with various H fluxes (0.025 to 0.7 ML/s), H_2 cracker cell temperatures (T_H = 1600 and 1900 °C), PH_3 cracker cell temperatures (T_c = 875 to 1125 °C), annealing conditions and Be doping levels. Room temperature Hall effect measurements were performed using a standard van der Pauw configuration on 2-3 µm thick layers grown at 460 °C on semi-insulating (Fe-doped) (100) InP substrates. Also, the optical properties of the InP layers were studied by photoluminescence (PL).

5.1. Hall Effect Results

Fig. 5.1 shows the Hall mobility versus carrier concentration for undoped InP layers grown by conventional, Ar plasma and H-assisted epitaxy. The PH_3 cracker cell temperature was T_c = 975 °C. Results obtained by varying the PH_3 cracker cell temperature (not shown in Fig. 5.1) are discussed later. The layers were n-type in all cases. The theoretical compensation curves ($\phi = N_a/N_d$) for InP, given by Walukiewicz et al [5.1], are shown as dashed lines. Layers grown by conventional epitaxy (open circles) had Hall mobilities between 3100 and 4300 cm^2/Vs, carrier concentrations between 1 and 4 x 10^{15} cm^{-3}, and typical compensation ratios of about 0.8. *Ex situ* rapid thermal annealing (RTA) at 650 °C for 2 minutes reduced the carrier concentrations to between 0.5 and 1.5 x 10^{15} cm^{-3}, and increased the Hall mobilities to 3900-4800 cm^2/Vs (filled circles).

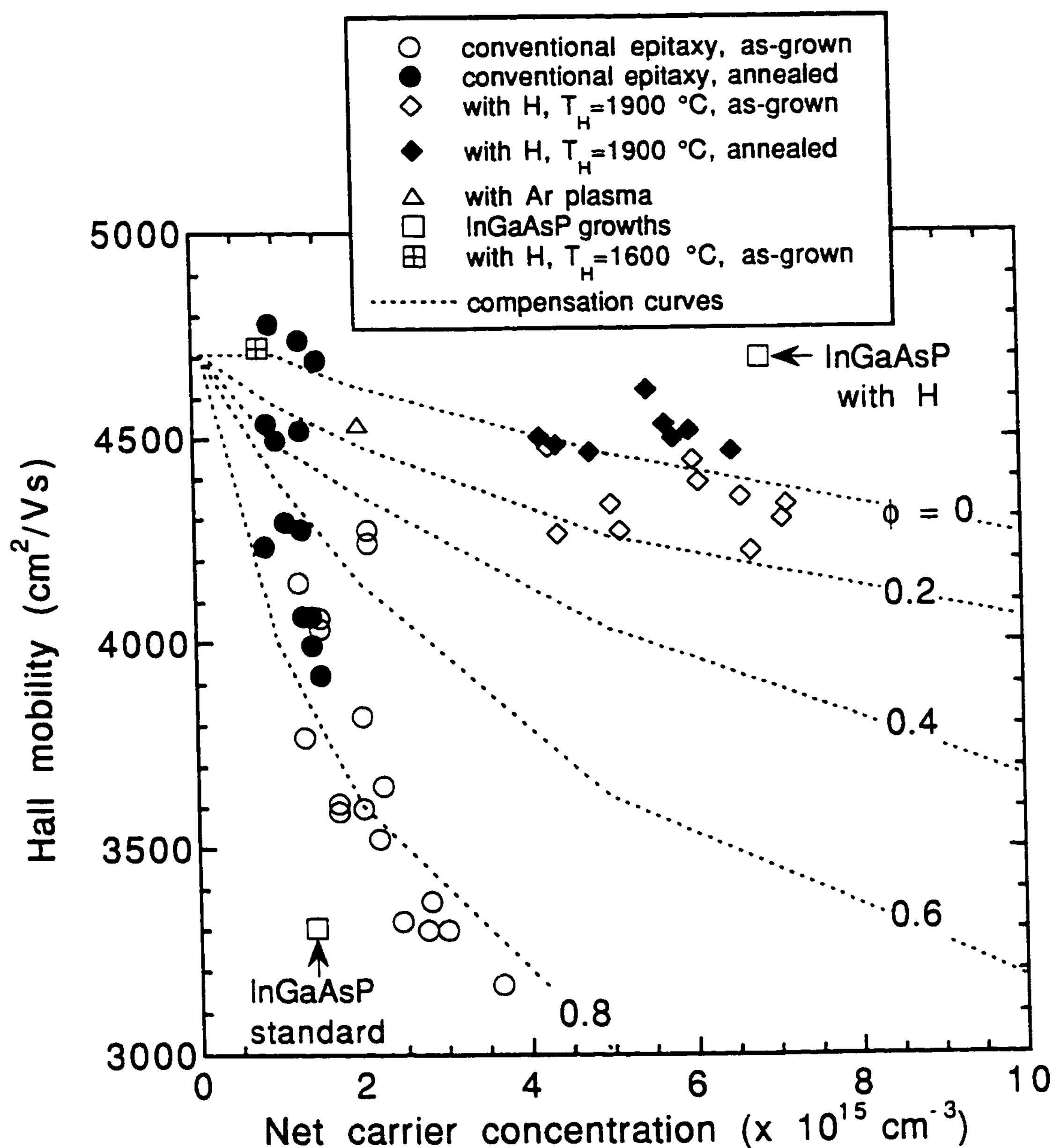

Fig. 5.1. Room temperature Hall effect results for as-grown (open symbols) and annealed (closed symbols) InP homoepitaxial layers grown by conventional epitaxy (circles), and H-assisted epitaxy using T_H = 1600 °C (crossed square) and 1900 °C (diamonds). Hall effect results are also shown for a lattice-matched $In_{0.72}Ga_{0.28}As_{0.61}P_{0.39}$/InP layer grown by H-assisted epitaxy (open squares), and an InP homoepitaxial layer grown by Ar plasma-assisted epitaxy (triangle). The dashed lines indicate theoretical compensation ratios, $\phi = N_a/N_d$.

The compensation curves in Fig. 5.1 allow a determination of the net donor (N_d) and acceptor (N_a) concentrations in the InP growths as shown in Fig. 5.2 [5.1]. The PH_3 cracker cell temperature was T_c = 975 °C unless indicated otherwise. The arrows for T_c = 875, 1050 and 1125 °C refer to single data points. A relationship, where $N_a \approx 0.8\ N_d$, is seen to exist at high values of N_a and N_d. As discussed below, the distribution in donor and acceptor values is attributed to an evolution of the PH_3 cracker cell efficiency due to the installation before these runs of a new rhenium catalyst in the PH_3 cracker. As a result, early growths (shortly after the cracker installation) typically had higher donor and acceptor values, as compared to later growths where the cracker was acting efficiently and the donor and acceptor values were low. Although this time dependence is not presently understood, it probably arises from subtle changes in the cracker surface. The intercept of N_d along the abscissa yields a residual donor concentration between 1-2 x 10^{15} cm^{-3}. This is the concentration obtained in good quality material and represents the background impurity concentration, or defect concentration (possibly related to P antisites [4.1-4.4]).

The effect of the PH_3 cracker efficiency was assessed by varying the PH_3 cracker cell temperature, T_c, from 875 to 1125 °C in three consecutive growths. As shown in Fig. 5.2, both N_a and N_d increased with decreasing cracker cell temperature down to T_c = 875 °C. This suggests that N_a and N_d can be attributed to defects associated with unwanted cracker products which increase with decreasing cracker cell temperature, rather than to impurities due to degassing which would decrease with decreasing T_c. For example, a lower cracking efficiency produces a higher beam flux of tetramers (P_4) relative to dimers (P_2) which has previously been shown to result in a higher concentration of stoichiometric defects (possibly group III and V vacancies) and a greater impurity incorporation [5.2, 5.3]. The trend with T_c in Fig. 5.2 did not depend on the order in which the cracker cell temperature was varied, ruling out any impurity contamination that might have occurred

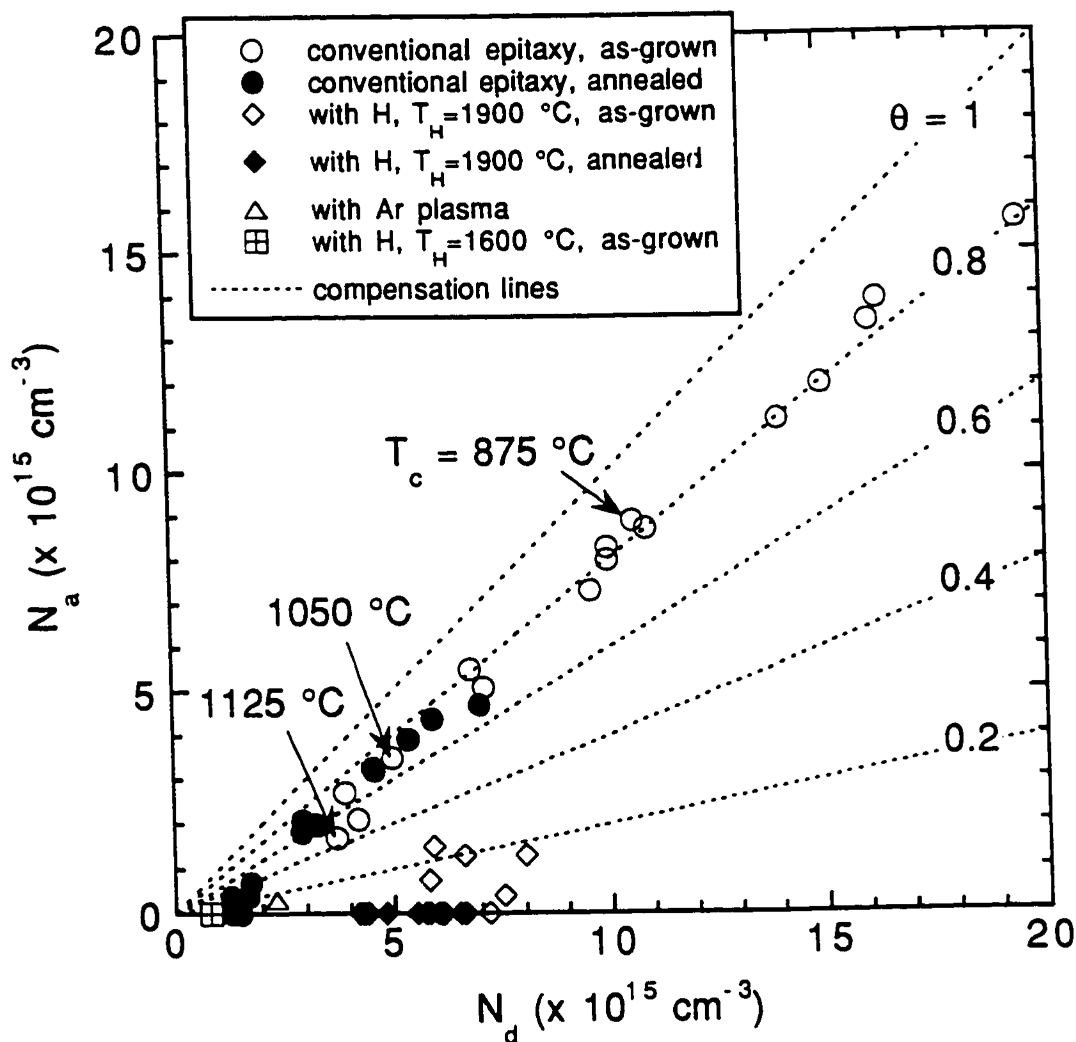

Fig. 5.2. Net donor, N_d, and acceptor concentrations, N_a, for the data in Fig. 5.1. The PH_3 cracker temperature was $T_c = 975$ °C unless indicated otherwise. The arrows for T_c = 875, 1050 and 1125 °C refer to single data points. The dashed lines indicate theoretical compensation ratios, $\phi = N_a/N_d$.

from the earlier growths. Annealing (filled circles) reduced N_a, N_d and ϕ, suggesting that compensating stoichiometric defects are present which are reduced somewhat with annealing. In summary, it appears that for the early growths (after installation of the new catalyst) the P-flux contained a significant fraction of P_4 resulting in a higher concentration of point defects as compared to the later growths where the catalyst was acting efficiently and the P-flux was predominantly P_2.

Fig. 5.1 also shows the Hall effect results for the H-assisted growths, using an H_2 cracker cell temperature of T_H = 1600 °C (crossed square) and 1900 °C (open diamonds). The H_2 flow through the H source was adjusted to give a H flux of about 0.25 ML/s for both T_H settings. A clear 2x1 surface reconstruction, observed by RHEED, indicated a H-terminated surface during growth at 1 μm/hr in both cases. The PH_3 cracker cell temperature was T_c = 975 °C. As discussed below, the time dependence discussed earlier for the conventional growths was not observed for the H-assisted growths.

The InP growth with T_H = 1600 °C (crossed square) produced a Hall mobility of 4725 cm^2/Vs, an n-type carrier concentration of 8 x 10^{14} cm^{-3}, and a compensation ratio between 0 and 0.2. An Ar plasma-assisted growth of InP, in which the H content in the plasma stream is about 0.1 ML/s (as determined in chapter 4), gave similar results (triangle). The growths with T_H = 1900 °C (open diamonds), on the other hand, produced Hall mobilities between 4200 and 4500 cm^2/Vs, n-type carrier concentrations between 4 and 8 x 10^{15} cm^{-3}, and compensation ratios between 0 and 0.2. Finally, Fig. 5.1 shows the results from a 2 μm thick lattice-matched $In_{0.72}Ga_{0.28}As_{0.61}P_{0.39}$/InP layer (open squares) with composition C in Fig. 1.1 grown using a H flux of 0.15 ML/s at T_H = 1900 °C, as used for the TEM studies in chapter 4. The expected Hall mobility for

$In_{0.72}Ga_{0.28}As_{0.61}P_{0.39}$ at n = 10^{15} cm^{-3} is about 5000 cm^2/Vs [2.7]. Hence, the InGaAsP observations are similar to those obtained for InP.

Fig. 5.2 shows that the donor concentrations for the H-assisted growths were between 4 and 8 x 10^{15} cm^{-3} for an H_2 cracker temperature of T_H = 1900 °C (open diamonds), and about 1 x 10^{15} cm^{-3} for T_H = 1600 °C (crossed square). Hence, the donor concentration increased with the H_2 cracker cell temperature with the H flux fixed at 0.25 ML/s. The Ar plasma-assisted growth (triangle), which is a relatively cold source for atomic hydrogen, and the H-assisted growths with T_H = 1600 °C gave comparable electrical characteristics and much lower donor concentrations. This suggests that the higher donor concentrations in the H-assisted growths at T_H = 1900 °C are associated with impurity degassing of the cell or its surrounding area rather than to impurities in the source of the H_2 gas. This was confirmed by the observation that the donor concentration was independent of the H flux from about 10^{-2} to 0.7 ML/s (not shown in Figs. 5.1 or 5.2) as obtained by varying the H_2 flow through the H source at a fixed H_2 cracker cell temperature of T_H = 1900 °C. Hence, the high donor concentration at T_H = 1900 °C cannot be attributed to the H itself. Also, the donor concentration cannot be attributed to the stoichiometric defects discussed earlier because, in contrast to the conventional growths, Figs. 5.1 and 5.2 show that essentially no change was observed in the H-assisted growths upon annealing at either 450 °C for 5 minutes, 650 °C for 2 minutes (filled diamonds), or 700 °C for 1 minute. Hence, while the H-assisted growths appear to reduce point defects, the donor impurity concentration increases with the H source temperature probably due to degassing.

Fig. 5.2 shows that the acceptor concentrations for the H-assisted growths, typically between 0 and 2 x 10^{15} cm^{-3}, were also less as compared to the conventional growths. In order to further assess the effect of hydrogen on the acceptor-type species,

Hall effect measurements were performed on two Be-doped samples (not indicated in Figs. 5.1 or 5.2) with nominal p-type carrier concentrations of 1×10^{16} cm^{-3} and 5×10^{17} cm^{-3}. Although acceptor impurity or defect passivation due to post-growth H irradiation has been observed elsewhere [5.4-5.6], the p-type carrier concentrations in this study were unaffected by a H exposure during growth with 0.25 ML/s at T_H = 1900 °C. In addition, for the undoped samples in Fig. 5.2, the donor concentration in each H growth did not generally equal that for each of the corresponding standard growths which would be expected if simple acceptor passivation were occurring. Finally, acceptor passivation is not expected to be stable under the annealing conditions used in this study [5.4-5.6]. Hence, the atomic hydrogen did not passivate the Be dopant, suggesting that the H is predominantly active only on the surface during growth and does not incorporate into the layers. The observation of the reconstructed 2x1 H-terminated surface during the H-assisted growths, as compared to the conventional 2x4 surface, confirms the presence of H on the sample surface [4.6]. This is consistent with the surfactant action of H as discussed later in chapter 6.

The absence of H within the epilayers was confirmed by secondary ion mass spectroscopy (SIMS) as shown in Fig. 5.3. The sample structure consisted of a 2000 Å thick layer of InP, followed by 2000 Å of InP grown with a deuterium (D) flux of about 0.7 ML/s at T_H = 1900 °C, and capped with 2000 Å of InP. In the as-grown sample, shown in Fig. 5.3(a), some of the D diffused to the substrate/layer interface and appears to have formed complexes with carbon and oxygen contaminants. Subsequent annealing at 700 °C for 1 minute removed the D, as shown in Fig. 5.3(b). Similar results were obtained for an InGaAsP epilayer. Because the D concentration after annealing is below the SIMS detection limit of about 10^{15} cm^{-3}, the reduced acceptor concentration associated with the H-assisted growths in Fig. 5.2 cannot be attributed to simple acceptor passivation.

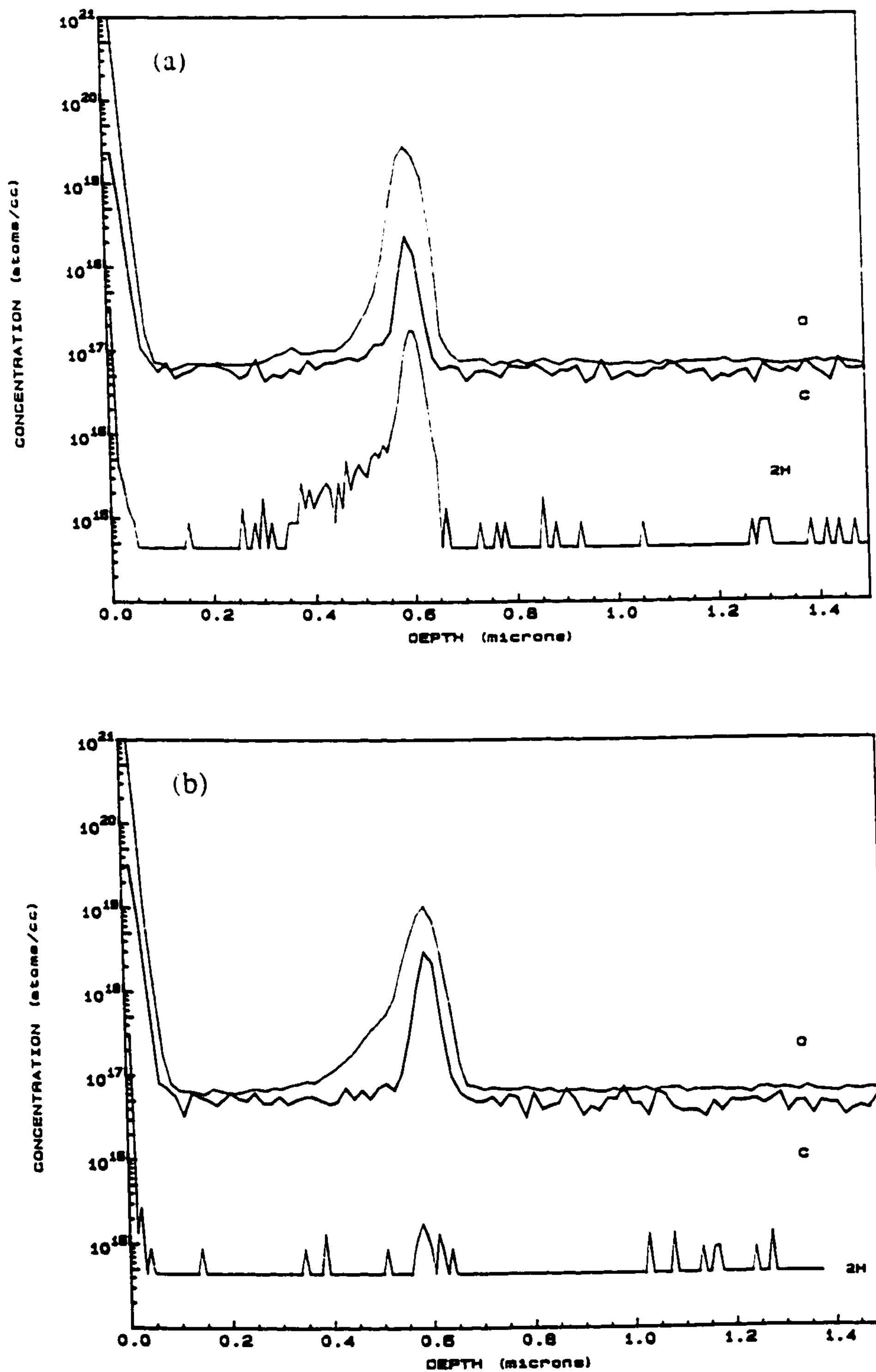

Fig. 5.3. SIMS yield as a function of depth from the surface for (a) an as-grown InP structure grown with deuterium, as discussed in the text, and (b) the same sample after annealing at 700 °C for 1 minute.

The reduction in donor and acceptor defects with H exposure, and the absence of the time dependence discussed earlier for the conventional growths, may be due to a reaction between H and P_4 on the sample surface during growth. P_4 may be decomposed and/or desorbed via the formation of PH_x species (x = 1, 2, 3), resulting in fewer stoichiometric defects as described earlier for the conventional growths. Evidence to support this view was provided by standard double crystal X-ray diffraction measurements which indicated a shift of 200 arcseconds toward compression in the relative Bragg angle for the InGaAsP layer grown with H as compared to the conventional growth. This result, when combined with PL bandgap determinations, indicated that while the group III composition was unaffected, the desorption of about 4% P (which could include P_4) occurred in the H-assisted growths. The increased P desorption, however, did not produce a greater P vacancy concentration. Indeed, photoluminescence measurements, discussed below, indicate a reduced phosphorus vacancy concentration in the presence of H probably due to the P_4 reduction.

The change in surface reconstruction due to the presence of H may also play a role in the defect reduction. The 2x1 H-terminated surface contains no phosphorus dimer vacancies, as compared to the conventional 2x4 surface, as shown in Fig. 4.11. During conventional epitaxy, the missing dimer row is filled by a difficult rate limiting reaction, as discussed later in chapter 6, which may produce grown-in P vacancies. The 2x1 H-terminated surface, on the other hand, is expected to produce fewer P vacancies due to the absence of the missing dimer row. This is consistent with photoluminescence measurements discussed in the following section in which a lower intensity of the P vacancy-related peak is observed with H exposure.

5.2. Photoluminescence

Fig. 5.4 shows the low temperature (15 K) PL spectra for a conventional growth without H (thin solid line), and H-assisted growths with T_H = 1900 °C (dashed line) and

T_H = 1600 °C (thick solid line). The H_2 flow was adjusted to give a H flux of 0.25 ML/s for both T_H settings. All three growths had a PH_3 cracker cell temperature of T_c = 1050 °C. The relative PL intensity of peak 2 is multiplied by a factor of 10 in all cases, while the peaks below 1.37 eV are all multiplied by 50.

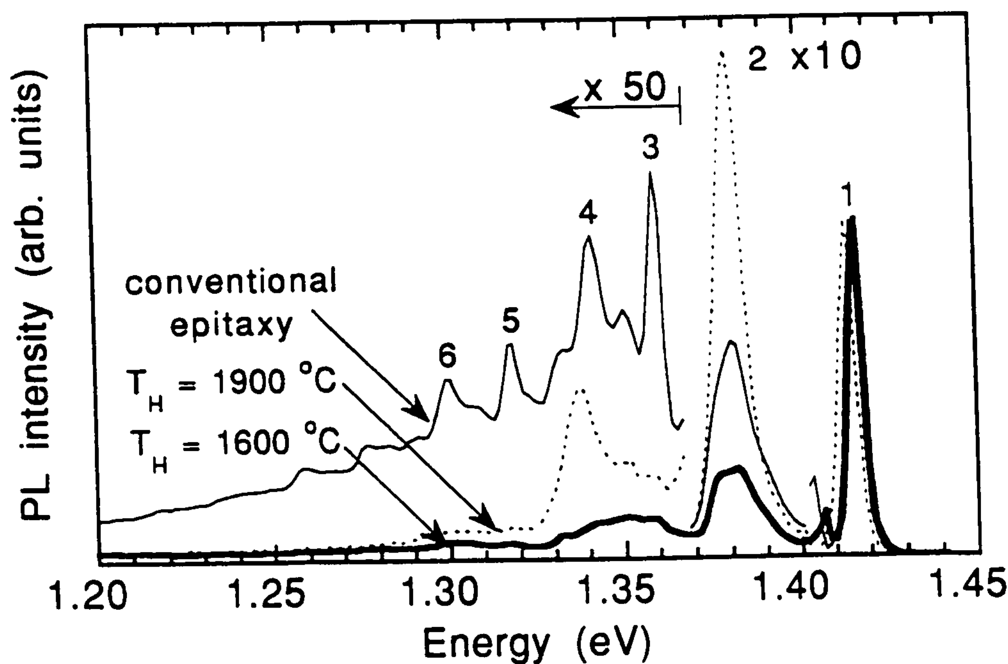

Fig. 5.4. Low temperature (15 K) PL spectra from InP homoepitaxial layers grown by conventional epitaxy (thin solid line), and H-assisted epitaxy using T_H = 1600 °C (thick solid line) and 1900 °C (dashed line). The peaks labelled 1 to 6 are discussed in the text.

The band-edge exciton PL (peak 1), also shown in Fig. 5.5 for layers grown with different PH_3 cracker cell temperatures, consists of several unresolved peaks associated with recombination of electron-hole pairs (e-h) at 1.4215 eV, free excitons (X) at 1.4180 eV, donor bound excitons (DX) at 1.4168 eV, and acceptor bound excitons (AX) at 1.4147 eV [2.7, 5.7-5.9]. As shown in Fig. 5.5, the donor bound exciton peak (DX) at 1.4168

eV increases only slightly with PH_3 cracker cell temperature (T_c = 875 to 1125 °C) in the conventional growths (thin solid lines), while the H growth with T_H = 1900 °C clearly shows the highest DX peak intensity (dashed line).

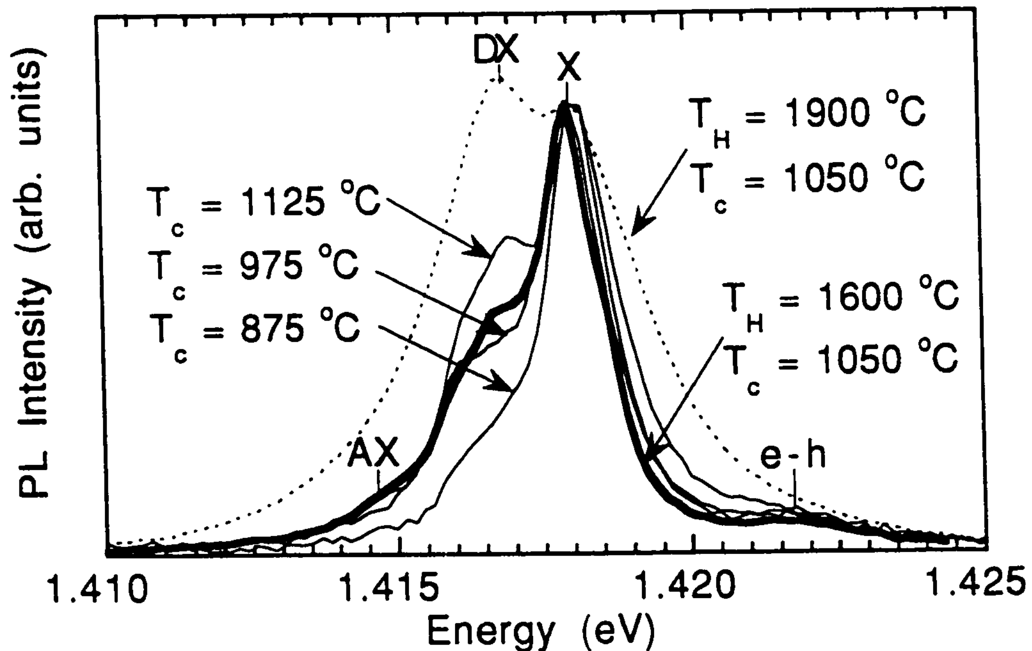

Fig. 5.5. Band-edge exciton PL obtained with various PH_3 cracker cell temperatures, T_c, and H cracker cell temperatures, T_H. Results are shown for conventional growths (thin solid lines), and H-assisted growths using T_H = 1600 °C (thick solid line) and 1900 °C (dashed line).

The unresolved donor-to-acceptor (D-A) and band-to-acceptor (e-A) transitions at 1.38 eV (peak 2 in Fig. 5.4) and the corresponding unresolved phonon replicas (first order at peak 4 and second order at peak 6) were also more intense at T_H = 1900 °C as compared to 1600 °C. Annealing and the magnitude of the H flux had no effect on these impurity-related peaks which is consistent with the previous Hall effect results where the donor

origin was identified as impurity degassing of the H_2 cracker. The donor ionization energy is about 10 meV, while the acceptor ionization energy is about 30 meV. However, sufficient spectral resolution for identification of the impurity species has not been achieved.

The peak at 1.36 eV (peak 3) is due to recombination of donor-bound excitons related to deep-lying phosphorus vacancy (V_P) centres [5.10-5.12]. This peak and its phonon replica (peak 5) are much weaker in the H-assisted growths, indicating a lower V_P concentration. As discussed above, this is attributed to a reduced surface P_4 concentration and to the absence of the missing phosphorus dimer row due to the presence of H. The vacancy concentrations were below the detection limit of positron annihilation.

PL spectra from the Ar plasma-assisted growths of InP were similar to the H-assisted growth at T_H = 1600 °C or to the best growths by conventional epitaxy, provided a substrate bias of +40 V was used to reduce the energy of the incident ion component of the plasma [2.3]. This is similar to the Hall effect results discussed earlier. The Ar plasma, which is a relatively cold source of H, appears to avoid the contamination problems associated with the use of a hot H_2 cracker filament.

5.3. Chapter Conclusions

Hall effect and photoluminescence studies on InP homoepitaxial layers suggested that the P flux of early growths (after installation of a new catalyst) contained a significant fraction of unwanted cracker products, such as P_4, resulting in a higher concentration of point defects, as compared to later growths where the catalyst was acting efficiently and the P flux was predominantly P_2. H-assisted epitaxy therefore appeared to have the most benefit when the MBE system was not operating at optimum performance. The defect reduction was attributed to reactions between H and the unwanted species (probably P_4) on the sample surface during growth, and by the absence of the missing dimer row present

during conventional epitaxy. The donor impurity concentration increased with thermal source temperature probably due to degassing. Ar plasma-assisted epitaxy, on the other hand, was shown to provide an adequate flux of H (to reduce the LCM in InGaAsP, for example) while eliminating the degassing problems associated with the thermal cracker.

CHAPTER 6

Growth Mechanisms of III-V Compounds during Conventional and Atomic Hydrogen-assisted Epitaxy

This chapter investigates the incorporation of the group III and V components in $In_{1-x}Ga_xAs_yP_{1-y}$ layers and its implications for lateral composition modulation (LCM). Section 6.1 describes a simple incorporation model, based on incorporation coefficients and bulk thermodynamic parameters, which successfully predicts the occurrence of LCM within the miscibility gap. These models, however, do not take account of the actual surface-mediated reactions that occur during epitaxy. The effect of growth conditions or surface reconstruction are therefore excluded. Section 6.2 describes a simple surface model of epitaxial growth which explains the effects of atomic hydrogen on the LCM.

6.1. Incorporation Models of Epitaxy and Implications for LCM

Control of the group III composition during growth by molecular beam epitaxy (MBE) is trivial since there is negligible re-evaporation of the group III elements at typical growth rates and temperatures. Hence, the incorporation probabilities of Ga and In are equal to unity, the growth rate is determined directly by the incident flux of the group III elements, and the Ga/In ratio in the solid is the same as in the beam flux. The incorporation of As and P, however, is complicated by the difference in incorporation probabilities of the group V species on the InGaAsP surface and by the group V overpressure required to stabilize the surface at growth temperatures greater than the congruent sublimation temperature.

In gas source molecular beam epitaxy (GSMBE), the group V species are supplied primarily in the form of As_2 and P_2 from the cracking of arsine (AsH_3) and phosphine

(PH_3) in a high temperature (≈ 1000 °C) cell. Early attempts at a quantitative incorporation model related the group V solid composition to these dimer fluxes via "sticking" probabilities or incorporation coefficients [6.1]. A thermodynamic model based on bulk properties and assuming chemical equilibrium at the InGaAsP surface has also been developed [6.2-6.4]. These models are reasonably accurate in predicting the group V solid composition for a given beam flux composition. However, these models will also be shown to predict the occurrence of LCM within the miscibility gap due to the preferential incorporation of P_2 at Ga sites and of As_2 at In sites.

Epitaxial layers of $In_{1-x}Ga_xAs_yP_{1-y}$ were grown nominally lattice-matched to (100) n-type InP substrates. The sample structure consisted of a 3000 Å thick InGaAsP layer grown on a 500 Å InP buffer layer, followed by a 250 Å InP cap layer. All layers were grown at a temperature of 460 °C. The group V incorporation was studied for various V/III flux ratios by using total hydride flows of 2.8, 3.5, 5.0, and 8.0 sccm, keeping the growth rate constant at 1 µm/hr. A total hydride flow of 5.0 sccm and a growth rate of 0.625 µm/hr was also used to verify the equivalence of the V/III flux ratio to that at 8.0 sccm and 1 µm/hr. The InGaAsP compositions (not shown in Fig. 1.1) for a given V/III flux ratio were controlled by varying the arsine flow fraction, Y, and the group III fluxes, keeping the total hydride flow and growth rate constant. The InGaAsP compositions were established by combining lattice mismatch determinations from DCXRD with PL bandgap determinations as described in chapter 2.

Incorporation data for the $In_{1-x}Ga_xAs_yP_{1-y}$ layers (y vs. Y) is shown in Fig. 6.1 for various V/III flux ratios, $k = \phi_V/\phi_{III}$. Note that the results at 8.0 sccm and 1 µm/hr are essentially equivalent to those at 5.0 sccm and 0.625 µm/hr. This observation is compatible with the assertion that the V/III beam flux ratio is the relevant parameter determining the incorporation and not simply the total group V flux. The dashed lines in

Fig. 6.1 are the incorporation curves based on the thermodynamic model discussed below.

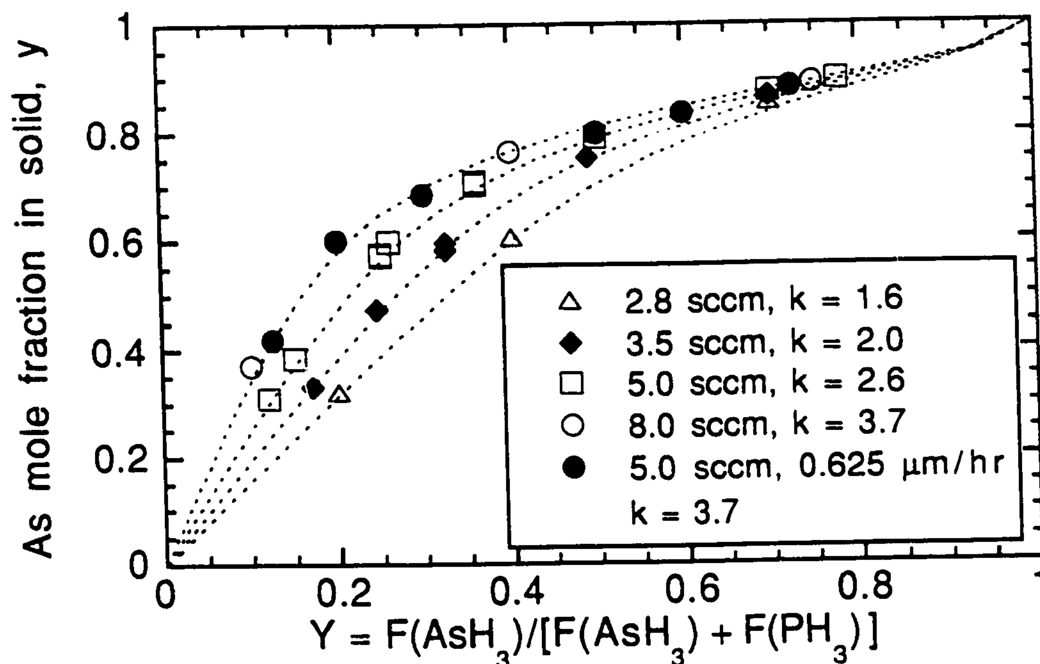

Fig. 6.1. Incorporation data showing As solid content, y, versus arsine flow fraction, Y. The V/III beam flux ratio is k and the growth rate is 1 μm/hr unless stated otherwise. The dashed lines are fits from the thermodynamic model as described in the text.

6.1.1 Incorporation Coefficient Model

Early attempts at a quantitative incorporation model [6.1] related the group V solid composition to the dimer fluxes via incorporation probabilities, c_{As2} and c_{P2}:

$$\frac{y}{1-y} = \frac{c_{As_2}\Phi_{As_2}}{c_{P_2}\Phi_{P_2}} \tag{6.1}$$

or, equivalently, using the arsine flow fraction, Y:

$$\frac{y}{1-y} = c_0 \frac{Y}{1-Y} \tag{6.2}$$

where the incorporation coefficient, $c_0 = c_{As2}/c_{P2}$, is usually assumed to be a constant as a first approximation. The upward bowing of the data in Fig. 6.1 can therefore be interpreted in terms of the preferential incorporation of As as compared to P on the InGaAsP surface, that is, $c_0 > 1$, as observed by many authors [6.1-6.4].

Although a reasonable fit to experimental data under restricted conditions can be obtained with Eq. (6.2), in this work it has been found that the incorporation coefficient is not constant but varies with the V/III flux ratio, k, and the arsine flow fraction, Y. It is convenient, therefore, to treat the incorporation coefficient as a variable quantity, c, defined in terms of y and Y, giving:

$$c = \frac{y}{1-y} \frac{1-Y}{Y} \tag{6.3}$$

which is just a rearrangement of Eq. (6.2). Experimental values of the incorporation coefficient can then be derived from the experimental values for y and Y via Eq. (6.3). Thus, the data of Fig. 6.1 is plotted in Fig. 6.2 as the incorporation coefficient, c, versus the arsine flow fraction, Y. A representative error bar is indicated in Fig. 6.2.

The incorporation coefficients in Fig. 6.2 deviate significantly from the simple incorporation coefficient model which uses a constant value for c, since there is a clear dependence of c on k (c increases as k increases) as well as a dependence of c on Y for a given k. The gradual decrease in c as Y decreases (for low values of Y) has previously been explained in terms of an As underpressure condition [6.2]. Briefly, the As incorporation probability approaches unity when the amount of As in the beam flux becomes insufficient to satisfy the required As content in the solid at the given growth rate. This occurs at low arsine flow fractions and leads to the decline in c with decreasing Y.

At higher arsine flow fractions, the incorporation probability of P increases with

respect to that of As, also leading to a decline in c. This has been interpreted elsewhere [6.5] in terms of a preferential "sticking" of P to Ga sites and of As to In sites within the miscibility gap as the Ga mole fraction in the solid increases monotonically with the arsine flow fraction as required to maintain a lattice-match with the InP substrate. The decline in c is seen to be consistent with the regions of immiscibility shown in Fig. 1.1 and indicated by the arrows in Fig. 6.2.

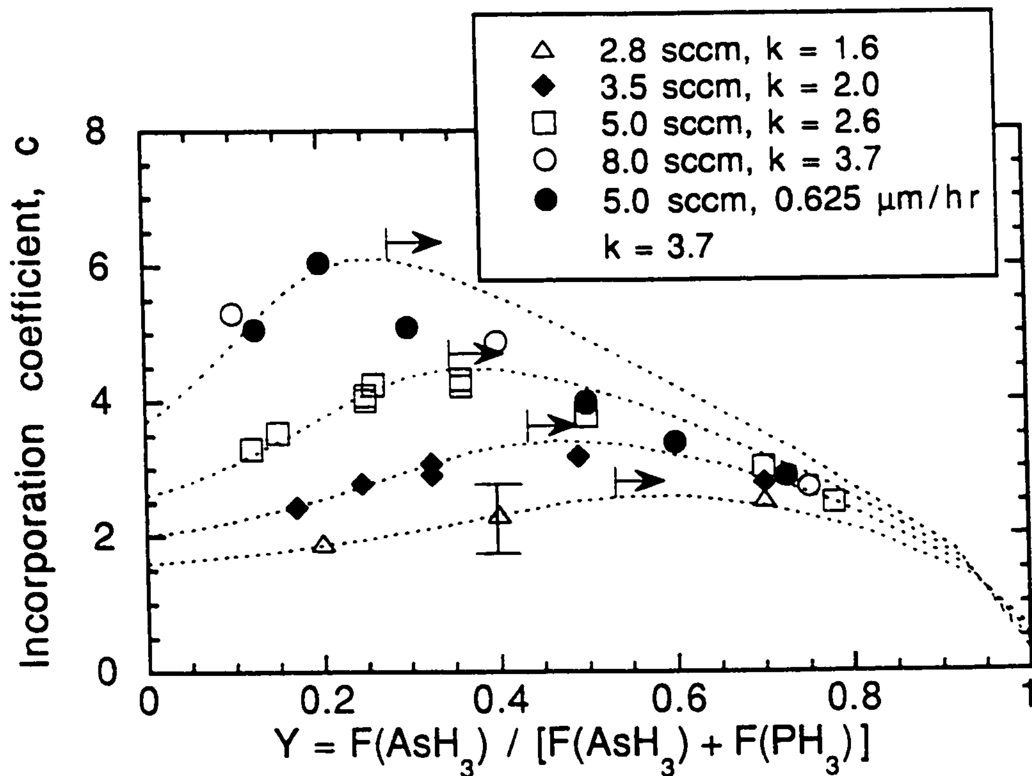

Fig. 6.2. Incorporation coefficient data fitted with the thermodynamic model (dashed curves). The arrows indicate the regions of immiscibility as discussed in the text.

Despite the successes of this simple model, the incorporation coefficient remains essentially a fitting parameter with little physical insight into its Y- or k-dependence at the greater arsine flow fractions. A thermodynamic model based on bulk properties and assuming chemical equilibrium at the InGaAsP surface, is therefore developed in the following section.

6.1.2. Thermodynamic Model

The dependence of c on k suggests that the excess of group V flux plays an important role in the group V incorporation. The total As_2 flux , Φ_{As2}, can be written in terms of the incorporated flux, Φ^{i}_{As2}, and the excess flux, Φ^{e}_{As2}, as $\Phi_{As2} = \Phi^{i}_{As2} + \Phi^{e}_{As2}$. The incorporated As mole fraction is then:

$$y = \frac{2\left(\Phi_{As_2} - \Phi^{e}_{As_2}\right)}{\Phi_{III}} \tag{6.4}$$

or, using the arsine flow fraction, Y:

$$y = k\left(Y - \frac{2\Phi^{e}_{As_2}}{\Phi_V}\right) \tag{6.5}$$

Similarly, the phosphorus content in the solid is given by

$$1 - y = k\left[(1 - Y) - \frac{2\Phi^{e}_{P_2}}{\Phi_V}\right] \tag{6.6}$$

Rearranging Eqs. (6.5) and (6.6) and forming ratios gives:

$$\frac{\Phi^{e}_{P_2}}{\Phi^{e}_{As_2}} = \frac{(1 - Y) - (1 - y)/k}{Y - (y/k)} \tag{6.7}$$

The InGaAsP quaternary may be considered as being formed from the binary reactions:

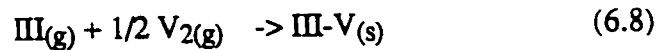

$$III_{(g)} + 1/2\, V_{2(g)} \;\rightarrow\; III\text{-}V_{(s)} \tag{6.8}$$

The equilibrium constants for these reactions are:

$$K_{III\text{-}V} = \frac{a_{III\text{-}V}}{P_{III}\sqrt{P_{V_2}}} \quad (6.9)$$

where the a_i's are the activities of the binary species. The P_i's are the partial pressures which, for epitaxial growth, are identified with the excess fluxes, that is, the incident flux of each species minus the incorporated flux required for growth. The activities, a_i, are expressed in terms of the activity coefficients, γ_i, and the binary mole fractions, X_i, in the quaternary :

$$a_i = X_i \gamma_i \quad (6.10)$$

where, for example, $X_{InP} = (1 - x)(1 - y)$. Using the Langmuir equation to relate pressures to fluxes, and using Eqs. (6.9) and (6.10), gives [6.2]:

$$\frac{\Phi^e_{P_2}}{\Phi^e_{As_2}} = \beta \left(\frac{1 - y}{y}\right)^2 \quad (6.11)$$

where

$$\beta = \sqrt{\frac{m_{As_2}}{m_{P_2}}} \left(\frac{\gamma_{GaP} K_{GaAs}}{\gamma_{GaAs} K_{GaP}}\right)^2 = \sqrt{\frac{m_{As_2}}{m_{P_2}}} \left(\frac{\gamma_{InP} K_{InAs}}{\gamma_{InAs} K_{InP}}\right)^2 \quad (6.12)$$

Combining Eqs. (6.7) and (6.11) and rearranging yields:

$$Y = \frac{k - (1 - y) + \beta y \left(\frac{1 - y}{y}\right)^2}{k + \beta k \left(\frac{1 - y}{y}\right)^2} \quad (6.13)$$

The activity coefficients and equilibrium constants in β may be calculated from the

delta lattice parameter (DLP) model proposed by Stringfellow [1.9]. However, typical values for β are not given in the literature, and the exact value is sensitive to the exponential terms in the expressions and the uncertainty in the thermodynamic parameters. We have found that $\beta = 30$ gives the best fit to our experimental data at a growth temperature of 460 °C, as indicated by the dashed lines in Figs. 6.1 and 6.2, which is reasonably close to the value of $\beta = 57$ estimated from the DLP model and available thermodynamic data. The dashed lines in Fig. 6.2 were obtained by inserting Eq. (6.13) into Eq. (6.3).

Although a reasonable fit to the experimental data is obtained with a constant value of $\beta = 30$, β has previously been shown to depend on the substrate surface orientation [6.2]. In addition, the spinodal isotherm in Fig. 1.1, calculated using the same thermodynamic principles as used for the incorporation curves, cannot predict the kinetic limitations imposed by the growth conditions on the LCM [1.22, 1.23]. In particular, these models cannot explain the reduction in LCM obtained with H exposure. Indeed, all models describing incorporation or LCM make little or no reference to the bonding configurations of the underlying surface. These models, typified by Eq. (6.8), implicitly assume that the crystal grows by the simultaneous formation of all the tetrahedral bonds in the bulk and are therefore inadequate for describing the actual surface-mediated processes that occur during epitaxy. Any attempt to understand epilayer growth from thermodynamic considerations, using bulk parameters, are unlikely to provide the detailed atomistic understanding that is required to describe the effect of growth conditions and surface reconstruction on the LCM.

6.2. Surface-mediated Model of Epitaxy

As mentioned in chapters 1 and 4, growth in the presence of H has been shown to produce less three-dimensional (3D) island growth and fewer dislocations in strained layer epitaxy [1.26-1.31], and to enhance the step flow growth on vicinal substrates [1.32-

1.35]. Two contradictory models, involving enhanced or suppressed adatom migration, have been proposed to explain these observations.

If the adatom migration is increased, as in migration-enhanced epitaxy, then the adatoms can migrate over longer distances thereby enhancing the step flow growth. Earlier studies have therefore proposed several mechanisms whereby the adatom migration is enhanced, such as site-blocking effects [6.6] or hydride formation [1.33-1.35, 6.6, 6.7], in order to account for the improved layer-by-layer growth in the presence of H. Other models have proposed that H may act as a "surface-active" species (that is, a surfactant) in which H adsorption lowers the surface energy of the growing layer [1.29-1.31]. Indeed, theoretical calculations have shown that the H-terminated 2x1 reconstructed GaAs surface has a lower energy compared to the conventional 2x4 surface [4.6]. For strained layer epitaxy, planar growth of the first monolayer (wetting) in the case of so-called Volmer-Weber growth (where the surface energy of the epilayer is higher than that of the substrate) may then be achieved by decreasing the surface energy of the epilayer. On the other hand, in the case of Stranski-Krastanow growth (where island growth succeeds an initial period of planar growth) the net driving force for 3D island formation (to reduce strain energy) would be expected to increase on a H-exposed surface because the surface energy cost associated with island formation would be reduced [1.30, 6.8].

The above considerations reveal that if the only role of H were to decrease surface energy then 3D island formation would increase in direct contradiction with the experimental results. Since islanding is thermodynamically favored, reduction of the adatom migration seems to be the relevant physical effect responsible for the reduced islanding, not the surface energy reduction *per se* nor an enhanced adatom migration as suggested previously. Further evidence to support this view was given in chapter 4 by the observation of reduced lateral composition modulation (LCM) for InGaAsP layers grown in the presence of H.

A random arrangement of atoms is initially deposited on the surface during epitaxial growth such that an ideal InGaAsP alloy would have the group III atoms (In and Ga) and

the group V atoms (As and P) distributed randomly on their respective sublattices of the zincblende structure. However, thermodynamic models show that a driving force for phase separation exists due to the positive enthalpy of mixing associated with the bending and stretching of the binary bonds from their equilibrium values [1.10-1.11]. This means that the microscopic strain energy of any alloy within the miscibility gap can be reduced during growth by separating into InAs-rich and GaP-rich regions resulting in LCM. The LCM can be minimized, however, if the random arrangement of adatoms deposited on the surface is covered by the next layer before significant diffusion can occur. In this section, the reduction in LCM on H-exposed surfaces will therefore be explained in terms of a decrease in the surface diffusion length of adatoms which is consistent with the above discussion.

Previous models of the mechanism by which a surfactant, such as atomic hydrogen, would reduce adatom migration have suggested that an enhanced driving force may exist for adatom incorporation in order to allow the surfactant atoms to occupy the surface sites where they have lower energy [1.33]. Hence, atomic H may limit the surface diffusion length of adatoms by essentially increasing their incorporation rate into the growing layer. The observation of enhanced step flow growth on H-exposed vicinal surfaces may then be understood from this model in terms of an enhanced "sticking" probability of adatoms to atomic steps in the presence of H. However, a great deal of uncertainty in the exact mechanism of surfactant action remains. In this chapter a detailed atomistic model, including surface reconstruction effects based on reflection high energy electron diffraction observations, is developed to further elucidate the surfactant action of H on (100) III-V surfaces. A simple rate equation model is then used to understand the decrease in the surface diffusion length of adatoms due to these H-related growth processes.

A growth sequence without atomic hydrogen exposure [6.9-6.11] is shown schematically (top view) in Figs. 6.3(a), (b) and (c) while the surface models involving H are indicated in Figs. 6.3(d) and (e). These sequences show only the first few steps of the

bilayer growth model which reveal the essential differences between growth with and without hydrogen. We assume, as in GSMBE, that the beam flux consists of group III atoms and group V dimers.

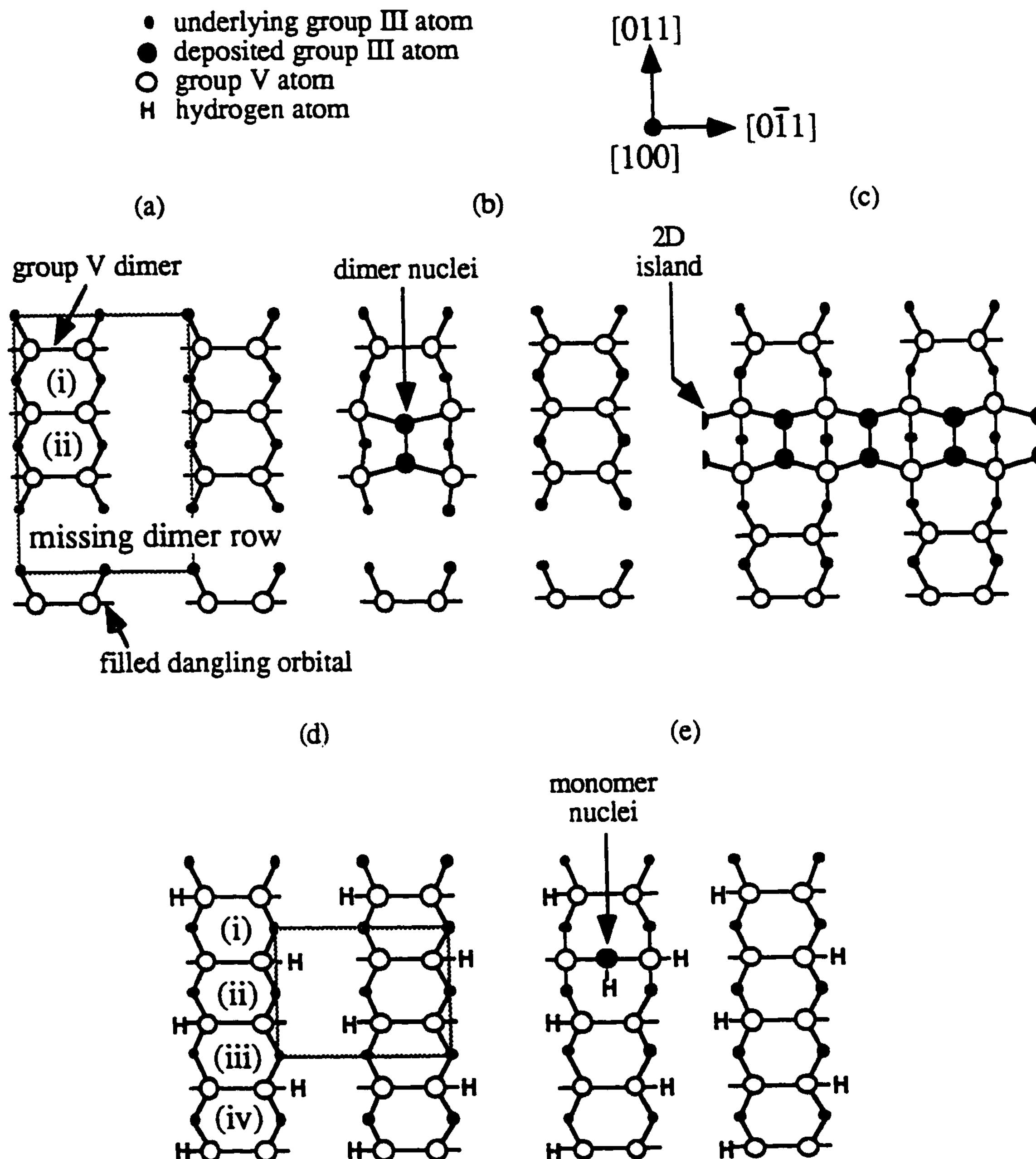

Fig. 6.3. Surface models for electronically stable intermediate structures for a (100) III-V surface grown by ((a) to (c)) conventional epitaxy, and ((d), (e)) H-assisted epitaxy.

6.2.1. Conventional Epitaxy

In the case of conventional epitaxy without H, the growth cycle begins with a group V stabilized surface which has a 2x4 reconstruction as shown in Fig. 6.3(a). The 2x4 surface unit cell, indicated by the box, consists of three group V dimers and one dimer vacancy. The dimer bonds pull the group V atoms together to an interatomic distance that is shorter than the bulk separation distance. Each group V atom on the surface has a filled dangling orbital (lone pair of electrons), while each dimer vacancy exposes four group III atoms in the underlying layer which each have an empty dangling orbital [6.9-6.11].

The growth model for conventional epitaxy without H has been described elsewhere [6.9-6.11] and is reviewed only briefly here. The model assumes that growth proceeds via the most stable atomic configurations that satisfy the electron counting model [6.12]. The electron counting model states that the lowest energy configurations are those with filled dangling orbitals on the group V atoms and empty dangling orbitals on the group III atoms due to the energy levels of these dangling orbital states relative to the Fermi level. Hence, the lifetime of an adatom before chemisorption, and therefore the adatom diffusion length, depends significantly on the local surface bonding configurations.

The chemisorption of a single group III adatom at a group V dimer site, for example, is expected to be unstable because this process results in non-bonding electrons above the Fermi level (that is, the electron counting model is not satisfied). This configuration is energetically unfavorable and will "decay" unless stabilized within a few vibrational cycles. These considerations suggest that the adatom incorporation occurs via dimer formation, as depicted in Fig. 6.3(b), such that the electron counting model is satisfied. Additional restrictions exist for adatom incorporation at the dangling orbital sites. In this case, four non-bonding electrons per group III dimer are produced due to the lone pair of electrons in the dangling orbital of each group V surface site. At the same time, four back-bonding electrons are unavailable from the underlying group III atoms for the chemisorption of a group V dimer along the missing dimer row. Hence, a plausible

incorporation pathway involves the chemisorption of two group III atoms across the dangling orbital sites (forming a group III dimer) and the "simultaneous" chemisorption of a group V dimer along the missing dimer row such that the electron counting model is satisfied. Hence, both group III atoms and group V dimers are expected to migrate over long distances in the physisorbed state until this rate limiting step occurs.

The re-evaporation of group III adatoms is negligible under the growth conditions used in this work. Hence, each group III adatom from the incident flux, F, migrates on the surface within the diffusion area, D, per unit time and collides with DM other adatoms within this time where D is the surface diffusion constant and M is the group III adatom density. Growth can occur either by 2D nucleation on the smooth surface (that is, an island-free region of the surface) or by the accretion of adatoms along the atomic steps of nuclei or 2D islands. The rate equation for the adatom density is therefore given by:

$$\begin{aligned} dM/dt &= F - DM^2M_{dv}/m - DM^2N_{dv}/n \\ &= F - M/\tau \end{aligned} \qquad (6.8)$$

where M_{dv}/m is the total probability per collision of dimer nucleation on the smooth surface and N_{dv}/n is the total probability per collision of dimer formation near the edges of nuclei or 2D islands. The density of group III dimer vacancy sites on the smooth surface is M_{dv} such that $1/m$ is the probability of dimer nucleation per unit density of available nucleation sites. Similarly, N_{dv} is the density of dimer vacancy sites along the periphery of nuclei or 2D islands such that $1/n$ is the probability of dimer formation per unit density of available step sites. Eq. (6.8) differs from previous rate equations [6.13] which assumed the incorporation of single adatoms at the step sites in violation of the electron counting model and previous STM observations [6.14, 6.15]. The total incorporation rate is usually expressed in terms of a lifetime, τ, as indicated in Eq. (6.8). In principle, incorporation of the group V species could be modelled by similar rate equations with the inclusion of a

desorption term as discussed earlier [6.2].

The effect of the surface diffusion length on the LCM can be understood by considering site specific incorporation probabilities such that In adatoms and As dimers "stick" preferentially to InAs-rich regions, while Ga adatoms and P dimers "stick" preferentially to GaP-rich regions, as suggested elsewhere [6.5]. This process is expected to yield the columnar microstructure discussed earlier for the TEM observations. Since the number of site visits is large for each adatom (10^4 for typical growth conditions), the difference between the probability of group III dimer formation at InAs-rich and GaP-rich regions need only be on the order of 10^{-6} in order to obtain typical compositional excursions of 1% as observed in Fig. 3.7 [1.22, 1.23]. This difference of 10^{-6} is small compared to previous estimates of $M_{dv}/m \sim 10^{-4}$ for Ga on a GaAs surface [6.13]. Hence, the incorporation probabilities in Eq. (6.8) are taken to be a constant, independent of the type of adatom or the binding site. For the purposes of this study, the reduction in LCM with decreasing surface diffusion length is simply understood in terms of a reduction in the number of site visits by an adatom or, equivalently, a smaller surface diffusion area. Accordingly, the adatom surface diffusion length need not be reduced below the lateral scale of the composition modulation in order to reduce the compositional fluctuations. As shown below, the lateral dimensions of the LCM are determined by the relative magnitudes of n and m which are independent of the surface diffusion length.

In the initial stage of the bilayer growth cycle, the nucleation rate is much greater than the incorporation rate near the nuclei or 2D island edges and the coverage-dependence of M_{dv} may be ignored. Eq. (6.8) may be solved under these conditions (with $N_{dv} = 0$), giving:

$$M = (F\tau_s)\left[\frac{\exp(2t/\tau_s) - 1}{\exp(2t/\tau_s) + 1}\right] \quad (6.9)$$

where τ_s is given by:

$$\tau_s = (m / M_{dv}DF)^{1/2} \quad (6.10)$$

Using Eq. (6.8), the total lifetime of adatoms before chemisorption is then given by:

$$\tau = \tau_s \frac{\exp(2t/\tau_s) + 1}{\exp(2t/\tau_s) - 1} \qquad (6.11)$$

During the transient (that is, for $t < \tau_S$), the dimer concentration is low and collisions between adatoms are rare resulting in a lifetime, τ, that is greater than τ_S. Hence, the dimer incorporation rate is essentially negligible before the time τ_S. However, if t is greater than τ_S, then each adatom has a lifetime essentially equal to τ_S, and a surface diffusion length given by:

$$\lambda = (D\tau_s)^{1/2} = \left(\frac{mD}{M_{dv}F}\right)^{1/4} \qquad (6.12)$$

The number of collisions to form a dimer is simply the number of adatoms in the diffusion area, $D\tau_S$, since after τ_S each adatom will have collided with another adatom and formed a dimer. The number of collisions before forming a dimer or the number of adatoms within the diffusion area, $D\tau_S$, is $F\tau_S D\tau_S$. The probability per collision of forming a dimer is therefore $M_{dv}/m = (F\tau_S D\tau_S)^{-1}$ which is simply a rearrangement of Eq. (6.10).

Group III dimer nucleation in the initial stage of the bilayer growth cycle is expected to occur predominantly at the group V dimer sites as compared to the dangling orbital sites due to the rate limiting step at the orbital sites as discussed earlier as well as the initially large separation of the dangling orbital sites as compared to the dimerized group V sites. However, the incorporation of group III adatoms at a group V dimer site, as depicted in Fig. 6.3(b), causes lateral relaxation of the underlying group V atoms. These local bond distortions promote adatom incorporation at the dangling orbital sites near the nuclei (that

is, island growth) rather than the formation of new nuclei at the group V dimer sites. Also, the electron counting model reveals that island growth in the [011] direction is unfavorable due to electron deficits associated with the missing dimer row [6.12]. An anisotropy in the incorporation probability is therefore expected such that the nuclei extend preferentially in the [0 -1 1] direction, as depicted in Fig. 6.3(c). This agrees with scanning tunnelling microscopy (STM) images of the 2x4 GaAs surface [6.14, 6.15], with observations of growth on vicinal surfaces [6.16], and with the anisotropy in the dimensions of the LCM structure as shown in Fig. 4.8 and as observed elsewhere [1.22, 1.23]. This suggests that the lateral scale of the composition modulation is determined by 2D island growth as discussed below. However, anisotropy in the incorporation probabilities or the surface diffusion constants are not addressed by the simple model presented here.

2D island growth may start as soon as the adatom diffusion length is greater than the average distance between nuclei. In general, however, nucleation continues until the incorporation rate at the edges of nuclei is roughly equal to the nucleation rate on the flat surface [6.13]. Using Eq. (6.8), the saturation density of nuclei, N_0, is therefore on the order of:

$$N_0 = (n/m)\, M_{dv} \qquad (6.13)$$

Subsequently, adatoms are adsorbed preferentially at the edges of the nuclei and further nucleation occurs rarely. The group III monolayer is then completed by the accretion of adatoms at the 2D island edges which grow to a diameter roughly equal to the nuclei separation, r, given by:

$$r = N_0^{-1/2} = \left(\frac{m}{n}\right)^{1/2} M_{dv}^{-1/2} \qquad (6.14)$$

Meanwhile, group V incorporation will be initiated (not shown in Fig. 6.3) as soon as the underlying group III islands are large enough to provide a suitable bonding configuration for group V dimers to chemisorb.

While the magnitude of the compositional excursions associated with the LCM can

be reduced during conventional epitaxy by inhibiting the surface adatom diffusion lengths, the dimensions of the LCM structure (that is, the period of the modulation) are essentially unchanged [1.22, 1.23]. This observation is understood from Eq. (6.14) which reveals that the 2D island size, and therefore the lateral scale of the composition modulation, depends only on the probability ratio, n^{-1}/m^{-1}, which is a constant for a given surface bonding configuration. The LCM structure in conventional epitaxy is on average about 100 Å in the [011] direction and about 1000 Å in the [0 -1 1] direction as evident in Fig. 4.8 and from previous studies [1.22, 1.23]. This gives an island density, N_o, equal to 10^{11} cm^{-2} and a probability ratio, n^{-1}/m^{-1}, on the order of 10^3. Since N_o is much less than the surface site density, essentially all of the bilayer growth cycle occurs via incorporation at 2D island edges.

Describing epitaxy in the regime of 2D island growth is difficult due to the implicit time dependence of N_{dv} in Eq. (6.8). Although the island density is fixed by Eq. (6.13), the size and hence the periphery of the islands increases with time such that the lifetime of adatoms before incorporation continually decreases. Nevertheless, the effect of the growth conditions on the compositional excursions of the LCM during 2D island growth can be understood by solving Eq. (6.8) with a fixed value of N_{dv} (and with $M_{dv}/m = 0$), giving:

$$\lambda = \left(\frac{nD}{N_{dv}F}\right)^{1/4} \tag{6.15}$$

which is similar to Eq. (6.12). Eqs. (6.12) and (6.15) reveal that decreasing the surface diffusion constant, D, via the growth temperature, or increasing F (that is, the growth rate), both limit the diffusion length of the adatoms before incorporation takes place. The LCM is therefore limited by reducing the number of site visits by an adatom or, equivalently, the diffusion area given roughly as λ^2.

Finally, we consider roughening due to incorporation on top of 2D islands. The

morphology will roughen only if the adatom transport on top of the islands is insufficient to allow atoms to leave the tops of islands as fast as they are arriving. The nuclei density within the diffusion area, $D\tau_s$, after a time, τ_s, is $F\tau_s$. Hence, the separation between nuclei and therefore the island diameter is expected to be $r < (F\tau_s)^{-1/2}$. Using Eqs. (6.10) and (6.12), the ratio of the island diameter to the surface diffusion length is therefore $r/\lambda < (M_{dv}/m)^{1/2}$. Since the probability, M_{dv}/m, is less than unity, the surface diffusion length is always greater than the island diameter. Adatoms incident on top of 2D islands are therefore able to diffuse to the island edges and step down without significant growth on top of the islands until they have coalesced, completing the deposition of one monolayer. In practice, some roughening occurs due to the existence of an energy barrier at the step edge [6.17].

6.2.2. H-assisted Epitaxy

The starting surface under group V stabilized conditions and atomic hydrogen exposure has a 2x1 reconstruction (with respect to the surface dimers) as shown by the surface unit cell (box) in Fig. 6.3(d). This surface has been shown to have a lower energy compared to the conventional 2x4 surface and also satisfies the electron counting model [4.6]. Previous authors [6.18, 6.19] have also suggested that the group V dimer bonds may be cleaved by H, producing a 1x1 surface reconstruction. However, this contradicts the 2x1 surface reconstruction actually observed by RHEED in this work. The fraction of group V dimer bonds cleaved by H is therefore considered to be insignificant under the growth conditions used in this study.

An enhanced nucleation rate has been observed directly by STM in the case of Ge growth on a H-exposed (100) Si surface where the surface reconstruction changes from 2x1 to 1x1 [6.20]. Previous studies [3.14] suggest that a similar enhancement is expected

for H-exposed III-V surfaces where the 2x4 to 2x1 transformation increases the site density available for group III chemisorption due to the absence of the missing dimer row. The site density increases from $M_{dv} = 2$ per 2x4 cell on the conventional surface, labelled (i) and (ii) in Fig. 6.3(a), to $M_{dv}' = 4$ for the same area on the H-exposed surface, labelled (i) to (iv) in Fig. 6.3(d).

We speculate that the nucleation rate on H-exposed III-V surfaces is further enhanced by the possibility of "monomer" formation. In the case of conventional epitaxy, dimer formation must occur as a stepwise process involving two adatoms that have to make a number of attempts via unstable adsorption sites before achieving stable pairing. In H-assisted epitaxy, however, "monomer" configurations may occur which involve the incorporation of only a single adatom with H, as illustrated in Fig. 6.3(e), rather than requiring the "simultaneous" chemisorption of two adatoms in order to form a stable dimer. The H atoms in these configurations may arise from the physisorbed state, from the underlying surface in a surfactant exchange mechanism [6.21], or from III-H_x molecules ($x = 1, 2, 3$) migrating to the binding site [1.33-1.35, 6.6, 6.7]. Single adatoms with H satisfy the electron counting model and are therefore expected to be electronically stable and energetically favorable. Indeed, the vibrational modes of H covalently bonded to both group III and V surface sites have been observed [6.22-6.25]. The monomer nuclei, assisted by the surfactant exchange mechanism [6.21], would presumably form dimers in the later stage of the bilayer growth cycle. Hence, the enhanced nucleation rate due to monomer formation can be described for simplicity by a dimer incorporation probability, $1/m'$, that is greater than that ($1/m$) in conventional epitaxy.

A rough comparison can be made between the experimental data in Fig. 4.9 and the model predictions given by Eqs. (6.13) and (6.15). Combining Eqs. (6.13) and (6.15), the adatom surface diffusion length during 2D island growth in the presence of H, λ', as compared to that in conventional epitaxy, λ, is given by:

$$\frac{\lambda'}{\lambda} = \left(\frac{M'_{dv}}{m'} \frac{m}{M_{dv}} \right)^{-1/4} \tag{6.16}$$

This assumes that the ratio of site vacancies, N_{dv}'/N_{dv}, is roughly equal to that at the saturation point, N_0'/N_0, throughout the bilayer growth cycle. Assuming the dangling orbital sites are the preferred adsorption sites for H, and that M_{dv}'/m' is directly proportional to the H surface coverage, θ, gives:

$$(M_{dv}'/m')/(M_{dv}/m) = 1 + 2\theta\,(2m/m' - 1) \tag{6.17}$$

Fig. 6.4 shows the surface diffusion length ratio, λ'/λ, as a function of the H surface coverage, θ, evaluated by combining Eqs. (6.16) and (6.17) with m/m′ = 1, 1.5 and 3.

The model parameter, m/m′, can be estimated by assuming that the degree of LCM, as measured by the linewidth and red-shift data in Fig. 4.9, is proportional to the diffusion area, λ^2, as discussed earlier. Fig. 6.4 shows the surface diffusion length ratios, λ'/λ, evaluated from the linewidth (FWHM) and red-shift (ΔE) data in Fig. 4.9. These ratios are in good agreement with the growth rate (GR) ratios measured at the bottom of etched grooves as in Fig. 4.10, assuming λ'/λ = GR′/GR. These growth rates, however, depend on the groove separation (for separations less than or on the order of λ), involve diffusion on non-(100) surfaces, and also do not account for anisotropic diffusion. These considerations, and the additional uncertainties in the H surface coverage described earlier, imply that the data in Fig. 6.4 are only rough estimates. Nevertheless, reasonable agreement between the model and the experimental data is obtained by using a value for m/m′ of about 1.5.

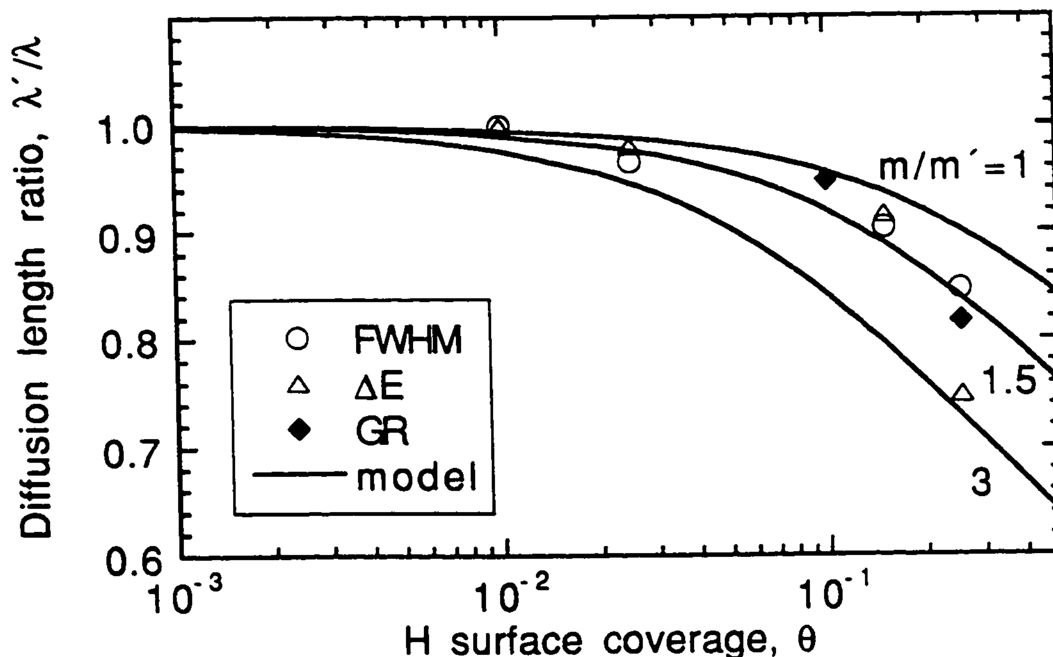

Fig. 6.4. Surface diffusion length ratio, λ'/λ, versus the H surface coverage, θ, using a model parameter of $m/m' = 1$, 1.5 and 3. Experimental data points are derived from the linewidth (FWHM) and red-shift (ΔE) measurements in Fig. 4.9, and the growth rate (GR) measurements at the bottom of etched grooves as in Fig. 4.10.

As considered earlier, the electron counting model reveals that island growth in the [011] direction is unfavorable during conventional epitaxy due to electron deficits associated with the missing dimer row. In the case of the H-exposed surface, however, the excess electrons required to fill the missing dimer row are provided by H atoms situated on the dangling orbital sites. The rate limiting step described earlier is therefore eliminated on the 2x1 H-exposed surface. As a result, adatom incorporation at 2D island edges is promoted, particularly in the [011] direction, producing smaller compositional excursions (weaker black-white contrast in Fig. 4.8) and a 2D island size that is more isotropic. This is consistent with the observation of enhanced step flow growth on H-exposed vicinal

surfaces misoriented in the [011] direction [1.32-1.35]. For the purposes of this work, we simply assume that the probability of incorporation at 2D islands in the presence of H, $1/n'$, is enhanced as compared to that ($1/n$) in conventional epitaxy (that is, $n/n' > 1$). Combining Eqs. (6.13) and (6.17), the 2D island size in the presence of H, N_o', as compared to that in conventional epitaxy, N_o, is given by:

$$\frac{N_o'}{N_o} = \frac{n'}{n}\left[1 + 2\theta\,(2m/m' - 1)\right] \tag{6.18}$$

Using N_o'/N_o greater than unity as evident in Fig. 4.8, $\theta = 0.15$ as used in Fig. 4.8, and $m/m' = 1.5$ as determined earlier gives $n/n' < 1.6$. These arguments, however, are highly qualitative and do not properly account for the anisotropy in the incorporation probabilities or the surface diffusion constants. Considering the complexity of these growth processes, Monte Carlo simulation techniques are likely required for a more realistic description of epitaxial growth in the presence of H [6.26-6.28]. Direct observation of the nuclei and 2D islands by a vacuum-linked scanning tunnelling microscope (STM) is also recommended for future studies.

6.3. Chapter Conclusions

In summary, the group V incorporation has been modelled for InGaAsP layers grown on (100) InP substrates by GSMBE. Thermodynamic models demonstrate the preferential sticking of As to In sites and of P to Ga sites within the miscibility gap which is consistent with the formation of InAs-rich and GaP-rich regions associated with the LCM structure.

A simple rate equation model has shown that the reduction in adatom diffusion length with H exposure can be explained by an enhanced incorporation rate. The enhanced incorporation rate is attributed to an increased surface site density, to the possibility of

stable monomer formation in the presence of H, and to the absence of the rate limiting steps associated with the missing dimer row in the conventional 2x4 surface reconstruction.

CHAPTER 7

Conclusions and Suggestions for Future Work

TEM, PL, and DCXRD have been used to characterize GSMBE-grown InGaAsP layers and quantum wells (QWs). Greater LCM was observed in tensile strained material with compositions that lie deeper within the miscibility gap as compared with lattice-matched or compressively strained material. Comparison of results from thick layers and QWs suggested that the LCM becomes more severe with increasing layer thickness. Differences between the observed LCM structure and that predicted by bulk models, and the influence of growth conditions, substrate surface orientation and lattice mismatch strain on the compositional fluctuations, suggested the need for a surface model to explain the development of the LCM.

Ar plasma-assisted epitaxy was shown to reduce the LCM in thick InGaAsP layers and single QWs grown on (100) InP substrates, resulting in improved structural and optical properties as compared to conventional epitaxy without plasma. Comparison of these results with those obtained by an independent atomic hydrogen source indicated that the reduced LCM was caused by atomic hydrogen present in the Ar plasma stream. Improvements in DH laser performance by H-assisted epitaxy, attributed to a reduction of LCM, was also established. Because the LCM adversely effects the structural and optical properties of InGaAsP/InP quantum wells for compositions that lie within the miscibility gap, H-assisted epitaxy is also expected to be beneficial for quantum well laser diodes. Similarly, the LCM becomes more severe for tensile strained InGaAsP layers such as that used for strain compensated laser structures [1.24]. Reduction of the LCM in this case would also be beneficial to device performance.

Hall effect and photoluminescence studies on InP homoepitaxial layers suggested

that the P flux of early growths (after installation of a new catalyst) contained a significant fraction of unwanted cracker products, such as P_4, resulting in a higher concentration of point defects, as compared to later growths where the catalyst was acting efficiently and the P flux was predominantly P_2. H-assisted epitaxy therefore appeared to have the most benefit when the MBE system was not operating at optimum performance. The defect reduction was attributed to reactions between H and the unwanted species (probably P_4) on the growing surface, and by the absence of the missing dimer row present during conventional epitaxy. The donor impurity concentration increased with thermal source temperature probably due to degassing. Ar plasma-assisted epitaxy, on the other hand, was shown to provide an adequate flux of H (to reduce LCM, for example) while eliminating the degassing problems associated with the thermal cracker.

A simple rate equation model showed that the reduced LCM in the presence of H could be explained by a reduction in the surface adatom diffusion lengths due to an enhanced incorporation rate. The enhanced incorporation rate was attributed to an increased surface site density, to the possibility of stable monomer formation in the presence of H, and to the absence of the rate limiting steps associated with the missing dimer row in the conventional 2x4 surface reconstruction. Despite the successes of this model, the arguments were highly qualitative and did not properly account for the anisotropy in the incorporation probabilities or the surface diffusion constants. Considering the complexity of these growth processes, Monte Carlo simulation techniques are likely required for a more realistic description of epitaxial growth in the presence of H. Direct observation of the nuclei and 2D islands by a vacuum-linked scanning tunnelling microscope (STM) is also recommended for future studies.

References

1.1. G. B. Stringfellow, J. Cryst. Growth **65** (1983) 454.

1.2. G. B. Stringfellow, J. Cryst. Growth **58** (1982) 194.

1.3. K. Onabe, Jpn. J. Appl. Phys. **21** (1982) L323.

1.4. K. Onabe, Jpn. J. Appl. Phys. **21** (1982) 797.

1.5. M. B. Panish and H. Temkin, *Gas Source Molecular Beam Epitaxy*, Springer Series in Materials Science **26** (Springer-Verlag, Berlin, 1993).

1.6. P. Henoc, A. Izrael, M. Quillec and H. Launois, Appl. Phys. Lett. **40** (1982) 963.

1.7. A. T. Macrander and S. Lau, J. Electrochem. Soc. **138** (1991) 1147.

1.8. D. A. Porter and K. E. Easterling, *Phase Transformations in Metals and Alloys* (Chapman and Hall, London, 1992) p. 18.

1.9. G. B. Stringfellow, J. Phys. Chem. Solids **34** (1973) 1749.

1.10. J. Y. Tsao, *Materials Fundamentals of Molecular Beam Epitaxy* (Academic Press, Inc., Boston, 1993) p. 93.

1.11. M. Ichimura and A. Sasaki, J. Cryst. Growth **98** (1989) 18.

1.12. S. Mahajan, Mat. Sci. Eng. B **30** (1995) 187.

1.13. K. Lee, B. A. Philips, R. S. McFadden and S. Mahajan, Mat. Sci. Eng. B **32** (1995) 231.

1.14. K. Tappura and J. Laurila, J. Cryst. Growth **131** (1993) 309.

1.15. T. L. McDevitt, S. Mahajan and D. E. Laughlin, Phys. Rev. B **45** (1992) 6614.

1.16. S. N. G. Chu, S. Nakahara, K. E. Strege and W. D. Johnson, Jr., J. Appl. Phys. **57** (1985) 4610.

1.17. A. G. Norman and G. R. Booker, J. Appl. Phys. **57** (1985) 4715.

1.18. S. Mahajan, B. V. Dutt, H. Temkin, R. J. Cava and W. A. Bonner, J. Cryst. Growth **68** (1984) 589.

1.19. S. Mukai, J. Appl. Phys. **54** (1983) 2635.

1.20. J. S. Roberts, G. B. Scott and J. P. Gowers, J. Appl. Phys. **52** (1981) 4018.

1.21. K. Takahei and H. Nagai, Jpn. J. Appl. Phys. **20** (1981) L313.

1.22. R. R. LaPierre, T. Okada, B. J. Robinson, D. A. Thompson, and G. C. Weatherly, J. Cryst. Growth **155** (1995) 1.

1.23. R. R. LaPierre, M. Eng. thesis (McMaster University, Hamilton, Ontario, Canada, 1992).

1.24. A. Ponchet, A. Rocher, J. Y. Emery, C. Starck and L. Goldstein, Fifth International Conference on Indium Phosphide and Related Materials (Paris, 1994) p. 183.

1.25. EPI MBE Products Group, 1290 Hammond Road, Saint Paul, MN 55110, U.S.A., Application Note, August/September, 1994 and January, 1996.

1.26. H. Shimomura, Y. Okada and M. Kawabe, Jpn. J. Appl. Phys. **31** (1992) L628.

1.27. H. Simomura, Y. Okada, H. Matsumoto, M. Kawabe, Y. Kitami and Y. Bando, Jpn. J. Appl. Phys. **32** (1993) 632.

1.28. Y. Okada, H. Shimomura and M. Kawabe, J. Appl. Phys. **73** (1993) 7376.

1.29. Y. J. Chun, Y. Okada and M. Kawabe, Jpn. J. Appl. Phys. **32** (1993) L1085.

1.30. A. Sakai and T. Tatsumi, Appl. Phys. Lett. **64** (1994) 52.

1.31. Y. J. Chun, Y. Okada and M. Kawabe, J. Cryst. Growth **150** (1995) 497.

1.32. H. Asahi, T. Hisaka, S. G. Kim, T. Kaneko, S. J. Yu, Y. Okuno and S. Gonda, Appl. Phys. Lett. **61** (1992) 1054.

1.33. Y. Okada, T. Sugaya, S. Ohta, T. Fujita and M. Kawabe, Jpn. J. Appl. Phys. **34** (1995) 238.

1.34. Y. Okada, T. Fujita and M. Kawabe, Jpn. J. Appl. Phys. **34** (1995) L768.

1.35. Y. Okada, T. Fujita and M. Kawabe, Appl. Phys. Lett. **67** (1995) 676.

2.1. A. S. Jordan and A. Robertson, J. Vac. Sci. Technol. A **12** (1994) 204.

2.2. P. G. Hofstra, B. J. Robinson, D. A. Thompson and S. A. McMaster, J. Vac. Sci. Technol. A **13** (1995) 2146.

2.3. D. A. Thompson, D. B. Mitchell, B. J. Robinson, R. R. LaPierre and P. Mascher, *Ion Beam Modification of Materials* (Elsevier Science, Amsterdam, 1996) p. 769.

2.4. M. A. Herman, D. Bimberg and J. Christen, J. Appl. Phys. **70** (1991) R1.

2.5. R. Benzaquen, S. Charbonneau, N. Sawadsky, A. P. Roth, L. Hobbs and G. Knight, J. Appl. Phys. **75** (1994) 2633.

2.6. Y. P. Varshni, Physica A **34** (1967) 149.

2.7. *Landolt-Börnstein Numerical Data and Functional Relationships in Science and Technology*, Vol. 17, *Semiconductors:Physics of Group IV Elements and III-V Compounds*, ed. by O. Madelung (Springer-Verlag, Berlin, 1982).

2.8. H. Kyuragi, A. Suzuki, S. Matsumura and H. Matsunami, Appl. Phys. Lett. **37** (1980) 723.

2.9. S. Adachi, J. Appl. Phys. **53** (1982) 8775.

2.10. *Rocking Curve Analysis by Dynamical Simulation*, version 1.00 (Bede Scientific Instruments, 1990).

3.1. D. D. Perovic, G. C. Weatherly and D. C. Houghton, Phil. Mag. A **64** (1991) 1.

3.2. M. M. J. Treacy, J. M. Gibson and A. Howie, Phil. Mag. A **51** (1985) 389.

3.3. E. P. O'Reilly and A. R. Adams, IEEE J. Quantum Electron. **30** (1994) 366.

3.4. E. F. Schubert and W. T. Tsang, Phys. Rev. B **34** (1986) 2991.

3.5. D. Cherns, P. D. Greene, A. Hainsworth and A. R. Preston, Phase Separation in InGaAsP Epitaxial Layers in *Microscopy of Semiconductor Materials*, eds. A. G. Cullis and P. D. Augustus, Inst. Phys. Conf. Ser. No. 87 (The Institute of Physics, London-Bristol, 1987) p. 83

3.6. T. Okada, R. LaPierre, C. Mullan, G. C. Weatherly, B. J. Robinson and D. A. Thompson, Ninth International Conference on Microscopy of Semiconducting Materials (Oxford, England, 1995).

3.7. T. Okada, G. C. Weatherly and D. W. McComb, J. Appl. Phys. **81** (1997) 2185.

3.8. J. W. Cahn, Acta. Metall. **10** (1962) 179; Trans. Metall. Soc. AIME **242** (1968) 166.

3.9. I. P. Ipatova, V. G. Malyshkin and V. A. Shchukin, J. Appl. Phys. **74** (1993) 7198.

3.10. F. Glas, J. Appl. Phys. **62** (1987) 3201.

3.11. G. B. Stringfellow, J. Electronic Mat. **11** (1982) 903.

3.12. M. Quillec, C. Daguet, J. L. Benchimol and H. Launois, Appl. Phys. Lett. **40** (1982) 325.

3.13. M. Hata, T. Isu, A. Watanabe, and Y. Katayama, J. Vac. Sci. Technol. B **8** (1990) 692.

3.14. R. R. LaPierre, B. J. Robinson and D. A. Thompson, Appl. Surf. Sci. **90** (1995) 437.

3.15. J. W. Lee, T. I. Kim and T. Tsakalakos, J. Electrochem. Soc. **142** (1995) 267.

3.16. A. Ponchet, A. le Corre, A. Godefroy, S. Salaün and A. Poudoulec, J. Cryst. Growth **153** (1995) 71.

3.17. U. Bangert, A. J. Harvey, V. A. Wilkinson, C. Dieker, J. M. Jowett, A. D. Smith, S. D. Perrin and C. J. Gibbins, J. Cryst. Growth **132** (1993) 231.

4.1. D. Mitchell, Ph. D. dissertation (McMaster University, Hamilton, Ontario, Canada, 1995).

4.2. G. N. Maracas, K. Shiralagi, R. Ramamurti and R. W. Carpenter, J. Electron. Mater. **22** (1993) 1375

4.3. P. Dreszer, W. M. Chen, D. Wasik, R. Leon, W. Walukiewicz, B. W. Liang, C. W. Tu and E. R. Weber, J. Electron. Mater. **22** (1993) 1487.

4.4. P. Dreszer, W. M. Chen, K. Seendripu, J. A. Wolk, W. Walukiewicz, B. W. Liang, C. W. Tu and E. R. Weber, Phys. Rev. B **47** (1993) 4111.

4.5. S. B. Ogale, A. Madhukar and M. Thomsen, Appl. Phys. Lett. **51**, 837 (1987).

4.6. Y. Miyamoto and S. Nonoyama, Phys. Rev. B **46** (1992) 6915.

4.7. G. P. Agrawal and N. K. Dutta, *Long-Wavelength Semiconductor Lasers* (Van Norstrand Reinhold Company, New York, 1986).

4.8. R. G. Hunsperger, *Integrated Optics* (Springer-Verlag, Berlin, 1995) p. 74.

5.1. W. Walukiewicz, J. Lagowski, L. Jastrzebski, P. Rava, M. Lichtensteiger, C. H. Gatos and H. C. Gatos, J. Appl. Phys. **51** (1980) 2659.

5.2. H. Kunzel, J. Knecht, H. Jung, K. Wunstel and K. Ploog, Appl. Phys. A **28**, (1982) 167.

5.3. J. C. Garcia, A. C. Beye, J. P. Contour, G. Neu and J. Massies, Appl. Phys. Lett. **52** (1988) 1596.

5.4. J. I. Pankove and N. M. Johnson, *Hydrogen in Semiconductors*, Semiconductors and Semimetals **34** (Academic Press Inc., Boston, 1991).

5.5. S. J. Pearton, J. W. Corbett and M. Stavola, *Hydrogen in Crytalline Semiconductors*, Springer Series in Materials Science **16** (Springer-Verlag, Berlin, 1992).

5.6. S. J. Pearton, *Hydrogen in Compound Semiconductors*, Materials Science Forum

148-149 (Trans Tech Publications, Switzerland, 1994).

5.7. S. Balasubramanian, N. Balasubramanian and V. Kumar, Semi. Sci. Technol. **10** (1995) 310.

5.8. M. A. Di Forte-Poisson, C. Brylinski and J. P. Duchemin, Appl. Phys. Lett. **46** (1985) 476.

5.9. *Properties of Indium Phosphide*, EMIS Datareviews Series No. 6 (INSPEC, London and New York, 1991) p. 170.

5.10. B. Wakefield, L. Eaves, K. A. Prior, A. W. Nelson and G. J. Davies, J. Phys. D **17** (1984) L133.

5.11. A. A. Iliads and S. Ovadia, J. Appl. Phys. **63** (1988) 5460.

5.12. T. S. Cheng, V. M. Airaksinen and C. R. Stanley, J. Appl. Phys. **64** (1988) 6662.

6.1. M. B. Panish and S. Sumski, J. Appl. Phys. **55** (1984) 3571.

6.2. R. R. LaPierre, B. J. Robinson and D. A. Thompson, J. Appl. Phys. **79** (1996) 3021.

6.3. H. Seki and A. Koukitu, J. Cryst. Growth **78** (1986) 342.

6.4. S. Pelligrino and L. Vitali, J. Electron. Mat. **25** (1996) 519.

6.5. J. N. Baillargeon, A. Y. Cho and K. Y. Cheng, J. Appl. Phys. **79** (1996) 7652.

6.6. Y. Morishiti, Y. Nomura, S. Goto and Y. Katayama, Appl. Phys. Lett. **67** (1995) 2500.

6.7. T. Sugaya, Y. Okada and M. Kawabe, Appl. Surf. Sci. **60/61** (1992) 251.

6.8. C. W. Snyder and B. G. Orr, Phys. Rev. Lett. **70** (1993) 1030.

6.9. H. H. Farrell, J. P. Harbison and L. D. Peterson, J. Vac. Sci. Technol. B **5** (1987) 1482.

6.10. J. P. Harbison and H. H. Farrell, J. Vac. Sci. Technol. B **6** (1988) 733.

6.11. H. H. Farrell, R. E. Nahory and J. P. Harbison, J. Vac. Sci. Technol. B **6** (1988) 779.

6.12. M. D. Pashley, Phys. Rev. B **40** (1989) 10481.

6.13. M. Hata, T. Isu, A. Watanabe, Y. Kajikawa and Y. Katayama, J. Cryst. Growth **114** (1991) 203.

6.14. M. D. Pashley, K. W. Haberern, W. Friday, J. M. Woodall and P. D. Kirchner,

Phys. Rev. Lett. **60** (1988) 2176.

6.15. M. D. Pashley, K. W. Haberern and J. M. Woodall, J. Vac. Sci. Technol. B **6** (1988) 1468.

6.16. P. R. Pukite, G. S. Petrich, S. Batra and P. I. Cohen, J. Cryst. Growth **95** (1989) 269.

6.17. R. L. Schwoebel and E. J. Shipsey, J. Appl. Phys. **37** (1966) 3682.

6.18. Y. Horikoshi, H. Yamaguchi, F. Briones and M. Kawashima, J. Cryst. Growth **105** (1990) 326.

6.19. M. Tsuda, M. Morishita, S. Oikawa and M. Mashita, Jpn. J. Appl. Phys. **27** (1988) L960.

6.20. M. Okada, T. Shimizu, H. Ikeda, S. Zaima and Y. Yasuda, Appl. Surf. Sci. **113/114** (1997) 349.

6.21. Z. Zhang and M. G. Lagally, Phys. Rev. Lett. **72** (1994) 693.

6.22. H. Lüth and R. Matz, Phys. Rev. Lett. **46** (1981) 1652.

6.23. J. A. Schaefer, Th. Allinger, Ch. Stuhlmann, U. Beckers and H. Ibach, Surf. Sci. **251/252** (1990) 1000.

6.24. T. Allinger, J. A. Schaefer, Ch. Stuhlmann, U. Beckers and H. Ibach, Physica B **170** (1991) 481.

6.25. U. del Pennino, C. Mariani, A. Amoddeo, F. Profix and C. A. Sébenne, Physica B **170** (1991) 487.

6.26. A. Madhukar, Surf. Sci. **132** (1983) 344.

6.27. C. D. Adams and D. J. Srolovitz, J. Appl. Phys. **74** (1993) 1707.

6.28. F. Léonard, M. Laradji and R. C. Desai, Phys. Rev. B **55** (1997) 1887.